UNIVERSITY OF CAPE TOWN
IYUNIVESITHI YASEKAPA • UNIVERSITEIT VAN KAAPSTAD

Fluid-structure interaction modelling of a patient-specific arteriovenous access fistula

by

Winston Guess

Thesis Presented for the Degree of
Master of Science in Engineering in Mechanical Engineering
University of Cape Town

November 24, 2016

cerecam
Centre for Research in Computational and Applied Mechanics

Declaration of authorship

I know the meaning of plagiarism and declare that all the work in the document, save for that which is properly acknowledged, is my own. This dissertation has been submitted to the Turnitin module and I confirm that my supervisor has seen my report and any concerns revealed by such have been resolved with my supervisor.

Winston Guess

Signed by candidate

Signature

22/11/16

Date

Acknowledgements

First and foremost, I wish to express my most sincere gratitude to my primary supervisor, Prof. B. Daya Reddy for his continuous support, patience, and encouragement from the first day of this project to the last. I am also highly indebted to my co-supervisor Andrew McBride. His motivation, guidance, and understanding throughout kept me focused and going in the right directions.

I would also like to thank my collaborators. This project would not have been possible without Prof. Delawir Kahn, Assoc. Prof. Thomas Franz, and Dr Jennifer Downs. Huge thanks must go to Stephen Jermy who worked tirelessly processing complex and problematic data for our research. I am also grateful for his extra effort in answering all of my questions along the way. A special thank you goes to Andie De Villiers; her input, and questions, and answers brought so much to this work. To the whole team, thank you for all the hilarious attempts trying to explain to each other the details of our respective work and specialisations.

To my colleagues in CERECAM, thank you for the wonderful lunchtime conversations and the interesting team building exercises. A special thanks to my good friend Ritesh Rama who helped me through some dark days with Bash and Latex. To Mebratu Wakeni, thank you for being such a great fellow Gunner. My thanks also go to Natalie Bent, Mama Nontsikelelo, and Sisi Nozuko, for all they have done for me.

My right Achilles tendon must also be acknowledged for its role in this work, without your fateful rupture, I might not have made some crucial breakthroughs quite as quickly.

I would also like to thank the ANSYS support affiliates who quickly and thoroughly answered my elaborate questions; particularly Danie de Kock, Daniel Correia, and the rest of the Qfinsoft support team.

Prof. Peter Smith also provided me with important advice and perspective at a crucial stage of my work, I greatly appreciate his support and wisdom.

Lastly, the biggest thanks go to my amazing family and my friends. Their enormous encouragement, support, love, and advice all along the way is the main reason that I have got this far.

This study was supported financially by the National Research Foundation (NRF) of South Africa and by the South African Research Chair in Computational Mechanics. Any opinion, findings and conclusions or recommendations expressed in this publication are those of the authors and therefore the NRF does not accept any liability in regard thereto.

Fluid-structure interaction modelling of a patient-specific arteriovenous access fistula

Winston Guess
University of Cape Town

Abstract

This research forms part of an interdisciplinary project that aims to improve the detailed understanding of the haemodynamics and vascular mechanics in arteriovenous shunts that are required for haemodialysis treatments. A combination of new PC-MRA imaging and computational modelling of in vivo blood flow aims to determine the haemodynamic conditions that may lead to the high failure rate of vascular access in these circumstances. This thesis focuses on developing a patient-specific fluid-structure interaction (FSI) model of a PC-MRA imaged arteriovenous fistula.

The numerical FSI model is developed and simulated within the commercial multiphysics simulation package ANSYS® Academic Research, Release 16. The blood flow is modelled as a Newtonian fluid with the finite-volume method solver ANSYS® Fluent®. A pulsatile mass-flow boundary condition is applied at the artery inlet and a three-element Windkessel model at the artery and vein outlets. ANSYS® Mechanical™, a finite element method solver, is used to model the nonlinear behaviour of the vessel walls. The artery and vein walls are assumed to follow a third-order Yeoh model, and are differentiated by thickness and by material strength characteristics. The staggered FSI model is configured and executed in ANSYS® Workbench™, forming a semi-implicit coupling of the blood flow and vessel wall models.

This work shows the effectiveness of combining a number of stabilisation techniques to simultaneously overcome the added-mass effect and optimise the efficiency of the overall model. The PC-MRA data, fluid model, and FSI model show almost identical flow features in the fistula; this applies in particular to a flow recirculation region in the vein that could potentially lead to fistula failure.

Contents

Declaration of authorship **i**

Acknowledgements **iii**

Abstract **v**

Table of contents **vii**

List of figures **xiii**

List of tables **xvii**

1 Introduction **1**

1.1 Problem description 1

1.2 Aim and objectives 7

1.3 Outline 8

2 Patient-specific data acquisition **11**

2.1 Magnetic resonance imaging 11

2.1.1 Excitation 12

2.1.2 Signal localisation 14

2.1.3 Gradient-recalled Echo 16

2.1.4 Image contrast 17

2.2 Phase-contrast magnetic resonance angiography 18

3 Nonlinear continuum mechanics **23**

3.1 Notation 23

3.2 Kinematics 24

3.3 Stress measures 28

3.4 Conservation laws 29

3.4.1 Conservation of mass 29

3.4.2 Conservation of momentum 30

3.5 Constitutive relations 30

3.5.1 Hyperelasticity 31

3.5.2 Newtonian fluids 32

3.6 Boundary conditions 33

3.6.1 Solid model 33

3.6.2 Fluid model 34

3.7 Governing equations 34

3.7.1 Solid model 34

3.7.2 Fluid model 35

4 Numerical methods **37**

4.1 The finite element method 37

4.1.1 The weak form 38

4.1.2 Linearisation 38

4.1.3 Discretisation 39

Voigt notation 40

Parent element shape functions and mapping 41

Enhanced assumed strain method 42

Gaussian quadrature 43

The finite element matrices 44

Time discretisation 45

4.1.4 The Newton-Raphson solution procedure 46

The direct sparse matrix solver 47

4.2 The finite volume method 48

4.2.1 Divergence form of the momentum equation 48

4.2.2 Control volume integration 49

The split momentum equations 49

The continuity equation 50

4.2.3 Discretisation schemes 50

Second-order upwind spatial discretisation 51

Least squares gradient reconstruction 52

Pressure discretisation and the co-located scheme 53

Second-order implicit time discretisation and integration 54

4.2.4 Discretisation of the transport equations 54

4.2.5 Pressure-velocity coupling and solving algorithms 54

The SIMPLE algorithm 55

PISO algorithm modification 56

Boundary condition implementation and algorithms 57

Point-iterative solution method 57

Residuals and convergence 59

4.3 Partitioned fluid-structure interaction modelling 59

4.3.1 The semi-implicit staggered algorithm 60

4.3.2 Finite volume mesh adaption 62

4.3.3 The added-mass effect 63

5 Implementation, results, and analysis 65

5.1 PC-MRA acquisition and post-processing 66

5.2 Patient-specific fluid model 69

5.2.1 Geometry reconstruction of the fluid domain 69

5.2.2 Material behaviour and boundary conditions 73

The lumped parameter model 75

5.2.3 Domain discretisation 79

5.2.4 Solver settings and solution behaviour 81

5.2.5 Mesh convergence analysis 85

5.3 Patient-specific solid model 90

5.3.1 Geometry and mesh 90

5.3.2 Material model 91

5.3.3 Boundary and initial conditions 92

5.3.4 Element formulations 94

5.3.5 Solution method 95

5.3.6 Mesh and convergence analysis 96

Initial mesh convergence analysis 96

Secondary mesh convergence analysis 101

5.4 The patient-specific FSI model 106

5.4.1 Boundary and initial conditions 106

5.4.2 Numerical set-up and behaviour 106

5.4.3 FSI and fluid model results and analysis 111

6 Conclusions and recommendations 123

Bibliography 127

List of Figures

1.1 Arteriovenous fistula and graft 3

1.2 Progression of neointimal hyperplasia 4

1.3 Angioplasty and stent placement 5

1.4 Comparison between CFD and PC-MRA WSS vector distribution . . . 7

2.1 Effects of the magnetic field and excitation 13

2.2 The effects of an RF pulse and slice selection gradient 14

2.3 Proton resonance during slice selection 15

2.4 Phase encoding gradient along along the Y-axis 16

2.5 Frequency encoding gradient along along the X-axis 17

2.6 The basic MRI sequence 18

2.7 An example of a fast GRE pulse sequence with velocity encoding 20

3.1 A body in motion - the reference and spatial configurations 26

4.1 Reference, spacial and parent element configurations 41

4.2 A fluid body moving through a fixed control volume. 49

4.3 Spatial and pressure discretisation between neighbouring cells 51

4.4 Discretisation variables used in calculating gradients 52

4.5 The SIMPLE and PISO algorithms 58

4.6 The semi-implicit staggered FSI coupling algorithm 61

5.1 Flow rate waveform profiles approximated from 2D PC-MRA inlet scan 68

5.2 Velocity data from the 2D PC-MRA inlet scan 69

5.3 Velocity streamlines processed from the 3D PC-MRA scan 70

5.4 Fluid domain generation in Meshlab and SolidWorks 72

5.5 The Patient-specific fluid model domain 73

5.6 Artery inlet mass flow boundary condition 75

5.7 Patient-specific blood flow model boundary conditions 76

5.8 The basis of the blocking method 80

5.9 Blocking strategy for fluid mesh at anastomosis 82

5.10 Pressure waveform solutions to fluid models 84

5.11 Average velocity waveform solutions to fluid models 85

5.12 Plots of the fluid solution mesh convergence 87

5.13 Mesh solution comparison of WSS distribution 88

5.14 Mesh solution comparison of pressure distribution 89

5.15 Solid geometry and mesh generation 90

5.16 Artery and vein stress strain curve 92

5.17 Solid model boundary conditions 93

5.18 Initial convergence plot of the error in the L2-norm 97

5.19 Displacement convergence and relative calculation time plots 99

5.20 Displacement norm contours from the initial mesh convergence study . 100

5.21 Solid model mesh convergence behaviour of various element types . . . 101

5.22 Mesh and element maximum principal strain contour comparison . . . 102

5.23 Final convergence plot of the error in the L2-norm with mesh refinement 104

5.24 Mesh and element formulation comparison - displacement norm contours 105

5.25 Unstable and overdamped FSI boundary solution behaviour 112

5.26 Optimally damped FSI boundary solution behaviour 113

5.27 Maximum deformation and principal strain profiles of artery 115

5.28 Maximum deformation and principal strain profiles in the vessel walls . 115

5.29 Fluid and FSI model velocity streamlines 116

5.30 Maximum deformation and principal strain profiles of artery 117

5.31 Fluid and FSI WSS solution contours 118

5.32 PC-MRA and FSI model velocity streamlines 119

5.33 PC-MRA and fluid model velocity streamlines 120

List of Tables

5.1 Details of the 2D PC-MRA scans for volunteers and patients 67

5.2 Details of the 3D PC-MRA scans for volunteers and patients 67

5.3 Windkessel boundary condition implementation - UDF details 78

5.4 Lumped parameter boundary condition details 79

5.5 Critical fluid model solver settings for optimal convergence 83

5.6 Details of the four meshes created for the fluid convergence study . . . 86

5.7 Solution errors to the fluid convergence study 86

5.8 Details and results of the large mesh convergence study 98

5.9 Details and results of the initial mesh convergence study 103

5.10 Computational time per cardiac-cycle for the FSI model 108

5.11 FSI settings for optimal efficiency with a time-step size of 0.005s 111

Chapter 1

Introduction

1.1 Problem description

Haemodialysis is the primary form of renal replacement therapy (RRT) that saves and extends the lives millions of patients worldwide [1–3]. The morbidity, mortality rate and quality of life of these patients are however severely affected in a large part by the consequent complications and interventions associated with vascular access, a surgically created access point to the bloodstream [4–6]. These complications and interventions are a large contributor to the high cost of caring for dialysis patients and make it more difficult to implement dialysis in developing countries where it is most needed [7, 8]. If the frequency of complications to vascular access could be reduced, it is likely that more patients could afford and gain access to haemodialysis.

Renal replacement therapy is required when a patient has end stage renal disease (ESRD), the prognosis of permanent renal failure. A global market survey by Fresenius Medical Care estimated that by the end of 2013 there were more than 3 million ESRD patients worldwide [3]. With the growth rate of the renal replacement population far exceeding the world population growth rate, this number is expected to rise to 5 million by the year 2030 [2, 3]. Estimates show however that the number of patients currently needing RRT worldwide is already between 4.9 and 9.7 million [2]. This is in large part because more than a hundred countries are completely unable to afford RRT, resulting in the death of over a 1 million people every year. There is thus a great need to increase access to dialysis and reduce the RRT gap in developing countries [8–10].

Although the situation is less dire in developed countries, ESRD remains a major cost for health-care systems and the substantial growth in the prevalent dialysis population is expected to continue.

The treatment of choice for renal failure is the kidney transplant, giving patients a much better quality of life than those on dialysis. Few patients are however able to receive a donor kidney, and for the few who do have access to transplantation, waiting lists are long. Peritoneal dialysis uses the lining of the abdominal cavity and a dialysis solution to remove waste and extra fluid from the body. Haemodialysis meanwhile is used by more than 70% of the ESRD population, a proportion that is expected to increase as the use of peritoneal dialysis continues to decrease in developed countries [3, 11, 12]. In haemodialysis treatment, waste products and unwanted extra fluid are removed from the bloodstream. Blood is pumped along an extracorporeal circuit and through a dialyzer, a filter that acts as an artificial kidney, before being returned to the bloodstream. Patients are typically required to be connected to the dialysis machine for four hours, three times a week.

To ensure the efficiency of haemodialysis blood flow rates are required to be high and at the very least 100ml/min more than the dialysis flow rate [13]. Countries vary in regard to the dialysis flow rate regulation, in the United States and Europe this is 400 to 500 ml/min while in Japan this is much lower, at 200 to 250 ml/min [14]. To generate these flow rates and provide an access point where the blood can be extracted and reintegrated into the bloodstream, placement of vascular access is a requirement.

The three most common forms of vascular access are the arteriovenous (AV) fistula, the AV graft, and the central venous catheter, or simply the fistula, graft and catheter respectively. Fistulas and grafts are surgically placed arteriovenous shunts (see Figure 1.1) that require a waiting period after surgery before they are ready for cannulation. Catheters allow for immediate access and can be placed in temporary or permanent forms into any one of the larger veins across the body.

The abnormally high and pulsatile flow rates generated in the vein by AV access are the major reason for the high rate of complications and failure. The flow rates caused by shunting can be upwards of 1000 ml/min which affect patency very negatively [17, 18]. Compared with AV access, catheters are associated with a higher rate of complications and greater levels of risk and mortality rates [19]. The complications associated with

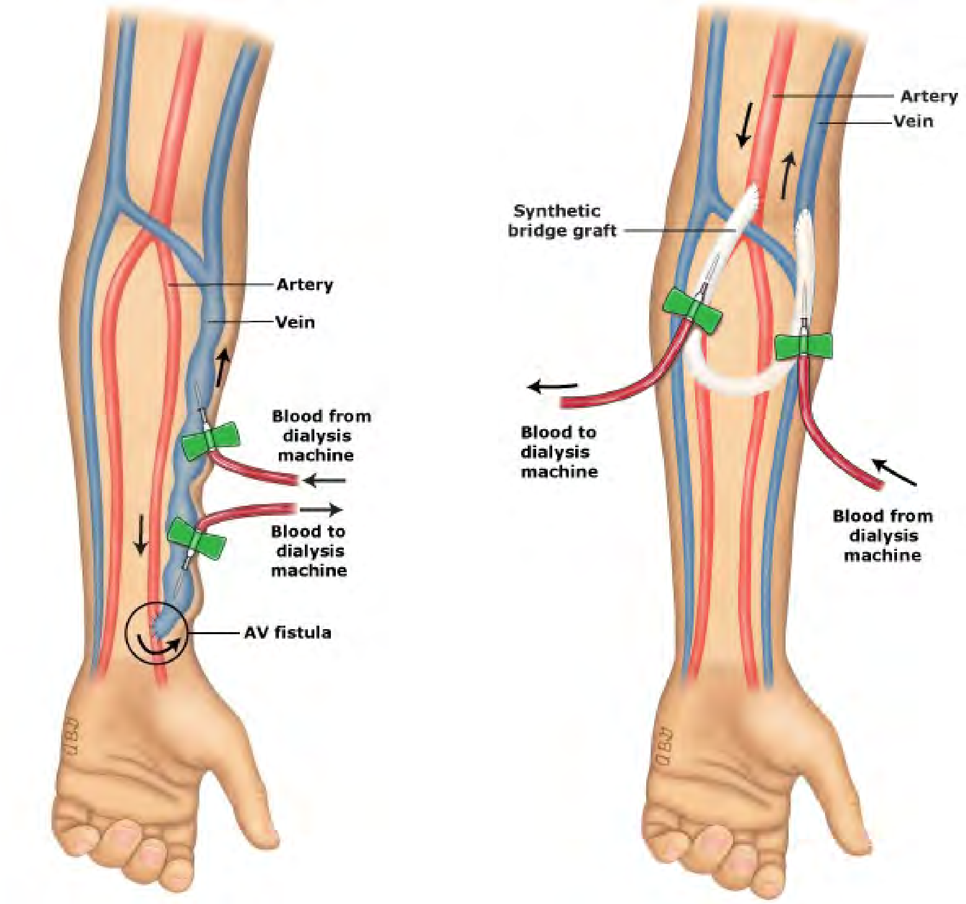

(a) Arteriovenous fistula (b) Arteriovenous graft

Figure 1.1: Illustrations arteriovenous shunts with cannula placement for haemodialysis: (a) of a lower arm arteriovenous fistula and (b) an upper arm arteriovenous graft (source: [15] and [16])

catheters include mechanical complications, infections and thrombotic episodes [20].

Prior studies have also shown that patients treated with catheters have inferior blood flow rates, more frequent hospitalisations and infections, higher related medical costs, as well as a lowered perception of their own health status [7]. Studies such as these have continually found that the overall performance of the AV approach is superior to the catheter approach and the latter has hence been discouraged, except in circumstances of need [21–24]. The National Kidney Foundation K-DOQI Practice Guidelines recommends that catheters be used in less than 10% of the dialysis patients because of their high complication rate [5].

Given their problems, catheter usage has reduced recently but remains prevalent with 20% of patients estimated to be dialysing by this method in 2011 [1, 24]. This is often as a result of ESRD being diagnosed at a late stage and immediate access with a

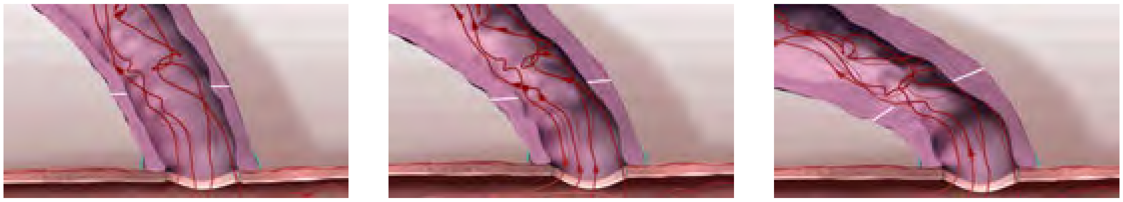

(a) Early-stage (b) Mid-stage (c) Late-stage

Figure 1.2: A depiction of the progression of stenosis by neointimal hyperplasia in the vein near the anastomosis (source: [28])

catheter is needed while waiting for a fistula or graft to mature. Catheters also remain an important access method in cases where AV access is highly likely to fail, has failed to mature, or has failed irreversibly after successful maturation [25, 26].

The form of AV access implemented is dependent on the vasculature, the age and health of the patient, and the preferences of the surgeon, among other things. Grafts are created by shunting an artery and vein with a length of prosthetic graft allowing for access in many positions across the body. Grafts require only 2-3 weeks of healing after surgery before being ready for cannulation, while for certain newer graft materials this may only take a matter of hours [1, 27]. A fistula is formed by suturing a vein directly to an artery in the upper arm or forearm, and takes between 3 to 6 months for the anastomosis, the surgical connection between the two structures, and the vein to mature for cannulation. Only three types of AVF can be formed, the radiocephalic, brachiocephalic and brachiobasilic fistula. The brachibasilic fistula, formed by the brachial artery and basilic vein, is one used less often as it is very difficult to cannulate [4].

With their versatility and short maturation times, grafts became the popular choice of AV access in the 1990s, when they constituted 70% of the total permanent access in the United States [29]. Numerous studies subsequently found that fistulas have overall the best long term patency rates, the lowest required intervention rate and are thus linked with the lowest costs to patients and the fewest number of deaths [7, 24, 30, 31]. As such the fistula has since been considered the first choice of access and in 2011 was found to be used in 60% of the dialysis population [5, 21, 29, 32, 33].

In situations where patients' veins and arteries are not suitable for fistula access or they cannot wait the long maturation period, a graft may be the best choice. Fistulas

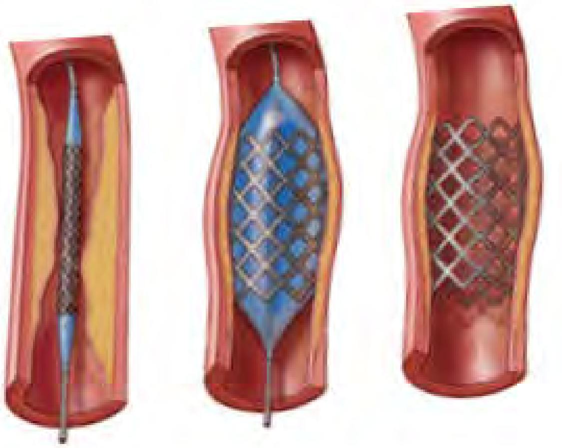

Figure 1.3: Depiction of fistula salvage by angioplasty and stent placement (source: [51])

have a higher likelihood of maturation failure, especially in older patients and those with diabetes [4]. Once matured however, the patency rates of fistulas increase drastically and are also more likely to remain patent for longer than other access methods, in some cases they can last for over ten years [34]. The average life of a graft is 2-3 years, while catheters on average have a short life span of only 12 months [5].

The vein walls in AV access experience abnormally high blood flow rates, pressures and shear stresses due to shunting and need to adapt successfully to remain patent. The increased flow and shear stresses lead to outward wall remodelling, described by Poiseuille's law, while the increases in pressure and hence tensile stress lead to wall thickening. Maturation failure, from early neointimal hyperplasia and insufficient or excessive vein adaptation, is the most common fistula dysfunction [35]. Numerous studies have also found that neointimal hyperplasia is responsible for the progression of venous outflow stenosis and eventual thrombosis and is the leading cause of access failure especially in grafts [29, 35–50]. The progression of neointimal hyperplasia stenosis is depicted in Figure 1.2.

Thrombosis can potentially be prevented by correcting mild outflow stenosis by angioplasty, illustrated in Figure 1.3, or surgical revision, returning venous blood flow rates and pressures to those sufficient for haemodialysis. Thrombosis itself can also be successfully treated with surgical embolectomy or thrombosis; however, the underlying stenosis also needs to be corrected or rapid re-thrombosis will occur. These interventions are however costly and only extend the life of the AV access and usually need to be repeated with increasing frequency [4].

Many approaches are being taken to better understand what haemodynamic factors lead to the aggresive and high rate of neointimal hyperplasia development found in haemodialysis patients. Although a number of *in-vivo* blood flow measuring techniques are available, they do not have a resolution capable of accurately determining the complex flow in access vessels. Recently much work has been done to numerically model the behaviour of blood flow in vascular access and other cardiovascular vessels. Computational fluid dynamics (CFD) simulations of patient-specific fistula have been able to approximate the haemodynamics at a high resolution and determine with relatively high accuracy, quantities such as pressure and wall shear stress (WSS) [34, 52–54]. These studies have also shown that abnormal flow recirculation and WSS conditions exist in fistulas in regions that correlate with neointimal development.

CFD models however do not capture the deformation of the vessel wall, decreasing the accuracy of the final results and possibly obscuring valuable flow information due to the interaction with highly-deformable solid media such as vessel tissue. Numerous numerical studies have incorporated vessel wall mechanics with FSI simulations to simulate more accurately regions of the cardiovascular system [55–65]. More recently a FSI study on a patient-specific fistula found that the effect of the wall compliance on the haemodynamics was non-negligible [66]. Their results showed that the velocities and WSS were overestimated by CFD simulations when compared with the FSI case. FSI models however take many times longer than CFD to simulate due to the added complexity of the vessel wall mechanics and in a large part due to the inherent instability in partitioned coupling techniques when dealing with these strongly-coupled problems [66–68].

Phase-contrast magnetic resonance angiography (PC-MRA) has also been used in cardiovascular time-dependent flow visualisation and quantification [70–73]. Velocity encoding MRI techniques have shown promise in their ability to determine the velocity distribution of the flow and hence approximate parameters such as WSS and pressure changes and to locate regions of stenosis [74, 75]. An example of the comparison between WSS vectors generated by a CFD simulation and that of a PC-MRA acquisition of blood flow through a carotid artery bifurcation is shown in Figure 1.4. Studies have however determined these parameters from acquisitions of blood flow in the larger arteries and veins where the resolution requirements are not as strict as they would be for smaller vessels such as those used in AV access. Increased resolution requires one or

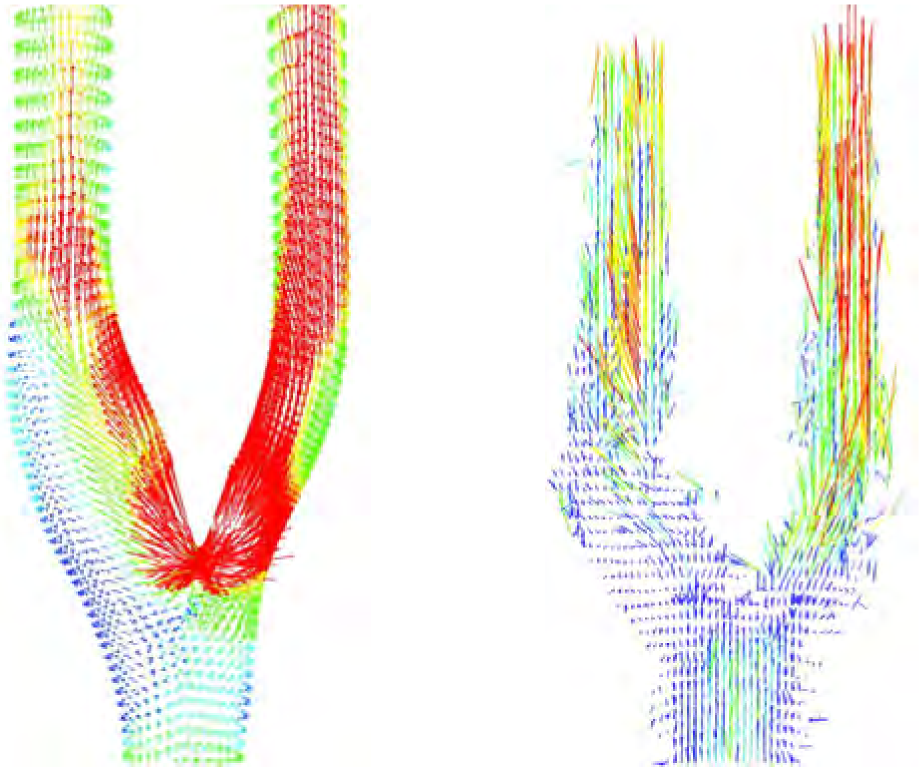
(a) CFD WSS vectors (b) PC-MRA WSS vectors

Figure 1.4: Comparison of the WSS vector distribution between a CFD simulation and a PC-MRA acquisition of a carotid artery bifurcation (source: [69])

more of the following depending on the scale: stronger magnetic fields, stronger field gradients and longer acquisition times. MRI has also been used to produce valuable data for the boundary conditions required in numerical models and to compare the accuracy of the modelled and measured data [54, 69, 76].

1.2 Aim and objectives

The objective of this thesis is the numerical investigation of the fluid dynamics and structural deformation of a patient-specific arteriovenous fistula. Various numerical methods and models are used to simulate aspects of the patient's vascular access under standard loading conditions. The blood flow through the anastomotic region is simulated by the partitioned coupling of two numerical methods, the finite element method (FEM) for the solid mechanics and the finite volume method (FVM) for the fluid mechanics.

The numerical model is developed and simulated within ANSYS® Academic Research, Release 16, a commercial multiphysics simulation package. Specifically, we aim to use ANSYS® Fluent® to model the blood flow and ANSYS® Mechanical™ to model the vessel walls. These two codes are coupled through the ANSYS® Workbench™ System Coupling component. The artery and vein are modelled as hyperelastic materials while the blood is assumed to behave as a Newtonian fluid.

The PC-MRA technique is assessed in terms of providing data for numerical modelling and determining the blood flow characteristics of the vascular access itself. We will also attempt to determine the near-optimal modelling schemes and range of parameters for stability and efficiency of the FSI model. The FSI and CFD models shall be quantitatively compared to determine the relative accuracy and efficiency between the two approaches.

Models such as the one developed in this work may provide valuable data for assessment and optimisation of fistula and grafts for current and future haemodialysis patients. Adjustments and improvements to these types of models may advance our understanding of the haemodynamics in vascular access and improve maturation patency, long-term patency and interventional strategies.

1.3 Outline

The structure of the rest of this work is as follows. In Chapter 2 we present the theory behind phase-contrast magnetic resonance angiography. The governing equations for nonlinear solid and fluid media are then introduced in Chapter 3 along with the constitutive relations for a hyperelastic material and a Newtonian fluid.

Chapter 4 is dedicated to the numerical methods used in our partitioned fluid-structure interaction. The first part of this chapter summarises the finite element method for materials experiencing large strain. The incompressible nature of the material is handled via an enhanced assumed strain field. We then introduce the finite volume method and a number of the underlying schemes and algorithms used in the pressure-based segregated solver. Chapter 4 concludes with a section on partitioned fluid-structure interaction coupling. This section starts by describing the features of a semi-implicit coupling algorithm and the modifications required to implement it in the finite volume method. The section ends with an explanation of the inherent numerical instability present in staggered coupling in FSI.

In Chapter 5, we turn to the implementation, results and analysis. We start by giving the details of the patient-specific acquisition and the data that was obtained. The method by which the geometry and mesh of the fluid region was developed for the patient-specific fistula is then described. We then detail the fluid model boundary conditions and setup. A mesh convergence analysis is then performed and the behaviour and results of the model are assessed. In the next section we do the same for the solid model while also comparing the performance of a number of element types. We then look at the fluid-structure interaction model in terms of its setup and give an analysis of the stability and performance of the method. The remainder of the chapter describes the results obtained and gives a comparative study against the fluid model.

The conclusions arising from this work and suggested areas for further research are presented in Chapter 6.

Chapter 2

Patient-specific data acquisition

The patient-specific fistula flow data were acquired from a PC-MRA sequence and a number of post-processing techniques to obtain a velocity field. In this chapter we briefly look at the theory of MRI and PC-MRA and highlight the generic techniques, sequences and post-processing requirements used in these methods. More details on this subject matter may be found in [77] for example.

2.1 Magnetic resonance imaging

In conventional MRI, radio waves and field gradients are imposed on a magnetic field to localise magnetic resonance in a body and produce a non-invasive picture of its internal structure from the processed signal data. Advantage is taken of the large number of protium atoms, the most common isotope of hydrogen, which have a considerable angular magnetic moment and are abundant in the water and fat in living tissue. The complex sequence of events can vary significantly between MRI techniques but is based on the basic underlying sequence described below. We will describe the basic sequence in terms a three-dimenstional Cartesian system with axes X, Y, and Z as the localising field gradients are applied in these directions.

2.1.1 Excitation

The MRI scanner produces a strong magnetic field $\boldsymbol{B}_0$, measured in teslas (T), along its axis, the Z-axis shown in Figure 2.1(a). This produces a net equilibrium magnetisation $\boldsymbol{M}_0$, proportional with the strength of the magnetic field. This occurs as a portion of the otherwise randomly spinning MR active nuclei in the magnetic field change the direction of the spin such that they precess in alignment with the magnetic field as shown in Figure 2.1(b). This occurs in accordance with the magnetic and angular momentum of each proton which do not precess in phase with one another, ensuring that the net magnetisation is fully longitudinal, i.e. $\boldsymbol{M}_Z = \boldsymbol{M}_0$, so that no resultant signal is generated by the mass of precessing protons. The proportion of aligned nuclei, and their precessional frequency ω_0 are proportional to the strength of the magnetic field. The angular frequency of the precession is given by the Larmor equation

$$\omega_0 = \lambda|\boldsymbol{B_0}| \tag{2.1}$$

where λ is the gyromagnetic ratio, a constant of proportionality for a specific nucleus.

Since the gyromatic ratio of protium (^{1}H) is 42.576 MHz/T^{-1}, radiofrequency (RF) waves can be used to induce resonance, or excitation, in these protons within the magnetic field. The excitation produces a short burst of electromagnetic energy and results in energy absorption by the precessing protons and a gain in phase coherence. The result of excitation is a net loss of longitudinal magnetisation and a net gain in transverse magnetisation $\boldsymbol{M}_{XY}$ as shown in Figure 2.1(c). The degree of transverse magnetisation is dependent on both the amplitude and duration of the radio RF pulse. An apodised sine 90° pulse at the Larmor frequency rotates the protons' spins into the transverse plane fully as shown in Figure 2.1(d).

On cessation of the RF pulse, the protons' frequency coherence decay back to their random state where longitudinal magnetisation regained, as indicated in Figure 2.1(c), this is known as T1 relaxation. Phase coherence loss also occurs and is due to random fluctuations in the local magnetic field and inhomogeneities throughout the magnetic field, this decay is known as T2 relaxation. Each tissue type has its own set of T1 and T2 relaxation times.

A receiver coil is able to pick up the signal from decaying spins, known as the free

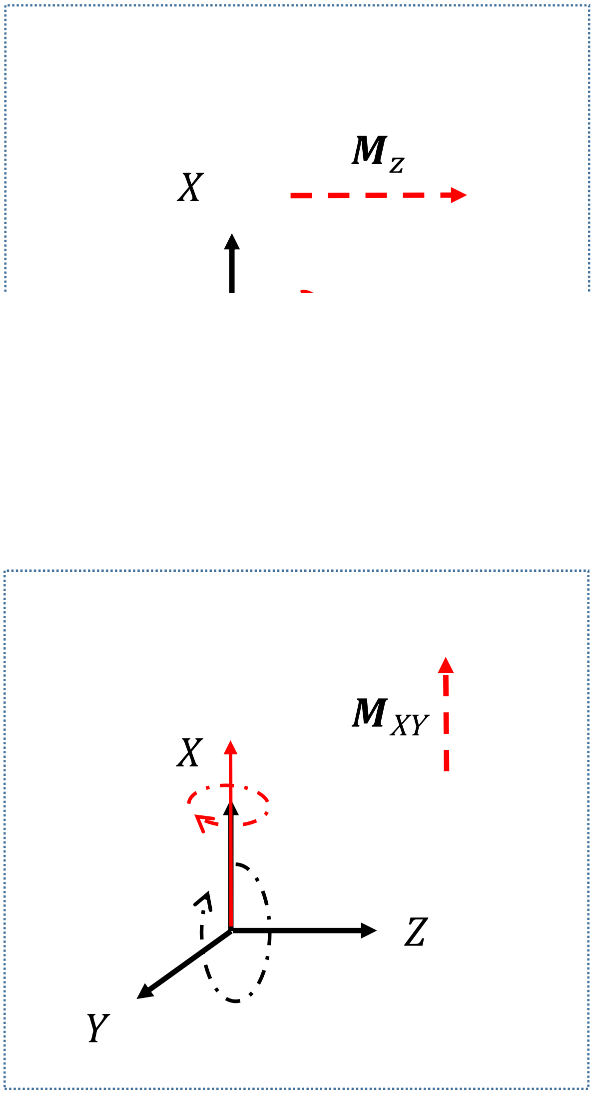

(d)

Figure 2.1: Magnetic field and excitation effects: (a) magnetic field direction and magnetisation (fully transverse), (b) proton spin precession and full transverse magnetisation, (c) excitation and decay of transverse magnetisation and proton spins, (d) resonance and full transverse magnetisation

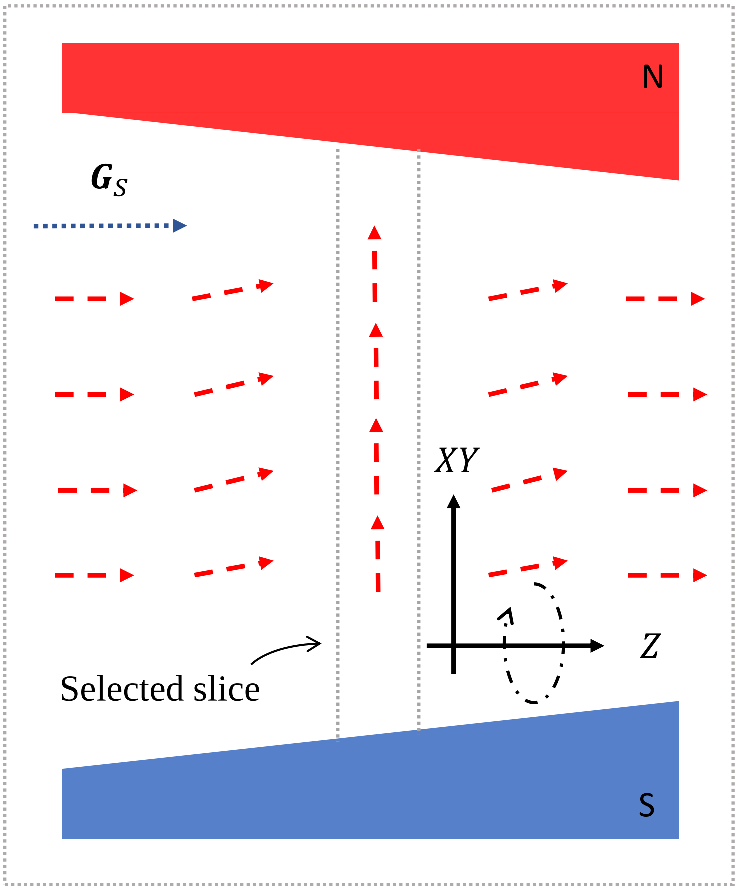

Figure 2.2: An RF pulse and a slice selection gradient along the Z-axis causes causes net magnetisation of protons in the slice to “tip” fully in the transverse (XY) plane

induction decay (FID) signal. At this point however one cannot differentiate between the signals and determine their location. A complex set of magnetic field adjustments and RF pulses is needed to give the signal positional information.

2.1.2 Signal localisation

A slice selection, frequency encoding, and phase encoding gradient perpendicular to one another are used to assign spatial localisation to the FID. An image in the XY plane is produced by a slice selection gradient along the Z-axis and assigns location in this direction. The frequency and phase encoding gradients can then be applied along the X and Y, or Y and X directions respectively to assign location in the XY-plane.

Applying a magnetic field gradient along the Z-axis at the same time as the 90° RF pulse induces resonance only in protons in a narrow region along the XY plane as illustrated in Figure 2.2. This gradient is known as the slice selection gradient

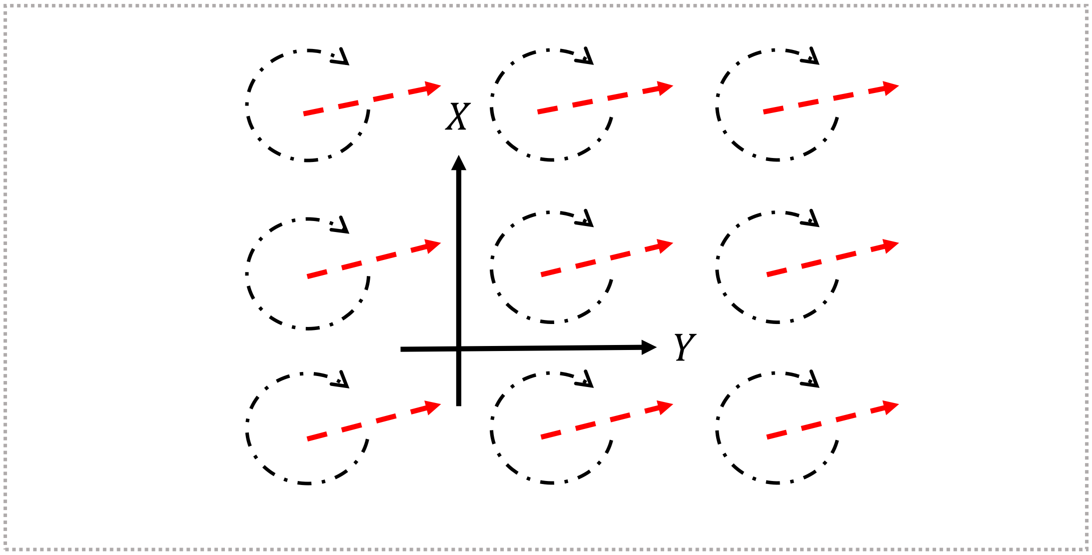

Figure 2.3: Slice selection causes spins to precess in phase and at the same frequency throughout the selected slice

(G_s) and is the first step in generating an image in the chosen plane. All atoms within the slice resonate in phase and with the same frequency as shown in Figure 2.3. The slice selection gradient is turned off as soon as the RF pulse is complete, so that precessional frequency and phase alignment start to decay and net transverse magnetisation decreases.

A phase encoding gradient (G_ϕ) is then applied perpendicular to the slice selection gradient, in this example along the Y-axis. This magnetic gradient is applied for a short duration directly after slice selection but right before data acquisition and encodes a phase gradient to spins, proportional to the magnetic field, along the Y-axis localising spins in this direction. The effect of the phase encoding gradient pulse is illustrated in Figure 2.4.

A frequency-encoding gradient (G_f) is applied directly after the phase encoding gradient pulse and for the duration of the data acquisition along the X-axis. This magnetic gradient imparts a frequency gradient along the X-axis and localising the spins this direction as depicted in Figure 2.5. With use of the Fourier transform, the frequency gradient can be translated into differences in signal at each spatial location along the X-axis.

Along the phase-encoding axis, spatial localisation usually requires the application a

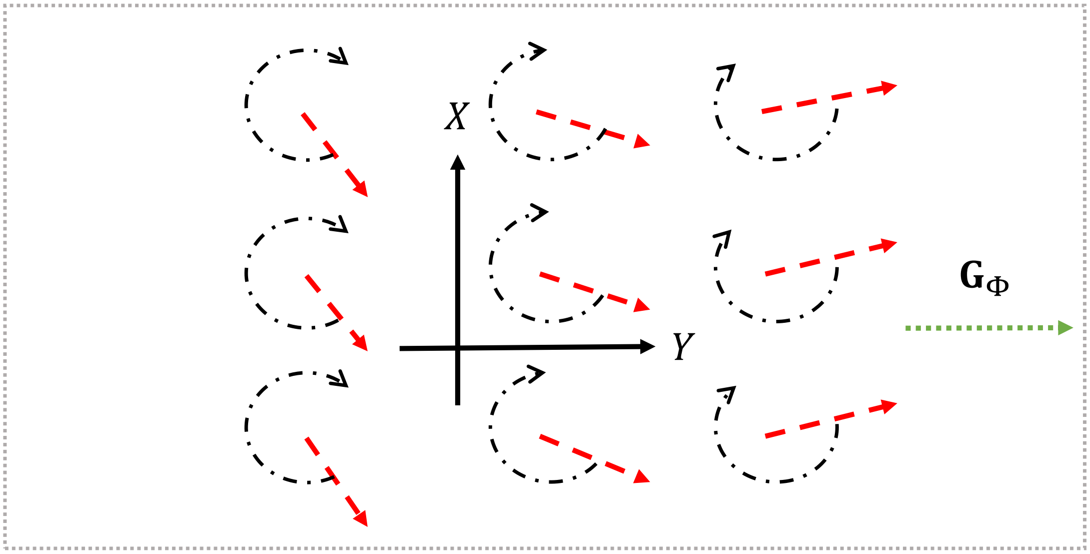

Figure 2.4: A short phase encoding gradient along the Y-axis imparts a corresponding a phase gradient to proton spins as they start to decay

number of RF excitations at varying phase-encoding gradient strengths. The number of phase-encoding steps required determines the extent of the MR image along the y-axis. This contributes to image acquisition time, along with the Time to Repetition (TR), and the time between consecutive excitation pulses. The basic MRI sequence for signal localisation is shown in Figure 2.6.

2.1.3 Gradient-recalled Echo

To generate a useful FID signal the proton spins need to be in phase at just the right moment. Spatial gradients, however, cause phase shifts to accumulate over time. To correct for this, reverse gradients are used to regain phase coherence. This generates an echo, referred to as a gradient-recalled echo.

This is accomplished by applying a gradient with two lobes that have opposite polarity. The first lobe of the gradient is the dephasing lobe. A second gradient is then applied with opposite polarity and typically twice the duration, called a rephasing lobe. At the midpoint of this rephasing lobe, the sampled protons are most in phase and an echo is generated, referred to as a gradient-recalled echo (GRE).

The time to echo (TE) is the time between the excitation pulse and the measurement of the signal. GRE acquisitions allow for decreased RF power deposition and shorter TR, reducing imaging time considerably. Gradient-recalled echos form the basis of the

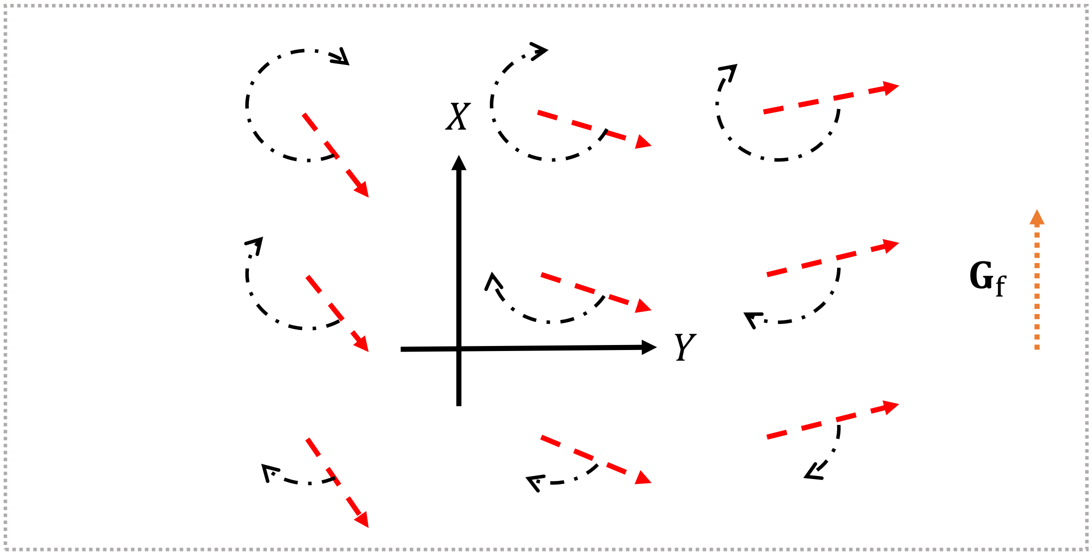

Figure 2.5: Frequency encoding gradient along the X-axis imparts a corresponding a frequency gradient to proton spins as they decay

PC-MRA technique which is described in Section 2.2.

2.1.4 Image contrast

The tissue relaxation times are used to determine the length between successive RF pulses and subsequently create contrast between tissue types taking into account that the image contrast is also dependant on the proton density of the tissue.

The tissues in the body have different timing constants which are determined by the size and movement of the molecules in the tissue. These timing constants are used to create contrast by controlling TR and TE of the pulse sequence. In MRA techniques blood flow is used to create contrast by a number of different methods.

The signal from the FID is captured and stored for each of the phase encoding gradient strengths. The signal data is processed by a Fourier transform in the frequency encoding direction and then in the phase encoding direction to localise the signals and extract an image. The images then usually need to be post-processed to smooth out noise and fix a number of other artefacts.

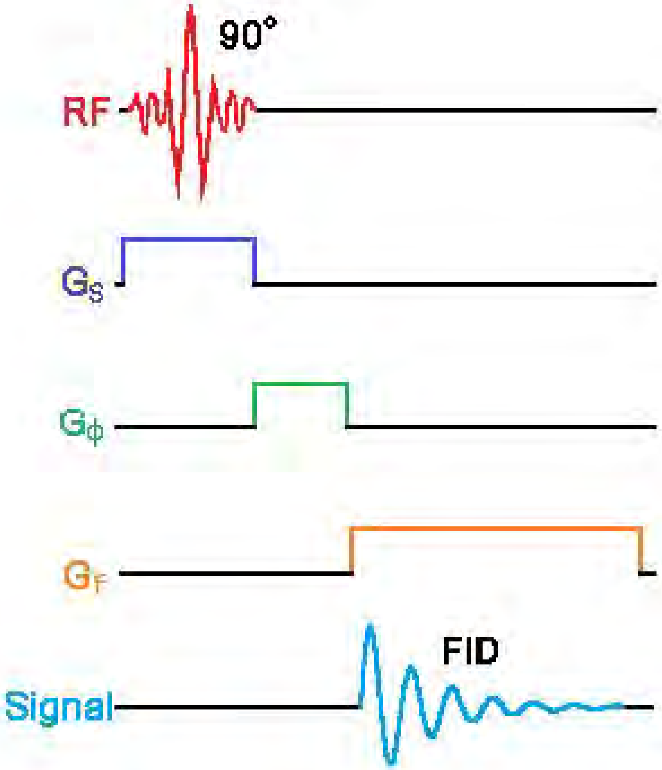

Figure 2.6: The basic MRI sequence for signal localisation (adapted from [78])

2.2 Phase-contrast magnetic resonance angiography

Phase contrast is an excellent method to noninvasively obtain flow information in patients with cardiac shunts due to its adjustable sensitivity to various flow rates [79]. It is the most sensitive sequence for detecting slow-flowing blood, and is the only MRA technique whereby velocity, flow, and pressure can be ascertained [80]. It is thus sensitive to turbulent flow that can be associated with vascular stenoses and can be used to identify thrombosis [81].

In phase-contrast MR angiography pairs of bipolar GREs are used to generate flow-sensitive phase images. Protons are velocity encoded by the dephasing and the rephasing lobes of the bipolar gradient which are identical in magnitude and time, but exactly opposite in direction. The movement of a proton causes it to experience a different field strength, and hence net phase change, from each lobe relative to stationary protons [81].

Nonmoving protons however do experience phase changes due to magnetic field inhomogeneities [81]. To account for this a second reversed bipolar gradient equal in magnitude is applied directly after the first (back-to-back bipolar gradients with reversed order). This subtracts the unwanted equal but opposite phase changes from the magnetic field inhomogeneities and doubles the phase change from proton motion. The total net phase change $\Delta\phi$ from the pair of bipolar gradients is given by

$$\Delta\phi = \pi\lambda\,\frac{v_{dir}}{v_{enc}} \tag{2.2}$$

where v_{dir} is the component of velocity perpendicular to the scanned plane and v_{enc} is dependent on the magnitude and duration of the applied gradient. This is set to calibrate the phase change according to the expected measured velocities. Velocities above v_{enc} wrap past 180 degrees resulting in aliasing, otherwise known as phase wrapping.

The need for an additional bipolar gradient means that acquisition times are at least twice as long as other MRA techniques. Furthermore, proton movement is detected only in one direction at a time. To obtain flow in two or three dimensions the sequence needs to be repeated in each direction.

Since this MRA sequence is effectively a GRE sequence and all echoes contain both magnitude and phase information, additional anatomic information can also be determined from the FID. The gradient echo method is also used in data acquisition acceleration for 2D slices and to image multiple 2D slices at the same time for 3D acquisitions. A typical PC-MRA sequence is illustrated in Figure 2.7.

Cardiac gating is used to obtain dynamic information throughout the cardiac cycle. Gating techniques are required to improve temporal resolution and minimize imaging artefacts caused by cardiac motion. This is especially important since phase contrast imaging is by its nature very sensitive to motion degradation. If the patient moves during any of the acquisitions however, the sequence usually cannot be used.

Arterial blood flow is pulsatile with high peak flow rates so that the v_{enc} is usually chosen to be greater than 1 $\mathrm{m\,s^{-1}}$ and can be as high as 3 or 4 $\mathrm{m\,s^{-1}}$ depending on the vessel or on the degree of stenosis present [80]. The closer the v_{enc} value is to the measured velocity, the more accurate the measurement giving PC-MRA adjustable accuracy. This ability makes phase contrast angiography the most sensitive MR sequence for the detection of slow-flowing blood.

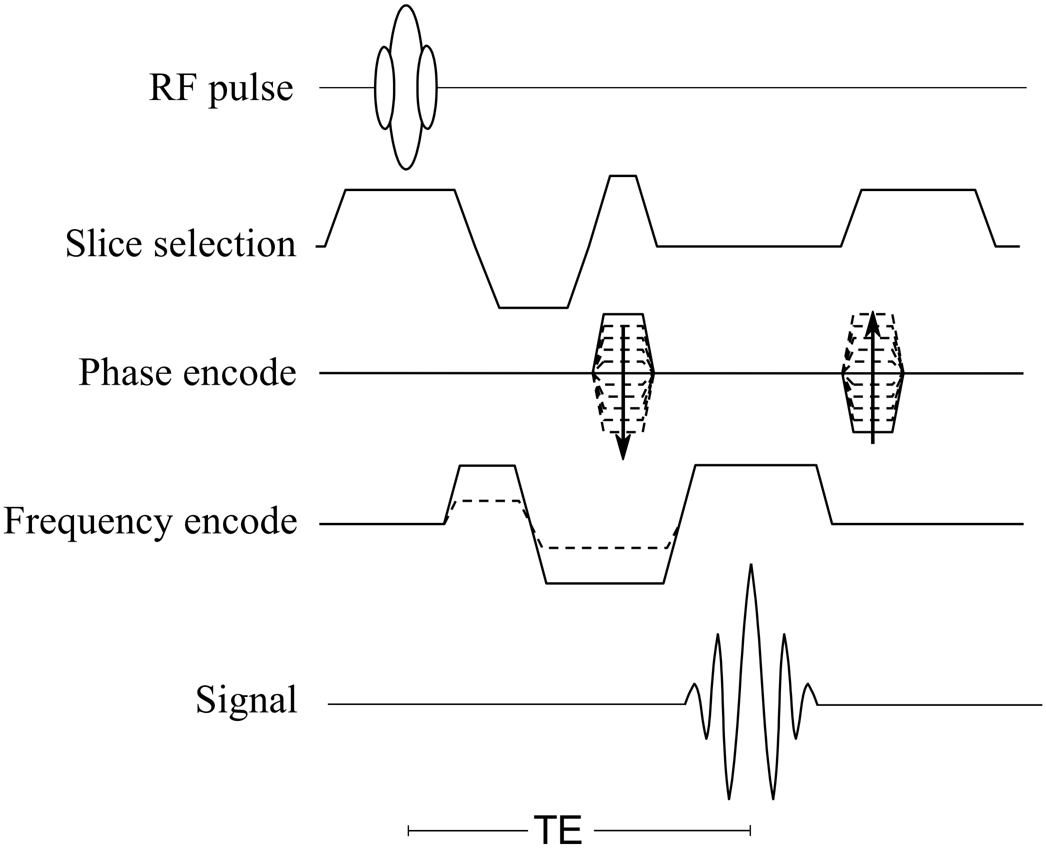

Figure 2.7: An example of a fast GRE pulse sequence with velocity encoding. The dotted lines show the flow encoding gradients for the frequency encoding axis while the arrows show the change in strength of the phase encoding gradient (adapted from [82] and [83])

To detect the full range of blood flow velocities spatially and temporally to a higher degree of accuracy, the v_{enc} parameter can be set lower than the expected maximum velocity also reducing the signal to noise ratio, a number of unwrapping algorithms can then be used to fix the artefacts from aliasing. These methods may however fail to unwrap the data adequately in cases where the spatial resolution or the v_{enc} are too low or other sources of noise are too high [84].

Chapter 3

Nonlinear continuum mechanics

In continuum mechanics a macroscopic approach to material behaviour is taken, whereby it is assumed that a body has a distribution of matter which is continuous in space and time. Furthermore, properties of the body are assumed to vary smoothly as functions of space and time. An abridged description of continuum mechanics is given as a basis for the governing equations and constitutive models used in setting up the coupled numerical model in the next chapter. For a more in-depth description the reader is referred to [85].

3.1 Notation

In this text scalar quantities are denoted by lower-case Greek symbols, vectors and second-order tensors by bold-face Roman letters, and fourth-order tensors by blackboard Roman letters:

0th-order	ρ, ψ
1st- and 2nd-order	$\boldsymbol{F}$, $\boldsymbol{u}$, $\boldsymbol{b}$
4th-order	$\mathbb{I}$, $\mathbb{C}$

The components of a tensor are defined with respect to a fixed orthonormal basis $\boldsymbol{e}_i$, $i = 1, 2, 3$. Components of tensors are given in index notation as:

0th-order	ρ
1st-order	u_i
2nd-order	b_{ij}
4th-order	$\mathbb{c}_{ijkl}$

The gradient of a second-order tensor field $\boldsymbol{A}(\boldsymbol{x})$ is a third-order tensor grad $\boldsymbol{A}$ with components

$$\frac{\partial A_{ij}}{\partial x_k} = A_{ij,k} \tag{3.1}$$

while the divergence of $\boldsymbol{A}$ is the vector with components

$$(\text{div } \boldsymbol{A})_i = \frac{\partial A_{im}}{\partial x_m} = A_{im,m}. \tag{3.2}$$

Here and elsewhere an index following a comma denotes partial differentiation with respect to that component.

The principal scalar invariants of $\boldsymbol{A}$ are given by

$$I_1(\boldsymbol{A}) = \text{tr}(\boldsymbol{A}), \tag{3.3}$$

$$I_2(\boldsymbol{A}) = \frac{1}{2}\left((\text{tr}(\boldsymbol{A}))^2 - \left(\text{tr}(\boldsymbol{A})^2\right)\right), \tag{3.4}$$

$$I_3(\boldsymbol{A}) = \det(\boldsymbol{A}), \tag{3.5}$$

where $\det(\boldsymbol{A})$ denotes the determinant of $\boldsymbol{A}$ and $\text{tr}(\boldsymbol{A})$ is defined by

$$\text{tr}(\boldsymbol{A}) = A_{ii}. \tag{3.6}$$

3.2 Kinematics

The undeformed and deformed states of a body are respectively referred to as the reference and spatial configurations. Both are described with respect to the same right handed coordinate axes with orthonormal basis vectors $\boldsymbol{e}_i$.

The body occupies a region B_0 in $\mathbb{R}^3$ in its initial configuration at time t_0, and is bounded by the surface ∂B_0. At time t the body occupies the region B with boundary ∂B. The position vector $\boldsymbol{X}$ of a material particle in B_0 is mapped to its current position $\boldsymbol{x}$ by the motion $\boldsymbol{\chi}$:

$$\boldsymbol{x} = \boldsymbol{\chi}(\boldsymbol{X}, t).$$

It is assumed that the motion is invertible, so that

$$\boldsymbol{X} = \boldsymbol{\chi}^{-1}(\boldsymbol{x}, t). \tag{3.7}$$

The displacement field is given by

$$\boldsymbol{U}(\boldsymbol{X}, t) = \boldsymbol{\chi}(\boldsymbol{X}, t) - \boldsymbol{X}. \tag{3.8}$$

This is a vector field and is given as a function of the reference position and time. In the spatial form the displacement vector is described by

$$\boldsymbol{u}(\boldsymbol{x}, t) = \boldsymbol{x} - \boldsymbol{\chi}^{-1}(\boldsymbol{x}, t). \tag{3.9}$$

Quantities with text in upper case Roman are reserved for reference configuration quantities while Roman lower case are reserved for spatial configuration quantities in this text. The position and displacement vectors are illustrated in Figure 3.1.

It is convenient to describe the material behaviour and perform calculations of large strain solid models with respect to the reference configuration. This is called the Lagrangian approach which is normally used in solid mechanics with the equations used in the form where they are only functions of $\boldsymbol{X}$ and $\boldsymbol{t}$. The Eulerian description is preferred in fluid mechanics where the spatial formulation of the governing equations are used such that they functions of $\boldsymbol{x}$ and $\boldsymbol{t}$. The spatial and material formulations of the governing equations are equivalent and can be mapped back and forth between configurations.

The deformation gradient maps infinitesimal elements between the reference and cur-

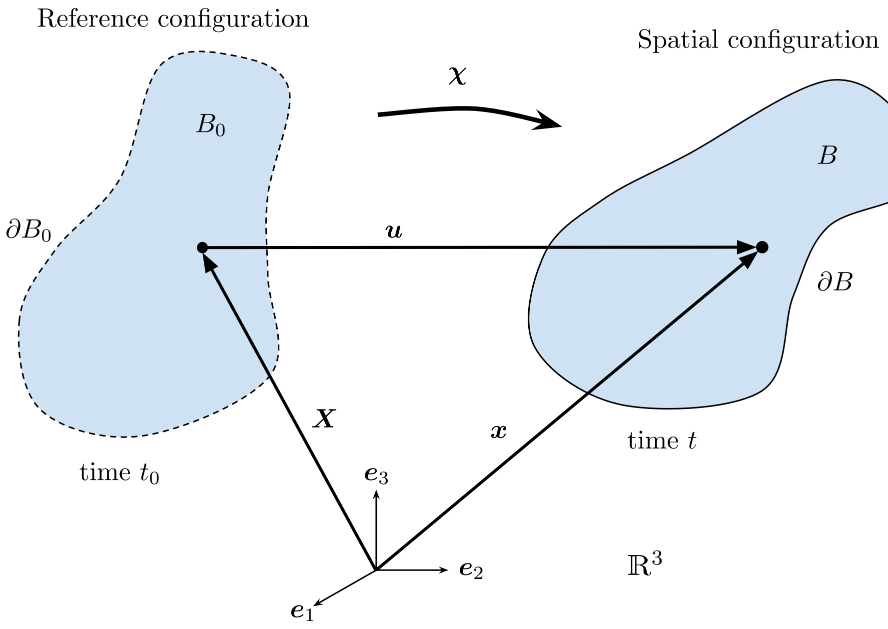

Figure 3.1: Position and displacement vectors for body in motion from reference configuration to spatial configuration

rent configurations such that

$$\mathrm{d}x_i = \frac{\partial \boldsymbol{\chi}_i}{\partial X_A}\, \mathrm{d}X_A. \tag{3.10}$$

The deformation gradient is derived from the material gradient of the spatial position field $\boldsymbol{x}$

$$\boldsymbol{F}(\boldsymbol{X}, t) = \frac{\partial \boldsymbol{\chi}}{\partial \boldsymbol{X}} = \mathrm{Grad}\ \boldsymbol{\chi} = \mathrm{Grad}\ \boldsymbol{U} + \boldsymbol{I}. \tag{3.11}$$

In index notation this is written as

$$F_{iJ} = \boldsymbol{\chi}_{i,J} = U_{i,J} + \delta_{iJ}. \tag{3.12}$$

An important measure in kinematics is the Jacobian which relates an infinitesimal volume element $\mathrm{d}V$ in the material configuration to its counterpart $\mathrm{d}v$ in the spatial configuration according to

$$J(\boldsymbol{X}, t) = \frac{\mathrm{d}v(\boldsymbol{x}, t)}{\mathrm{d}V(\boldsymbol{X}, t)} = \det(\boldsymbol{F}) \tag{3.13}$$

Deformations where $J \leq 0$ produce zero or negative volumes of the body during the motion. Only motions where $J > 0$ are therefore permitted, ensuring the impenetrability of matter in the continuous sense.

The following symmetric strain measures are used in this work: The right Cauchy-Green stretch tensor:

$$\boldsymbol{C}(\boldsymbol{X}, t) = \boldsymbol{F}^T \boldsymbol{F}; \tag{3.14}$$

The left Cauchy-Green stretch tensor:

$$\boldsymbol{b}(\boldsymbol{X}, t) = \boldsymbol{F}\,\boldsymbol{F}^T; \tag{3.15}$$

The Green-Lagrange strain tensor:

$$\boldsymbol{E}(\boldsymbol{X}, t) = \frac{1}{2}\left(\boldsymbol{C} - \boldsymbol{I}\right); \tag{3.16}$$

The Euler-Almansi strain tensor:

$$\boldsymbol{\varepsilon}(\boldsymbol{X}, t) = \frac{1}{2}\left(\boldsymbol{I} - \boldsymbol{b}^{-1}\right). \tag{3.17}$$

The material time derivative is the rate of change with respect to time of a quantity at a fixed material point, and for a tensor field $\boldsymbol{\Phi}$ is defined as

$$\dot{\boldsymbol{\Phi}} = \frac{\mathrm{D}\boldsymbol{\Phi}}{\mathrm{Dt}} = \left(\frac{\partial \boldsymbol{\Phi}}{\partial \mathrm{t}}\right)_{\boldsymbol{X}}. \tag{3.18}$$

The material time derivative of a spatial tensor field $\boldsymbol{\Phi}(\boldsymbol{x}, t)$ is thus given by

$$\dot{\boldsymbol{\Phi}}\,(\boldsymbol{x}, t) = \frac{\partial \boldsymbol{\Phi}(\boldsymbol{x}, t)}{\partial \mathrm{t}} + \Big(\mathrm{grad}\ \boldsymbol{\Phi}(\boldsymbol{x}, t)\Big)\boldsymbol{v}(\boldsymbol{x}, t). \tag{3.19}$$

where grad $\boldsymbol{\Phi}(\boldsymbol{x}, t)$ is the spatial gradient

$$\mathrm{grad}\ \boldsymbol{\Phi}\,(\boldsymbol{x}, t) = \frac{\partial \boldsymbol{\Phi}(\boldsymbol{x}, t)}{\partial \boldsymbol{x}}, \tag{3.20}$$

or in index form,

$$\left(\mathrm{grad}\ \boldsymbol{\Phi}\,(\boldsymbol{x}, t)\right)_{ijk} = \boldsymbol{\Phi}_{ij,k}. \tag{3.21}$$

Since $\boldsymbol{a} = \dot{\boldsymbol{v}}$, the acceleration field can be determined from the velocity field without knowing the motion explicitly. This is a crucial element of the Eulerian formulation for fluids.

The velocity gradient and rate of deformation are given respectively by

$$\boldsymbol{l}(\boldsymbol{x}, t) = \text{grad } \boldsymbol{v}, \tag{3.22}$$

$$\boldsymbol{d}(\boldsymbol{x}, t) = \tfrac{1}{2} \left(\boldsymbol{l} + \boldsymbol{l}^T \right). \tag{3.23}$$

3.3 Stress measures

Cauchy's stress theorem states that the traction vector $\boldsymbol{t}$ on an infinitesimal surface element d$\boldsymbol{a}$ with normal $\boldsymbol{n}$ at a point in or on body B is given by

$$\boldsymbol{t} \left(\boldsymbol{x}, t, \boldsymbol{n} \right) = \boldsymbol{\sigma} \left(\boldsymbol{x}, t, \boldsymbol{n} \right) \boldsymbol{n} \tag{3.24}$$

where $\boldsymbol{\sigma}$ is the Cauchy stress tensor. The first Piola-Kirchhoff stress tensor $\boldsymbol{P}$ which relates the traction in the deformed configuration to the surface element d$\boldsymbol{A}$ with normal $\boldsymbol{N}$ in the reference configuration is defined such that

$$\boldsymbol{\sigma}\, \boldsymbol{n} \ \mathrm{d}a = \boldsymbol{P} \left(\boldsymbol{X}, t, \boldsymbol{N} \right) \boldsymbol{N} \ \mathrm{d}A. \tag{3.25}$$

Since the surface element in the spatial configuration is related to its counterpart in the reference configuration by

$$\boldsymbol{n} \ \mathrm{d}a = J\, \boldsymbol{F}^{-T}\, \boldsymbol{N} \ \mathrm{d}A, \tag{3.26}$$

the first Piola-Kirchoff stress is related to the Cauchy stress by the identity

$$\boldsymbol{P} = J\, \boldsymbol{\sigma}\, \boldsymbol{F}^{-T}. \tag{3.27}$$

The second Piola-Kirchhoff stress tensor $\boldsymbol{S}$ is defined by

$$\boldsymbol{S} = \boldsymbol{F}^{-1}\,\boldsymbol{P}. \tag{3.28}$$

This is a very useful stress measure in solid mechanics since it is symmetric and parametrised by material coordinates.

3.4 Conservation laws

3.4.1 Conservation of mass

Since mass can neither be created nor destroyed, the rate of change of mass of a material volume is zero: that is,

$$\frac{\mathrm{D}}{\mathrm{D}t}\int_P \rho(\boldsymbol{x}, t)\ \mathrm{d}v = 0, \tag{3.29}$$

where P is any part of the body. In the material description the material time derivative can be brought into the integral: that is,

$$\frac{\mathrm{D}}{\mathrm{D}t}\int_{P_0} \rho J\ \mathrm{d}V = \int_{P_0} \frac{\partial}{\partial t}\rho J\ \mathrm{d}V = 0 \tag{3.30}$$

from this the point-wise mass conservation equation is obtain in the form

$$\dot{\rho} + \rho\,\mathrm{div}\ \boldsymbol{v} = 0 \tag{3.31}$$

For an incompressible material conservation of mass reduces to the incompressibility condition

$$\mathrm{div}\ \boldsymbol{v} = 0. \tag{3.32}$$

3.4.2 Conservation of momentum

Balance of linear momentum states that the rate of change of linear momentum of any part of a body equals the applied force on that part. That is,

$$\frac{\mathrm{D}}{\mathrm{D}t}\int_P \rho(\boldsymbol{x},t)\boldsymbol{v}\ \mathrm{d}v = \int_P \boldsymbol{f}\mathrm{d}v + \int_{\partial P} \boldsymbol{t}\ \mathrm{d}a. \tag{3.33}$$

This reduces to

$$\int_P \rho\dot{\boldsymbol{v}}\ \mathrm{d}v = \int_P \boldsymbol{f}\ \mathrm{d}v + \int_{\partial P} \boldsymbol{\sigma n}\ \mathrm{d}a \tag{3.34}$$

from which we obtain Cauchy's first equation of motion

$$\mathrm{div}\ \boldsymbol{\sigma} + \boldsymbol{f} = \rho\dot{\boldsymbol{v}}. \tag{3.35}$$

In the material configuration where the body force is given by $\boldsymbol{B} = J\boldsymbol{f}$, the equation of motion is given by

$$\mathrm{Div}\boldsymbol{P} + \boldsymbol{B} = \rho_0\dot{\boldsymbol{V}}. \tag{3.36}$$

Balance of angular momentum states that the rate of change of angular momentum is equal to the total applied moment. This reduces to the symmetry condition

$$\boldsymbol{\sigma} = \boldsymbol{\sigma}^T. \tag{3.37}$$

3.5 Constitutive relations

So far the governing equations have been developed independent of the material characteristics. A constitutive relation (material model) is required to relate the stress state of the body to its motion or state of strain. We are interested in hyperelastic behaviour for solids and Newtonian behaviour for fluids.

3.5.1 Hyperelasticity

A hyperelastic material has a strain energy function $\varPsi$ that is a function of deformation only, so that

$$\varPsi = \varPsi(\boldsymbol{F}). \tag{3.38}$$

From material frame indifference the strain energy function can also be given in terms of the right Cauchy-Green or Green-Lagrange strain tensors: that is,

$$\varPsi(\boldsymbol{F}) = \varPsi(\boldsymbol{C}) = \varPsi(\boldsymbol{E}). \tag{3.39}$$

Furthermore, for an isotropic material the dependence is on the principal invariants of its arguments, so that

$$\varPsi = \varPsi\Big[I_1(\boldsymbol{C}), I_2(\boldsymbol{C}), I_3(\boldsymbol{C})\Big]. \tag{3.40}$$

For incompressible materials we have $J = I_3 = 1$. To enforce this constraint on the deformation, the strain-energy function may be modified by adding the constraint term $p(J-1)$, where p is a Lagrange multiplier. This gives

$$\varPsi = \varPsi\Big[I_1(\boldsymbol{C}), I_2(\boldsymbol{C})\Big] - \frac{p}{2}\Big[I_3(\boldsymbol{C}) - 1\Big]. \tag{3.41}$$

From the second law of thermodynamics a reversible isothermal process is found to have zero internal dissipation such that

$$\dot{\varPsi} = J\,\boldsymbol{\sigma} : \dot{\boldsymbol{d}} \quad \text{or} \quad \dot{\varPsi} = \boldsymbol{P} : \dot{\boldsymbol{F}} \tag{3.42}$$

holds for every admissible process, where $J\boldsymbol{\sigma} : \dot{\boldsymbol{d}} = \boldsymbol{P} : \dot{\boldsymbol{F}}$ is the stress power per unit referential volume (see Section 3.2 for material time derivative definitions). From the time differentiation of the strain energy function we get

$$\frac{\partial\varPsi(\boldsymbol{F})}{\partial\boldsymbol{F}} : \dot{\boldsymbol{F}} = \boldsymbol{P} : \dot{\boldsymbol{F}}. \tag{3.43}$$

Since $\dot{\boldsymbol{F}}$ is arbitrary we obtain the elasticity relation

$$\boldsymbol{P} = \frac{\partial \Psi(\boldsymbol{F})}{\partial \boldsymbol{F}} - p\,\frac{\partial J}{\partial \boldsymbol{F}}, \tag{3.44}$$

and in terms of the Cauchy stress tensor

$$\boldsymbol{\sigma} = \boldsymbol{\sigma}' - p\,\boldsymbol{I} = J^{-1}\,\frac{\partial \Psi(\boldsymbol{F})}{\partial \boldsymbol{F}}\,\boldsymbol{F}^T - p\,\boldsymbol{I}. \tag{3.45}$$

The Yeoh model [86] is an isotropic hyperelastic material model used for rubber-like materials with typical stress stiffening effect in the large strain domain. The incompressible material model has a strain energy that is a function of the first strain invariant I_1 only. The generalised form of the incompressible Yeoh model is

$$\Psi = \sum_{i=1}^{n} c_i \left(I_1 - 3\right)^i \tag{3.46}$$

where c_i are material constants such that $2c_1$ can be interpreted as the initial shear modulus. This produces a convex strain-energy function that increases monotonically with I_1. The Yeoh model has the consistency condition $2c_1 = G$, where G is the shear modulus. The original model proposed by Yeoh will be used with $n = 3$. The stress relation for the incompressible Yeoh model is given by

$$\boldsymbol{\sigma} = 2\left[c_1 + 2c_2\left(I_1 - 3\right) + 3c_3\left(I_1 - 3\right)^2\right]\boldsymbol{b} - p\,\boldsymbol{I}. \tag{3.47}$$

3.5.2 Newtonian fluids

The Newtonian fluid model is a good approximation for many fluids and assumes that the stress is proportional to the rate of deformation:

$$\boldsymbol{\sigma} = 2\mu\boldsymbol{d} + \lambda \mathrm{tr}\left(\boldsymbol{d}\right)\boldsymbol{I}. \tag{3.48}$$

Here μ is the coefficient of shear viscosity or dynamic viscosity. The second constant of proportionality λ is termed the second viscosity which relates stress to volumetric deformation. In the incompressible limit $\lambda \longrightarrow \infty$ and $\mathrm{tr}\left(\boldsymbol{d}\right) = 0$, to account for the unknown hydrostatic pressure $\lambda\mathrm{tr}\,(\boldsymbol{d})$ is replaced so that the Cauchy stress is given by

$$\boldsymbol{\sigma} = 2\mu\boldsymbol{d} - p\boldsymbol{I} \tag{3.49}$$

where p is the static pressure, often referred to only as the pressure in fluid mechanics. This is accompanied by equation (3.32).

3.6 Boundary conditions

3.6.1 Solid model

The Dirichlet boundary condition imposes displacements

$$\boldsymbol{u}(\boldsymbol{x}, t) = \bar{\boldsymbol{u}} \quad \text{on} \quad \partial B_u \tag{3.50}$$

and the Neumann boundary condition imposes tractions

$$\boldsymbol{\sigma}(\boldsymbol{x}, t) \cdot \boldsymbol{n} = \bar{\boldsymbol{t}} \quad \text{on} \quad \partial B_t. \tag{3.51}$$

A Robin boundary condition is a weighted combination of Dirichlet and Neumann boundary conditions and acts to impede displacements and changes in displacement of the boundary. The most basic form of Robin boundary condition essentially states that the surface traction is proportional to the displacement on the boundary and is given by

$$\boldsymbol{\sigma}(\boldsymbol{x}, t)\boldsymbol{n} = -k\boldsymbol{u} \quad \text{on} \quad \partial B_r, \tag{3.52}$$

where k is the spring constant or foundation stiffness. The boundaries ∂B_u, ∂B_t, and ∂B_r form complementary parts of ∂B, that is

$$\partial B_u \cup \partial B_t \cup \partial B_r = \partial B, \tag{3.53}$$

$$\partial B_u \cap \partial B_t = \partial B_u \cap \partial B_r = \partial B_t \cap \partial B_r = \emptyset. \tag{3.54}$$

3.6.2 Fluid model

The Dirichlet boundary condition enforces velocities on part of the control surface $\partial\Omega$

$$\boldsymbol{v}(\boldsymbol{x},t) = \bar{\boldsymbol{v}} \quad \text{on} \quad \partial\Omega_v \tag{3.55}$$

and the Neumann boundary condition imposes tractions

$$\boldsymbol{\sigma}(\boldsymbol{x},t)\boldsymbol{n} = \bar{\boldsymbol{t}} \quad \text{on} \quad \partial\Omega_t \tag{3.56}$$

where $\partial\Omega_v$ and $\partial\Omega_t$ are complementary parts of $\partial\Omega$, that is

$$\partial\Omega_v \cup \partial\Omega_t = \partial\Omega, \tag{3.57}$$

$$\partial\Omega_v \cap \partial\Omega_t = \emptyset. \tag{3.58}$$

3.7 Governing equations

3.7.1 Solid model

The set of governing equations for the solid body B is given by

$$\operatorname{div} \boldsymbol{\sigma} + \boldsymbol{f} = \rho\dot{\boldsymbol{v}}, \tag{3.59}$$

$$\boldsymbol{\sigma} = J^{-1}\,\frac{\partial\Psi(\boldsymbol{F})}{\partial\boldsymbol{F}}\,\boldsymbol{F}^T - p\,\boldsymbol{I}, \tag{3.60}$$

$$J - 1 = 0, \tag{3.61}$$

along with the boundary conditions as stated in Sec. 3.6.1.

3.7.2 Fluid model

The set of governing equations for the fluid control volume $\varOmega$ is given by

$$\operatorname{div} \boldsymbol{\sigma} + \boldsymbol{f} = \rho \dot{\boldsymbol{v}}, \tag{3.62}$$

$$\boldsymbol{\sigma} = 2\mu \boldsymbol{d} - p\boldsymbol{I}, \tag{3.63}$$

$$\operatorname{div} \boldsymbol{v} = 0, \tag{3.64}$$

along with the boundary conditions as stated in Sec. 3.6.2.

Chapter 4

Numerical methods

In numerical modelling the governing equations of continuous media are discretised and linearised to form a set of algebraic equations that may be solved approximately using various algorithms and solution techniques. To simulate the FSI of a fistula, a structural model of the artery and vein needs to be coupled with a fluid model of the blood flow. In industry and research, the finite element method (FEM) is primarily used for structural modelling while the finite volume method (FVM) is often preferred for fluid modelling. Coupling these two methods is a frequent approach to FSI modelling and the one used in this project.

The ANSYS Academic Research suite is used to simulate the entire FSI system. The ANSYS® Workbench™ software's Coupling System component is used to couple ANSYS® Mechanical™ software, FEM code, with ANSYS® Fluent® software, the FVM solver, in a semi-implicit staggered manner. This chapter includes an overview of the FEM, the FVM, and the partitioned FSI approach used in this project.

4.1 The finite element method

The finite element method was originally used in modelling structural behaviour, but finite elements are now also used to analyse problems of heat transfer, fluid flow, and magnetic fields, to name a few [87]. The FEM, in general, models a body or region as an assembly of small elements where the approximate solution is a polynomial on elements and piecewise-continuous across elements.

This section gives a brief description of the finite element method. More details may be found for example in [88]. For a description of the approach used in this project please refer to the Mechanical APDL Guide and the ANSYS Mechanical User's Guide [89, 90].

4.1.1 The weak form

The weak form of the equation of motion is required in order to construct the finite element formulation. This is derived by multiplying the equation of motion by a test function $\delta\boldsymbol{v}$ and then integrating over the body. The test function satisfies the homogeneous essential boundary condition. In the absence of body forces this gives

$$\int\limits_B (\mathrm{div}\ \boldsymbol{\sigma}(\boldsymbol{u}, p) - \rho\,\ddot{\boldsymbol{u}}) \cdot \delta\boldsymbol{v}\ \mathrm{d}v = 0. \tag{4.1}$$

By applying Green's theorem we get

$$\int\limits_B \rho\,\ddot{\boldsymbol{u}}\,\delta\boldsymbol{v}\ \mathrm{d}v + \int\limits_B \boldsymbol{\sigma}\colon \mathrm{grad}\ \delta\boldsymbol{v}\ \mathrm{d}v - \int\limits_{\partial B} \big(\boldsymbol{\sigma}\boldsymbol{n}\big) \cdot \delta\boldsymbol{v}\ \mathrm{d}a = 0. \tag{4.2}$$

Setting $\boldsymbol{\sigma} = \boldsymbol{\sigma}' - p\,\boldsymbol{I}$ as in equation (3.45) and simplifying gives

$$\int\limits_B \big(\rho\,\ddot{\boldsymbol{u}} \cdot \delta\boldsymbol{v} + \boldsymbol{\sigma}'\colon \delta\boldsymbol{d} + p\,\mathrm{div}\ \delta\boldsymbol{v}\big)\ \mathrm{d}v - \int\limits_{\partial B_t} \bar{\boldsymbol{t}} \cdot \delta\boldsymbol{v}\ \mathrm{d}a = 0, \tag{4.3}$$

where $\delta\boldsymbol{d}$ is the variational rate of deformation. The weak form of the incompressibility constraint equation is derived similarly but with respect to a virtual pressure function δp giving

$$\int\limits_B \big(J - 1\big)\delta p\ \mathrm{d}v = 0. \tag{4.4}$$

4.1.2 Linearisation

The set of equations are nonlinear in $\boldsymbol{u}$ and so need to be linearised so that they can then to be solved with an iterative path-finding technique such as the Newton-Raphson method. Taylor expansion of a function of two variables $R(\boldsymbol{u}, p)$, neglecting terms of higher order than linear, gives

$$R^{k+1}(\boldsymbol{u},p) = R^k(\boldsymbol{u},p) - \left.\frac{\partial R}{\partial \boldsymbol{u}}\right|^k \Delta\boldsymbol{u} + \left.\frac{\partial R}{\partial p}\right|^k \Delta p = 0. \tag{4.5}$$

Linearisation of equation (4.3) gives

$$\int\limits_B \Big(\rho\, \ddot{\boldsymbol{u}} \cdot \delta\boldsymbol{v} + \delta\boldsymbol{d} \colon \mathbb{c} \colon \Delta\boldsymbol{\varepsilon} + \boldsymbol{\sigma} \colon \big((\text{grad } \delta\boldsymbol{v})^T \text{grad } \Delta\boldsymbol{u}\big) + \Delta p \,\text{div } \delta\boldsymbol{v}\Big) \text{ d}v = \\ -\int\limits_B \Big(\boldsymbol{\sigma}' \colon \delta\boldsymbol{d} + p\,\text{div } \delta\boldsymbol{v}\Big) \text{ d}v + \int\limits_{\partial B_t} \bar{\boldsymbol{t}} \cdot \delta\boldsymbol{v} \text{ d}a, \tag{4.6}$$

where $\mathbb{c}$ is the elasticity tensor in the spacial description. The linearisation of the incompressible constraint equation in the direction of increment Δp gives

$$\int\limits_\Omega \text{div } \Delta\boldsymbol{u}\, \delta p \text{ d}v = -\int\limits_B \big(J-1\big)\delta p \text{ d}v. \tag{4.7}$$

4.1.3 Discretisation

The domain B is subdivided into a set of n_{el} elements $E_1, E_2, \cdots, E_{n_{el}}$ that approximates the domain such that $E_1 \cup E_2 \cup \cdots \cup E_N \approx B$ and $E_i \cap E_j = \emptyset$ for $i \neq j$. An approximate solution $\boldsymbol{u}^h$ is chosen from the set of admissible finite element trial solutions. These functions must satisfy at least C^0 continuity and the essential boundary condition $\mathbf{u} = \overline{\mathbf{u}}$ on ∂B_u. This is stated formally as $\mathbf{u}^h(\mathbf{X}, t) \in \mathcal{S}_h$ where

$$\mathcal{S}_h = \{\mathbf{u} \mid \mathbf{u} \in C^0(\mathbf{X}), \quad \mathbf{u} = \overline{\mathbf{u}} \text{ on } \partial B_u\}. \tag{4.8}$$

The approximate solution is then given by

$$\boldsymbol{u}^h = \sum_{a=1}^{n} N_a(\mathbf{X})\, \boldsymbol{u}_a \tag{4.9}$$

where $N_a(\mathbf{X})$ are the chosen shape functions and $\boldsymbol{u}_a$ the nodal (displacement) degrees of freedom and n the number of nodes.

In the Galerkin finite element method the test functions $\delta\boldsymbol{v}^h$ are chosen from the same space as the trial functions with the additional restriction that these functions are zero at points on the boundary where essential boundary conditions are applied. Stated formally, $\delta \boldsymbol{v}^h(\mathbf{X}) \in \mathcal{S}_t$ where

$$\mathcal{S}_t = \{\delta \boldsymbol{v} \mid \delta \boldsymbol{v} \in C^0(\mathbf{X}), \quad \delta \boldsymbol{v} = \mathbf{0} \text{ on } \partial B_u\}. \tag{4.10}$$

The test functions chosen have the same form as the trial function, i.e.,

$$\delta \boldsymbol{v}^h = \sum_{a=1}^{n} N_a(\mathbf{X})\, \delta \boldsymbol{v}_a. \tag{4.11}$$

Voigt notation

Tensors can then be written in vector form to assist in calculation. The stress vector $\underline{\boldsymbol{\sigma}}$ is defined as

$$\underline{\boldsymbol{\sigma}} = [\sigma_{11}, \sigma_{22}, \sigma_{33}, \sigma_{23}, \sigma_{13}, \sigma_{12}]^T. \tag{4.12}$$

Similarly the rate of deformation tensor can be re-written as

$$\underline{\boldsymbol{d}} = [d_{11}, d_{22}, d_{33}, 2d_{23}, 2d_{13}, 2d_{12}]^T. \tag{4.13}$$

This choice of $\underline{\boldsymbol{d}}$ ensures that internal energy is calculated correctly as in

$$\int_B \boldsymbol{\sigma} : \boldsymbol{d}\ \mathrm{d}v = \int_B \underline{\boldsymbol{d}}^T \underline{\boldsymbol{\sigma}}\ \mathrm{d}v. \tag{4.14}$$

In vector notation equation (4.9) may be written as

$$\boldsymbol{u}^h = \underline{\boldsymbol{N}}\, \underline{\boldsymbol{u}} \tag{4.15}$$

where $\underline{\boldsymbol{N}}$ and $\underline{\boldsymbol{u}}$ are the shape function matrix and nodal displacement vector respectively. The quantities $\boldsymbol{x}$, $\boldsymbol{v}$, $\boldsymbol{a}$, $\boldsymbol{X}$,and $\delta \boldsymbol{v}$ are then approximated by the same shape functions along with their respective nodal vectors.

We will also need

$$\text{div } \boldsymbol{u}^h = \begin{bmatrix} \dfrac{\partial N_1}{\partial x} & \dfrac{\partial N_1}{\partial y} & \dots & \dfrac{\partial N_n}{\partial x} & \dfrac{\partial N_n}{\partial y} \end{bmatrix} \underline{\boldsymbol{u}} = \underline{\boldsymbol{L}}\, \underline{\boldsymbol{u}}, \tag{4.16}$$

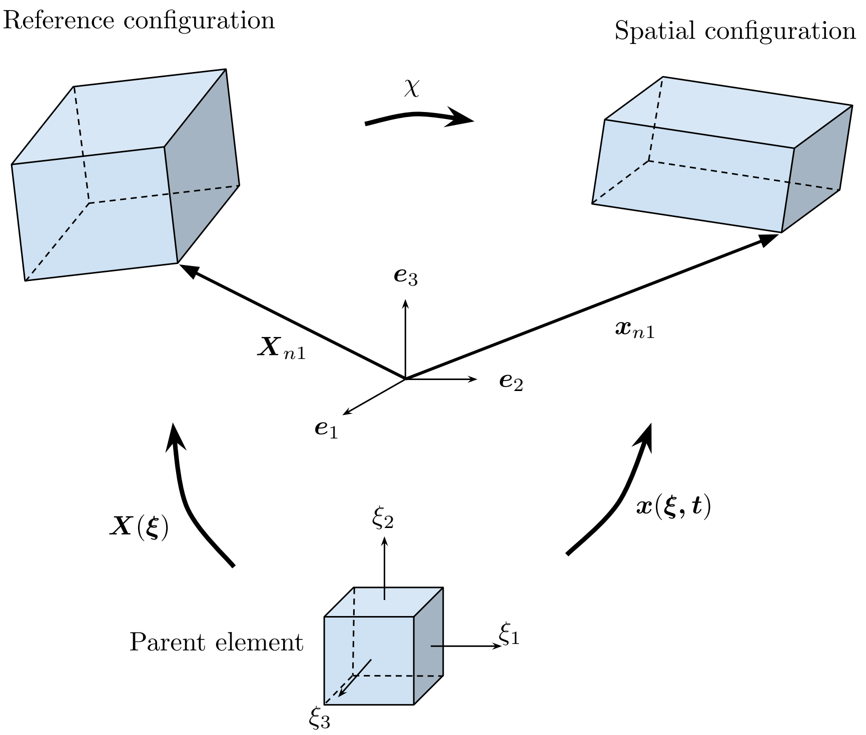

Figure 4.1: Mapping between elements in the reference and spacial configurations and the parent element configuration

with the quantities $\delta \boldsymbol{u}$, $\Delta \boldsymbol{u}$ approximated in the same way. The pressure is interpolated over internal pressure degrees of freedom $\underline{\boldsymbol{p}}$ according to

$$p^h = \sum_{a=1}^{n_p} \tilde{N}_a \, p_a = \underline{\tilde{\boldsymbol{N}}} \, \underline{\boldsymbol{p}}, \tag{4.17}$$

where n_p is the number of pressure degrees of freedom.

Parent element shape functions and mapping

The element shape functions are defined with respect to a parent element in a coordinate system with directions ξ_1, ξ_2, and ξ_3. Functions and their derivatives can then be mapped to the reference or current configurations as illustrated in Figure 4.1.

The shape functions derivatives are calculated from

$$\frac{\partial N_a(\boldsymbol{\xi})}{\partial \boldsymbol{x}} = \left(\frac{\partial \boldsymbol{x}}{\partial \boldsymbol{\xi}}\right)^{-T} \frac{\partial N_a}{\partial \boldsymbol{\xi}}. \tag{4.18}$$

Shape function derivatives with respect to $\boldsymbol{X}$ are required for the deformation gradient and left Cauchy-Green stretch tensor and are given by

$$\frac{\partial N_a(\boldsymbol{\xi})}{\partial \boldsymbol{X}} = \left(\frac{\partial \boldsymbol{X}}{\partial \boldsymbol{\xi}}\right)^{-T} \frac{\partial N_a}{\partial \boldsymbol{\xi}}. \tag{4.19}$$

Enhanced assumed strain method

So far we have described only the formulation of the mixed displacement-pressure method for incompressible problems. However, in bending dominated problems volumetric locking may still occur. Locking, in general, can be prevented by employing the enhanced strain formulation where a number of internal degrees of freedom are introduced at the element level and condensed out. We follow the treatment by Nagtegaal & Fox [91] which is based on the work of Simo & Armero [92] and Simo, Armero & Taylor [93]. The deformation gradient approximation is adjusted by the addition of an independent field so that the total deformation gradient is given by

$$\boldsymbol{F}^h = \text{Grad}\ \boldsymbol{\varphi}^h + \tilde{\boldsymbol{F}}^h, \tag{4.20}$$

where Grad $\boldsymbol{\varphi}^h$ is the compatible displacement-based part and $\tilde{\boldsymbol{F}}^h$ is the enhanced field which satisfy

$$\int_{B_0^e} \boldsymbol{P}^h : \tilde{\boldsymbol{F}}^h \ \mathrm{d}V = 0 \tag{4.21}$$

for all $\tilde{\boldsymbol{F}}^h$, where B_0^e is the reference element volume and $\boldsymbol{P}^h$ is the approximation to the Piola-Kirchhoff stress. The incremental enhanced deformation gradient field is constructed at an element level with independent internal degrees of freedom $\Delta\boldsymbol{\alpha}$ according to

$$\Delta\tilde{\boldsymbol{F}}^h = \sum_i \Delta\boldsymbol{\alpha}\, \frac{j(\mathbf{0})}{j(\boldsymbol{\xi})}, \left[\boldsymbol{J}(\mathbf{0})\right]^{-1} \boldsymbol{\xi}_i \tag{4.22}$$

where

$$j(\boldsymbol{\xi}) = \det\big(\boldsymbol{J}(\boldsymbol{\xi})\big) \quad \text{and} \quad \boldsymbol{J}(\boldsymbol{\xi}) = \frac{\mathrm{d}\boldsymbol{x}}{\mathrm{d}\boldsymbol{\xi}}, \tag{4.23}$$

while $j(\mathbf{0})$ and $\boldsymbol{J}(\mathbf{0})$ are the evaluations at the centre of the isoparametric coordinate system. The vectors $\boldsymbol{\xi}_i$ are those in each of the principal directions of the parent element.

The Almansi strain is obtained directly from the deformation gradient using

$$\boldsymbol{\varepsilon}^h = \boldsymbol{\varepsilon}^h_u + \boldsymbol{\varepsilon}^h_\alpha = \frac{1}{2}\Big(\boldsymbol{I} - \big(\boldsymbol{F}^h\big)^{-T}\big(\boldsymbol{F}^h\big)^{-1}\Big), \tag{4.24}$$

with the conformal part approximated by

$$\boldsymbol{\varepsilon}^h_u = \frac{1}{2}\sum_a^n \left(\boldsymbol{u}_a \otimes \frac{\partial N_a}{\partial \boldsymbol{x}} + \frac{\partial N_a}{\partial \boldsymbol{x}} \otimes \boldsymbol{v}_a\right) = \underline{\boldsymbol{B}}_u\, \underline{\boldsymbol{u}}, \tag{4.25}$$

and enhanced part given in vector notation by

$$\boldsymbol{\varepsilon}^h_\alpha = \frac{j(\mathbf{0})}{j(\boldsymbol{\xi})}\big[\boldsymbol{J}(\mathbf{0})\big]^{-1}\, \underline{\boldsymbol{M}}\, \underline{\boldsymbol{\alpha}} = \underline{\boldsymbol{B}}_\alpha\, \underline{\boldsymbol{\alpha}}, \tag{4.26}$$

where $\underline{\boldsymbol{M}}$ denotes the interpolation matrix defined in [94]. The quantities $\boldsymbol{d}$, $\delta\boldsymbol{d}$, and $\Delta\boldsymbol{\epsilon}$ are approximated in the same way.

The approximation of the conforming part of the deformation gradient is given by

$$\text{Grad}\ \boldsymbol{\varphi}^h = \sum_{A=1}^n \boldsymbol{x}^A \otimes \frac{\partial N_a}{\partial \boldsymbol{X}}. \tag{4.27}$$

Gaussian quadrature

Integration is carried over the parent element

$$\int_\Omega f(\mathbf{x})\ \mathrm{dv} = \int_{\Omega_0} \hat{f}(\mathbf{X})\ J\ \mathrm{dV}_0 = \int_{\Omega_\xi} \tilde{f}(\boldsymbol{\xi})\ J_\xi\ \mathrm{d}V_\xi \tag{4.28}$$

where J_ξ maps the volume between the parent element and current configuration element

$$J_\xi = \det\left(\frac{\partial \boldsymbol{x}}{\partial \boldsymbol{\xi}}\right). \tag{4.29}$$

The integration is carried out by Gaussian quadrature according to

$$\int_{\Omega_\xi} f(\boldsymbol{\xi})\ \mathrm{d}V_\xi = \int_{-1}^{1}\int_{-1}^{1}\int_{-1}^{1} f(\boldsymbol{\xi})\ \mathrm{d}\xi_1\ \mathrm{d}\xi_2\ \mathrm{d}\xi_3 = \sum_{i=1}^{n_{gp}}\sum_{j=1}^{n_{gp}}\sum_{k=1}^{n_{gp}} w_{(i)}\ w_{(j)}\ w_{(k)}\ f(\boldsymbol{\xi}_{(ijk)}) \tag{4.30}$$

where n_{gp} is the number of Gauss points chosen; $\boldsymbol{\xi}_{(ijk)}$ is the position of the particular Gauss point and; $w_{(i)}$, $w_{(j)}$, and $w_{(k)}$ are the weights associated with the Gauss point.

The finite element matrices

Applying the approximations to equation (4.6) and (4.7) and dropping the arbitrary weighting functions yields a set of matrix equations given by

$$\begin{bmatrix} \underline{\boldsymbol{M}}\,\ddot{\underline{\boldsymbol{u}}} \\ \boldsymbol{0} \\ \boldsymbol{0} \end{bmatrix} + \begin{bmatrix} \underline{\boldsymbol{K}}_{uu} & \underline{\boldsymbol{K}}_{u\alpha} & \underline{\boldsymbol{K}}_{up} \\ \underline{\boldsymbol{K}}_{\alpha u} & \underline{\boldsymbol{K}}_{\alpha\alpha} & \boldsymbol{0} \\ \underline{\boldsymbol{K}}_{pu} & \boldsymbol{0} & \boldsymbol{0} \end{bmatrix} \begin{bmatrix} \underline{\Delta\boldsymbol{u}} \\ \underline{\Delta\boldsymbol{\alpha}} \\ \underline{\Delta p} \end{bmatrix} = \begin{bmatrix} \underline{\boldsymbol{F}}_{\mathrm{ext}} \\ \boldsymbol{0} \\ \boldsymbol{0} \end{bmatrix} - \begin{bmatrix} \underline{\boldsymbol{R}}_u \\ \underline{\boldsymbol{R}}_\alpha \\ \underline{\boldsymbol{R}}_{\mathrm{p}} \end{bmatrix} \tag{4.31}$$

where $\underline{\boldsymbol{M}}$ is the mass matrix which is derived from the integral

$$\underline{\boldsymbol{M}} = \int\limits_B \rho \underline{\boldsymbol{N}}^T \underline{\boldsymbol{N}}\ \mathrm{d}v. \tag{4.32}$$

The matrix $\underline{\boldsymbol{K}}_{uu}$ is formed from equation

$$\underline{\boldsymbol{K}}_{uu} = \int\limits_B \underline{\boldsymbol{B}}_u^T\,\underline{\boldsymbol{D}}\,\underline{\boldsymbol{B}}_u\ \mathrm{d}v + \boldsymbol{I}\,\underline{\boldsymbol{L}}\,\underline{\boldsymbol{\tau}}\,\underline{\boldsymbol{L}}^T\ \mathrm{d}v \tag{4.33}$$

where the matrices $\underline{\boldsymbol{D}}$ and $\underline{\boldsymbol{\tau}}$ correspond to the terms $\mathbb{c}$ and $\boldsymbol{\sigma}$ in equation (4.6). The matrices $\underline{\boldsymbol{K}}_{up}$, $\underline{\boldsymbol{K}}_{u\alpha}$, and $\underline{\boldsymbol{K}}_{\alpha u}$ are derived similarly from the current volume integrals of $\underline{\boldsymbol{L}}^T\,\underline{\tilde{\boldsymbol{N}}}$, $\underline{\boldsymbol{B}}_u^T\,\underline{\boldsymbol{D}}\,\underline{\boldsymbol{B}}_\alpha$, and $\underline{\boldsymbol{B}}_\alpha^T\,\underline{\boldsymbol{D}}\,\underline{\boldsymbol{B}}_\alpha$ respectively with $\underline{\boldsymbol{K}}_{u\alpha} = \underline{\boldsymbol{K}}_{\alpha u}^T$ and $\underline{\boldsymbol{K}}_{pu} = \underline{\boldsymbol{K}}_{up}^T$.

$\underline{\boldsymbol{R}}_u$ is derived according to

$$\underline{\boldsymbol{R}}_u = \int\limits_B \underline{\boldsymbol{B}}_u^T \, \underline{\boldsymbol{\sigma}}' \, \mathrm{d}v - \int\limits_B \underline{\boldsymbol{L}}^T \, \underline{\boldsymbol{p}} \, \mathrm{d}v \tag{4.34}$$

and $\underline{\boldsymbol{R}}_\alpha$ is derived similarly from $\boldsymbol{B}_\alpha^T \, \underline{\boldsymbol{\sigma}}$. The external force vector $\underline{\boldsymbol{F}}_{\mathrm{ext}}$ is given by

$$\underline{\boldsymbol{F}}_{\mathrm{ext}} = \int\limits_{\partial B} \underline{\boldsymbol{N}}^T \, \underline{\bar{\boldsymbol{t}}} \, \mathrm{d}a. \tag{4.35}$$

Applying the finite element approximations to the linearised constraint equation (4.7) we get

$$\underline{\boldsymbol{R}}_{\mathrm{p}} = \underline{\tilde{\boldsymbol{N}}} \, (J - 1). \tag{4.36}$$

At the element level $\underline{\Delta\boldsymbol{\alpha}}$ can be condensed out of equation (4.31) by noting that

$$\underline{\Delta\boldsymbol{\alpha}} = -\underline{\boldsymbol{K}}_{\alpha\alpha}^{-1} \left[\underline{\boldsymbol{K}}_{\alpha u} \, \underline{\Delta\boldsymbol{u}} + \underline{\boldsymbol{R}}_\alpha \right]. \tag{4.37}$$

Equation (4.31) can then be reduced to

$$\begin{bmatrix} \underline{\boldsymbol{M}\ddot{\boldsymbol{u}}} \\ \boldsymbol{0} \end{bmatrix} + \begin{bmatrix} \underline{\boldsymbol{K}}_{\mathrm{eff}} & \underline{\boldsymbol{K}}_{up} \\ \underline{\boldsymbol{K}}_{pu} & \boldsymbol{0} \end{bmatrix} \begin{bmatrix} \underline{\Delta\boldsymbol{u}} \\ \underline{\Delta p} \end{bmatrix} = \begin{bmatrix} \underline{\boldsymbol{F}}_{\mathrm{ext}} \\ \boldsymbol{0} \end{bmatrix} - \begin{bmatrix} \underline{\boldsymbol{R}}_{\mathrm{eff}} \\ \underline{\boldsymbol{R}}_{\mathrm{p}} \end{bmatrix} \tag{4.38}$$

where $\underline{\boldsymbol{K}}_{\mathrm{eff}} = \underline{\boldsymbol{K}}_{uu} - \underline{\boldsymbol{K}}_{u\alpha} \, \underline{\boldsymbol{K}}_{\alpha\alpha}^{-1} \, \underline{\boldsymbol{K}}_{\alpha u}$ and $\underline{\boldsymbol{R}}_{\mathrm{eff}} = \underline{\boldsymbol{R}}_u - \underline{\boldsymbol{K}}_{u\alpha} \, \underline{\boldsymbol{K}}_{\alpha\alpha}^{-1} \, \underline{\boldsymbol{R}}_\alpha$.

Time discretisation

So far we have not dealt with the acceleration term $\underline{\ddot{\boldsymbol{u}}}$. For an implicit time integration scheme the equilibrium equation at time $t + \Delta t$ is solved to obtain a solution for time $t + \Delta t$. For implicit time integration and a full Newton-Raphson scheme equation (4.38) can be recast as

$$\boldsymbol{M} \, \ddot{\boldsymbol{u}}_k^{(t+\Delta t)} + \boldsymbol{K} \, \Delta\boldsymbol{u}_k^{(t+\Delta t)} = \boldsymbol{R}_{k-1}^{(t+\Delta t)} + \boldsymbol{F}_k^{(t+\Delta t)} \tag{4.39}$$

where k is the current Newton iteration and $k-1$ the previous Newton iteration. The implicit time stepping scheme then updates the displacement vector according to

$$\boldsymbol{u}_k^{t+\Delta t} = \boldsymbol{u}_{k-1}^{t+\Delta t} + \Delta \boldsymbol{u}_{k-1}. \tag{4.40}$$

The Newmark method [95] uses finite difference expansions of Δt and for the trapezoidal rule assumes that the displacement vector and velocity vector at time $t+\Delta t$ are respectively given by

$$\boldsymbol{u}^{t+\Delta t} = \boldsymbol{u}^t + \frac{\Delta t}{2}\Big(\dot{\boldsymbol{u}}^t + \dot{\boldsymbol{u}}^{t+\Delta t}\Big) \quad \text{and} \quad \dot{\boldsymbol{u}}^{t+\Delta t} = \dot{\boldsymbol{u}}^t + \frac{\Delta t}{2}\Big(\ddot{\boldsymbol{u}}^t + \ddot{\boldsymbol{u}}^{t+\Delta t}\Big). \tag{4.41}$$

The acceleration vector at time $t+\Delta t$ is then found to be given by

$$\ddot{\boldsymbol{u}}^{t+\Delta t} = \frac{4}{\Delta t^2}\Big(\boldsymbol{u}^{t+\Delta t} - \boldsymbol{u}^t\Big) + \frac{4}{\Delta t}\dot{\boldsymbol{u}}^t - \ddot{\boldsymbol{u}}^t. \tag{4.42}$$

Substituting equation (4.40) into (4.42) and applying the result to the equilibrium equation (4.39) so that we can solve for $\Delta \boldsymbol{u}_k$ from known quantities according to

$$\left[\boldsymbol{K} + \frac{4}{\Delta t^2}\boldsymbol{M}\right]\Delta \boldsymbol{u}_k = \boldsymbol{F}_k^{t+\Delta t} - \boldsymbol{R}_{k-1}^{t+\Delta t} - \boldsymbol{M}\left[\frac{4}{\Delta t^2}\Big(\boldsymbol{u}_{k-1}^{t+\Delta t} - \boldsymbol{u}^t\Big) - \frac{4}{\Delta t}\dot{\boldsymbol{u}}^t - \ddot{\boldsymbol{u}}^t\right]. \tag{4.43}$$

4.1.4 The Newton-Raphson solution procedure

To find the current position $\boldsymbol{x}$ at each time-step an iterative procedure is followed where $\boldsymbol{u}^{t+\Delta t}$ is obtained by repeatedly solving for $\Delta \boldsymbol{u}_k$ by equation (4.43) and updating $\boldsymbol{u}_k^{t+\Delta t}$ according to equation (4.40) until certain convergence criteria are met . This is the Newton-Raphson procedure, which is summarised below:

1. Initialise for t_n
    (a) If $t_n = 0$: $\boldsymbol{F} = \boldsymbol{I}$, $\boldsymbol{x}_0 = \boldsymbol{X}_0$, $\boldsymbol{R} = \boldsymbol{0}$, $\boldsymbol{u}_n = \boldsymbol{v}_n = \boldsymbol{0}$
    (b) If $t_n \neq 0$: $\boldsymbol{X}_n = \boldsymbol{x}_n$, $\boldsymbol{R} = \boldsymbol{0}$
2. find $\Delta \boldsymbol{F}_n$
3. set $\boldsymbol{F}_n = \boldsymbol{F}_n + \Delta \boldsymbol{F}_n$
4. set $\boldsymbol{R} = \boldsymbol{R} - \Delta \boldsymbol{F}_n$

   (a) find $\boldsymbol{K}$
   (b) solve $\boldsymbol{K}\Delta\boldsymbol{u} = -\Delta\boldsymbol{R}$
   (c) set $\boldsymbol{x} = \boldsymbol{x} + \Delta\boldsymbol{u}$
   (d) update $\boldsymbol{R}$
   (e) do (i)-(iv) while $\|\boldsymbol{R}\|/||\boldsymbol{F}_n|| >$ tol

5. loop over (2)-(4) for all load increments $\Delta\boldsymbol{F}_n$
6. find $\boldsymbol{u}^{t+\Delta t}$
7. set $n = n + 1$, $t_n = t_n + \Delta t$
8. set $\Delta\boldsymbol{F}_n$
9. loop over (1)-(8) for all time steps Δt

The direct sparse matrix solver

The system of simultaneous linear equations can be solved by a direct elimination process or an iterative method. The method used in this project is the direct method by an elimination approach which solves the unknown vector in equation (4.43),

$$\boldsymbol{K}\,\boldsymbol{x} = \boldsymbol{F} \tag{4.44}$$

The direct solver uses triangular decomposition with forward and backward substitution to solve for $\underline{\Delta\boldsymbol{x}}$. A direct sparse solving algorithm can optimise the solution procedure as the matrices generated by the finite element procedure are normally sparse. The sparse matrix solver is designed to consider only the non-zero entries in $\boldsymbol{K}$ and can thus be further optimised by reordering the $\boldsymbol{K}$ matrix and respective $\underline{\Delta\boldsymbol{x}}$ and $\underline{\boldsymbol{F}}$ vectors. This reordering minimises the number of non-zero entries that appear in the lower triangular matrix from Cholesky decomposition. The decomposition takes the form

$$\boldsymbol{L}\,\boldsymbol{U}\,\boldsymbol{x} = \boldsymbol{F} \tag{4.45}$$

where $\boldsymbol{L}$ and $\boldsymbol{U}$ are the lower and upper triangular matrices respectively.

4.2 The finite volume method

The finite volume method (FVM) is a numerical method with a formulation that lends itself well to computational fluid dynamics (CFD). The FVM has a long history in CFD, leading to it generally being the preferred method in fluid flow modelling. Many improvements to algorithms, new acceleration techniques and understanding of numerical behaviour in the FVM have led to robust and efficient CFD codes.

The finite volume method takes the conservative form of the transport equations, which are discretised over a region of control volumes to form a set of coupled equations. The coupled equations may be solved by a number of methods.

This section aims to introduce FV CFD modelling specifically related to the implementation used in this project. The various discretisation techniques and the PISO pressure-velocity coupling algorithm used are described. For more detailed descriptions and derivations the reader is referred to [96]. For a description of the approach used in this project please refer to the Fluent Theory Guide and the Fluent User's Guide [97, 98].

4.2.1 Divergence form of the momentum equation

Equation 3.30 can be rewritten as

$$\rho\,\dot{\boldsymbol{v}} = \frac{\partial}{\partial t}(\rho\,\boldsymbol{v}) + \mathrm{div}\ (\rho\,\boldsymbol{v}\cdot\boldsymbol{v}), \tag{4.46}$$

and introduced into the momentum equation for a Newtonian fluid yields the divergence form of the momentum equation

$$\frac{\partial}{\partial t}(\rho\,\boldsymbol{v}) + \mathrm{div}\ (\rho\,\boldsymbol{v}\cdot\boldsymbol{v}) = \mathrm{div}\ (2\,\mu\,\boldsymbol{d}) - \mathrm{div}\ (p\,\boldsymbol{I}) + \boldsymbol{f}. \tag{4.47}$$

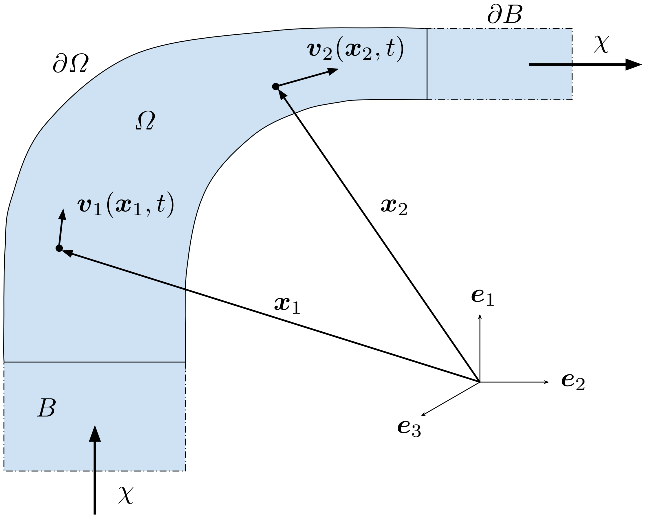

Figure 4.2: A fluid body moving through a fixed control volume.

4.2.2 Control volume integration

Integrating equation (4.47) over an arbitrary control volume Ω_a in the absence of body forces gives

$$\int_{\Omega_a} \frac{\partial}{\partial t}(\rho \boldsymbol{v})\ \mathrm{d}v + \int_{\Omega_a} \mathrm{div}\ (\rho \boldsymbol{v} \cdot \boldsymbol{v})\ \mathrm{d}v = \int_{\Omega_a} \mathrm{div}\ (2\mu \boldsymbol{d})\ \mathrm{d}v - \int_{\Omega_a} \mathrm{div}\ (p\boldsymbol{I})\ \mathrm{d}v. \quad (4.48)$$

Application of Gauss' theorem gives

$$\int_{\Omega_a} \frac{\partial}{\partial t}(\rho\, \boldsymbol{v})\ \mathrm{d}v + \int_{\partial\Omega_a} \rho\, \boldsymbol{v}(\boldsymbol{v} \cdot \boldsymbol{n})\ \mathrm{d}a = \int_{\partial\Omega_a} 2\,\mu\, \boldsymbol{d}\boldsymbol{n}\ \mathrm{d}a - \int_{\partial\Omega_a} p\,\boldsymbol{n}\ \mathrm{d}a. \quad (4.49)$$

where $\partial\Omega_a$ is the boundary of the control volume.

The split momentum equations

In component form, equation (4.49) can be written as

$$\int_{\Omega_a} \frac{\partial\,(\rho\,\phi)}{\partial t}\ \mathrm{d}v + \int_{\partial\Omega_a} \rho\,\phi(\boldsymbol{v} \cdot \boldsymbol{n})\ \mathrm{d}a = \int_{\partial\Omega_a} \mu\, \mathrm{grad}\ \ \cdot \phi\, \boldsymbol{n}\ \mathrm{d}a - \int_{\partial\Omega_a} p\, \boldsymbol{n} \cdot \boldsymbol{e}_\phi\ \mathrm{d}a \quad (4.50)$$

where ϕ is equal to u, v or w, the velocity components in the x, y and z directions. In time-dependent problems it is also necessary to integrate with respect to a change in time, giving

$$\int_{\Delta t}\int_{\Omega_a} \frac{\partial\,(\rho\,\phi)}{\partial t}\ \mathrm{d}v\ \mathrm{d}t + \int_{\Delta t}\int_{\partial\Omega_a} \rho\,\phi(\boldsymbol{v}\cdot\boldsymbol{n})\ \mathrm{d}a\ \mathrm{d}t = \int_{\Delta t}\int_{\partial\Omega_a} \mu\,\mathrm{grad}\ \cdot\phi\,\boldsymbol{n}\ \mathrm{d}a\ \mathrm{d}t - \int_{\Delta t}\int_{\partial\Omega_a} p\,\boldsymbol{n}\cdot\boldsymbol{e}_\phi\ \mathrm{d}a\ \mathrm{d}t. \tag{4.51}$$

The continuity equation

In the FVM an alternate expression of the continuity equation is used, that is,

$$\frac{\partial\rho}{\partial t} + \mathrm{div}\ (\rho\,\boldsymbol{v}) = 0. \tag{4.52}$$

The density of an incompressible fluid remains constant so that the first term in the equation 4.52 so that we are left with

$$\mathrm{div}\ (\rho\,\boldsymbol{v}) = 0. \tag{4.53}$$

Integrating this over an arbitrary control volume and applying Gauss' theorem gives the following constraint on the mass flux through the boundary of the control volume:

$$\int_{\partial\Omega_a} \rho\boldsymbol{v}\cdot\boldsymbol{n}\ \mathrm{d}s = 0. \tag{4.54}$$

4.2.3 Discretisation schemes

The next step in developing the FVM is to discretise the integrated transport equations so that they apply to discrete solution storage points of the control volumes. In the FVM three-dimensional control volumes are made up of discrete planar faces that enclose a polygon: these are referred to as cells. ANSYS Fluent uses a cell-centred approach where the velocities and pressures are stored at the cell centres and face values are determined by interpolation of the stored values to the face centres.

The momentum equation (4.50), for each polygonal cell with faces f, is given by

$$\frac{\partial\,(\rho\phi)}{\partial t}\Delta V + \sum_f (\rho\phi_f\boldsymbol{v}_f\cdot\boldsymbol{A_f}) = \sum_f (\mu_f\nabla\phi_f\cdot\boldsymbol{A_f}) + \sum_f p_f\boldsymbol{A}_f\cdot\boldsymbol{e}_\phi \tag{4.55}$$

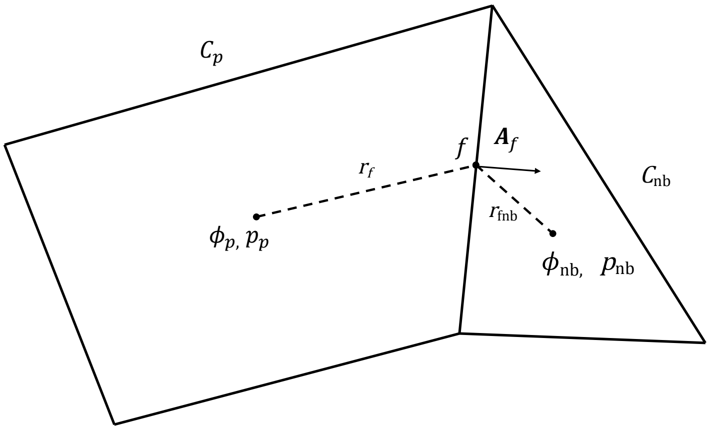

Figure 4.3: Illustration of the variables used in spatial and pressure discretisation between neighbouring cells

with the following discretisation schemes showing how the face values and gradients are obtained.

Second-order upwind spatial discretisation

In fluid flow ϕ is diffused and convected through the faces of each control volume. For various discretisation schemes ϕ is therefore required at each face of the cells. This quantity ϕ_f needs to be interpolated from ϕ at each of the neighbouring cells sharing that face.

A two-dimensional representation of two adjacent cells, used in the spatial and pressure discretisation, is shown in Figure 4.3. We denote C_p the discretised cell and by C_{nb} the neighbouring cell that shares face f where ϕ_f is required. The quantities $\boldsymbol{r}_f$ and $\boldsymbol{r}_{fnb}$ are the vectors from the cell centres of C_p and C_{nb} to the centre of their shared face respectively. The quantity $\boldsymbol{A}_f$ is the area vector (includes the normal and magnitude of the face area) of the shared face for the discretised cell.

An upwinding scheme is preferred in CFD , whereby ϕ_f is approximated by ϕ at the upstream control volume. By taking the flow direction into account in this way faster convergence is obtained, especially in convection dominated problems. The second-

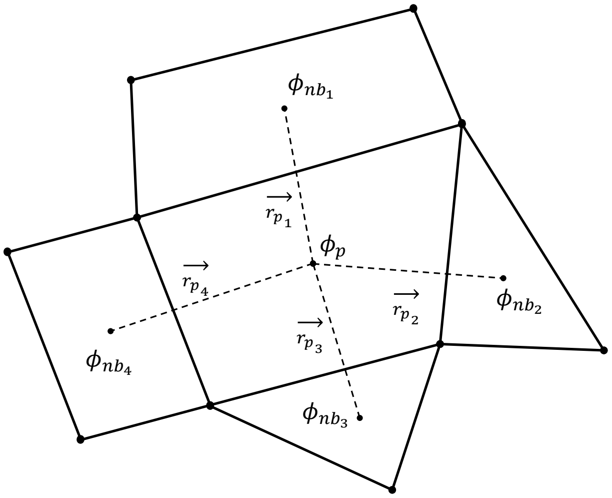

Figure 4.4: Discretisation variables used in calculating gradients illustrated on an unstructured grid

order upwinding scheme is computed using the expression

$$\phi_f = \phi_{up} + \text{grad}\ \phi_{up} \cdot \boldsymbol{r_f}, \tag{4.56}$$

where ϕ_{up} is the cell-centred ϕ upstream cell.

Least squares gradient reconstruction

Gradients of variables are required in the various schemes such as in second-order upwind discretisation. A number of methods for calculating gradients on structured or unstructured grids are used in the FVM. A popular method, due to its robustness and efficiency, is the least-squares gradient method. It gives good accuracy even on skewed and distorted meshes while remaining computationally efficient.

For a two-dimensional grid, as shown in Figure 4.4, a first-order Taylor expansion about ϕ_p gives

$$\phi_{np_i} = \phi_p + \left(\frac{\partial\phi}{\partial x}\right)\bigg|_p \Delta x_i + \left(\frac{\partial\phi}{\partial y}\right)\bigg|_p \Delta y_i. \tag{4.57}$$

This set of equations is assembled into the following matrix equation for a cell with n

sides:

$$\begin{bmatrix} \Delta x_1 & \Delta y_1 \\ \Delta x_2 & \Delta y_2 \\ \Delta x_3 & \Delta y_3 \\ \vdots & \vdots \\ \Delta x_n & \Delta y_n \end{bmatrix} \begin{bmatrix} \left.\dfrac{\partial \phi}{\partial x}\right|_p \\ \left.\dfrac{\partial \phi}{\partial y}\right|_p \end{bmatrix} = \begin{bmatrix} \phi_1 - \phi_p \\ \phi_2 - \phi_p \\ \phi_3 - \phi_p \\ \vdots \\ \phi_n - \phi_p \end{bmatrix} . \tag{4.58}$$

This results in an overdetermined system of linear equations, in the form $\boldsymbol{AX} = \boldsymbol{B}$, where $\boldsymbol{X}$ is obtained by the least-squares method. This method is easily adapted to the three-dimensional case.

Pressure discretisation and the co-located scheme

The coupling between velocity and pressure in an incompressible fluid can lead to an oscillatory pressure field that satisfies the momentum equation and yields a good approximation to the velocity field but is otherwise non-physical. It is convenient to use a co-located grid scheme, where the pressure and velocity are both stored at the cell centres, along with Rhie-Chow [99] interpolation of the pressure to overcome this numerical error.

The pressure term in the momentum equation is discretised with second-order accuracy according to

$$\sum_f p_f \boldsymbol{A}_f \cdot \boldsymbol{e}_i = \sum_f \left(\frac{1}{2}\left(p_p - p_{nb}\right) + \frac{1}{2}\left(\nabla p_p \cdot \boldsymbol{r}_{f_p} + \nabla p_{nb} \cdot \boldsymbol{r}_{f_{nb}}\right)\right) \boldsymbol{A}_f \cdot \boldsymbol{e}_i \tag{4.59}$$

where ∇p_p and ∇p_{nb} are determined from the least squares gradient reconstruction method.

Second-order implicit time discretisation and integration

Discretisation of the partial differential equations in time involves the integration of each term with respect to time. Second-order time implicit time discretisation yields

$$\left(\frac{\mathrm{d}\phi}{\mathrm{d}t}\right)^{t+\Delta t} = \frac{3\phi^{t+\Delta t} - 4\phi^{t} + \phi^{t-\Delta t}}{2\Delta t}. \tag{4.60}$$

4.2.4 Discretisation of the transport equations

The discretised form of the continuity equation takes the form

$$\sum_f J_f A_f = 0 \tag{4.61}$$

where J_f is the mass flux through face A_f. Rhie-Chow interpolation of the pressure gives a face flux calculation

$$J_f = p_f \frac{a_{p,c_0} v_{n,c_0} + a_{p,c_1} v_{p,c_1}}{a_{p,c_0} + a_{p,c_1}} + d_f \left[\left(p_{c_0} + (\Delta p)_{c_0} \cdot \boldsymbol{r}_{c_0}\right) - \left(p_{c_1} + (\Delta p)_{c_1} \cdot \boldsymbol{r}_{c_1}\right)\right]. \tag{4.62}$$

Applying the discretisation schemes to equation (4.55) yields a set of linearised momentum equations for each cell that can be put in the form

$$a_p \phi_p = \sum_{nb} a_{nb} \phi_{nb} + \sum_f p_f \boldsymbol{A}_f \cdot \boldsymbol{e}_\phi + b, \tag{4.63}$$

where a_p and a_{nb} are the linearised coefficients of ϕ_p and ϕ_{nb} respectively.

4.2.5 Pressure-velocity coupling and solving algorithms

Since the momentum and continuity equations are coupled through the velocity terms, and the convective term in each of the momentum equations introduces a non-linearity, an iterative solution strategy is used in pressure-based solvers to converge to the true solution. A segregated approach is often used in CFD where the coupled equations are corrected one after another giving a robust and efficient method.

The SIMPLE segregated algorithm of Patankar and Spalding (1972) or one of its derivatives can be used to progressively update the velocity and pressure fields. The PISO algorithm, a revision of the SIMPLE algorithm, that is more efficient in solving transient flow problems was used in this project. These segregated approaches are discussed in this section.

The SIMPLE algorithm

The SIMPLE (Semi-Implicit Method for Pressure Linked Equations) iteration process begins with a 'guessed' pressure and velocity field where p^*, u_0,v_0 and w_0 are initialised for each solution point of the domain. The first step is then to solve the discretised momentum equations sequentially to obtain an intermediate velocity field of u^*,v^* and w^* by an under-relaxed momentum equation given by

$$\phi_p^* = \frac{\alpha_u}{a_p}\Big(\sum_{nb} a_{nb}\phi_{nb}^* + \sum_f p_f \boldsymbol{A}_f \cdot \boldsymbol{e}_\phi + b\Big) + a_p \frac{1-\alpha_u}{\alpha_u}\phi_p^n, \tag{4.64}$$

where α_u is the velocity relaxation variable with $\alpha_u < 1$. The resulting face flux from the intermediate velocity field will not satisfy the discrete continuity equation, therefore a correction J_f' is added to the face flux J_f^* to give

$$J_f = J_f^* + J_f'. \tag{4.65}$$

A discrete pressure correction equation is then obtained by substituting the flux correction equation into the discrete continuity equation to give

$$a_p p' = \sum_{nb} a_{nb} p_{nb}' + \sum_f^{N_{faces}} J_f^* A_f. \tag{4.66}$$

Once the pressure correction equation is solved the cell pressure is updated by an under-relaxed pressure correction equation, given by

$$p^{**} = p^* + \alpha_p p', \tag{4.67}$$

where α_p is the pressure relaxation variable. The pressure correction equation is prone to divergence and is hence under-relaxed with $\alpha_p < 1$. The face flux is corrected by

$$J_f = J_f^* + \alpha_u \frac{A_f \cdot \boldsymbol{e}_{phi}}{a_f} \left(p'_{c_0} - p'_{c_1}\right). \tag{4.68}$$

The velocities then also need to be corrected according to

$$\phi = \phi^* + \phi', \tag{4.69}$$

where u is the 'true' velocity field while u' is velocity correction field which when substituted into the momentum equations gives

$$a_p \phi'_p = \sum_{nb} a_{nb} \phi'_{nb} + \sum_f p'_f A_f + b'. \tag{4.70}$$

Substitution of equation (4.69) into (4.70) gives the 'true' velocity field. However, in the SIMPLE algorithm the terms involving neighbouring velocity corrections are neglected, yielding the velocity correction equation

$$a_p \phi_p^{**} = a_p \phi_p^* + \sum_f p'_f A_f. \tag{4.71}$$

the corrected pressure p^{**} and velocity component solutions ϕ_p^{**} are checked for convergence at the end of the SIMPLE iteration (see Section 4.2.5). If the solution is not converged p^* and ϕ_p^* are set to equal to p^{**} and ϕ_p^{**} and the simple iteration is started again.

PISO algorithm modification

In the PISO algorithm a second pressure and velocity correction step is added to the end of the SIMPLE algorithm, before convergence is checked, so that the continuity and momentum equations are more closely satisfied at the end of each iteration. A second pressure correction equation, solved to find p'', is given by

$$a_p p'' = \sum_{nb} a_{nb} p''_{nb} + \sum_f^{N_{faces}} J_f^{**} A_f. \tag{4.72}$$

where J_f^{**} is the updated face flux after the initial pressure and velocity corrections. The pressures are then corrected a second time by

$$p^{***} = p^{**} + \alpha_p p'', \tag{4.73}$$

with the velocities finally corrected a second time by

$$a_p \phi_p^{***} = a_p \phi_p^{*} + \sum_f p'_f A_f + \sum_{nb} a_{nb} \left(\phi_{nb}^{**} - \phi_{nb}^{*} \right) + \sum_f p''_f A_f. \tag{4.74}$$

The PISO iteration ends exactly as the SIMPLE iteration does but instead does so with regards to p^{***} and ϕ_p^{***}. The SIMPLE and PISO algorithms are outlined in Figure 4.5.

Boundary condition implementation and algorithms

Boundary conditions are implemented by constructing additional nodes surrounding the 'physical' boundary so that cell centres are fixed along the boundaries, and by introducing very large source terms to those cells. To set ϕ_p to the fixed value ϕ_{fix} the discretised momentum equation for that cell is modified according to

$$a_p = a_p + c_L, \quad \text{and} \quad b = b + c_L \phi_{fix}. \tag{4.75}$$

The large value of c_L chosen for applying the boundary sources is arbitrary in magnitude as long as it is very large relative to all of the coefficients of the discretised equations. To apply a pressure boundary condition the pressure correction equation is modified for the boundary cells according to

$$b' = b' + c_L. \tag{4.76}$$

Point-iterative solution method

The system of equations resulting from realistic CFD problems are usually very large with sparse coefficient matrices. These systems are generally found to be solved more economically by iterative methods with preconditioning. A further advantage to iterative techniques in large scale CFD problems is that they also require less core memory.

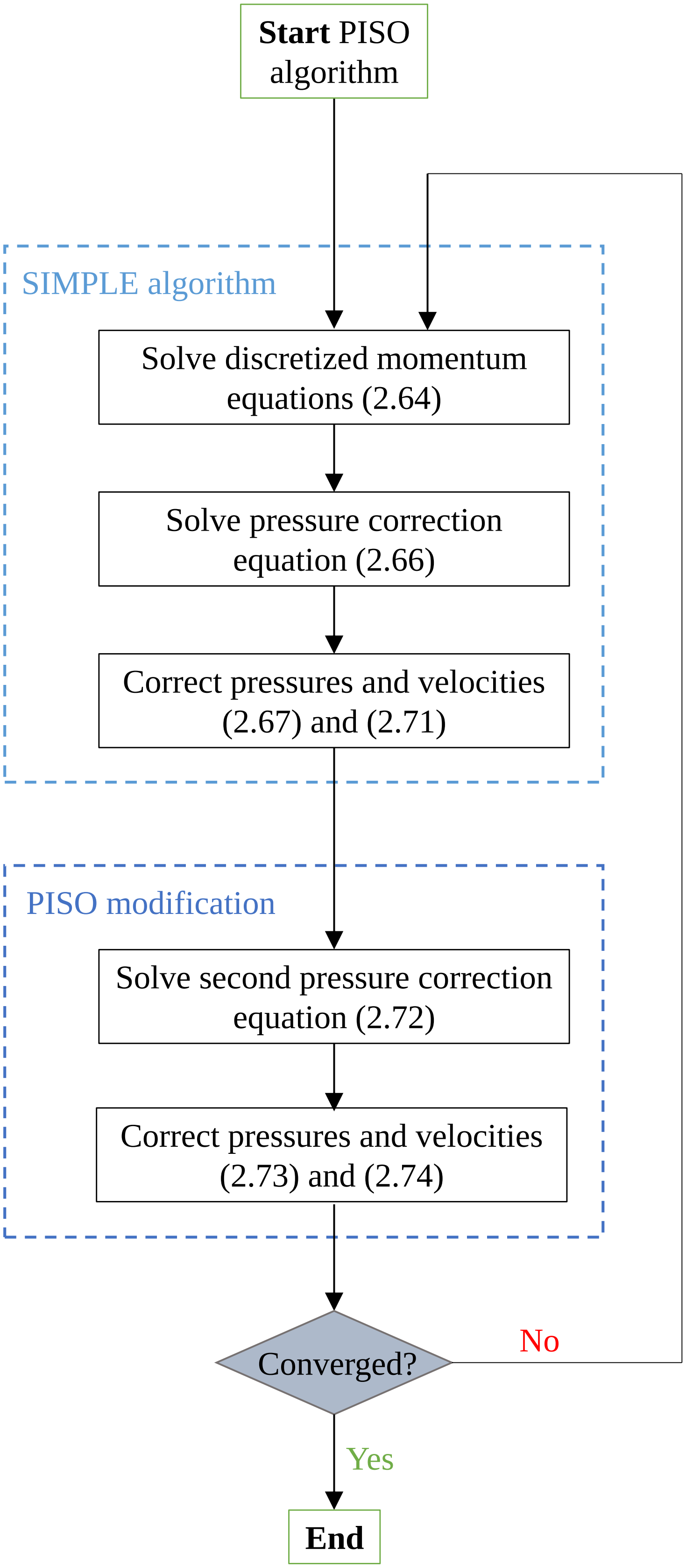

Figure 4.5: The SIMPLE and PISO algorithms

The linear systems are solved using a point implicit Gauss-Seidel equation solver in conjunction with an algebraic multigrid preconditioning. The Gauss-Seidel method is over-relaxed; that is,

$$x_i^k = x_i^{k-1} + \alpha \left[\sum_{j=1}^{i-1} \left(\frac{-a_{ij}}{a_{ii}} \right) x_j^k + \sum_{j=i}^{n} \left(\frac{-a_{ij}}{a_{ii}} \right) x_j^{k-1} + \frac{b_i}{a_{ii}} \right], \tag{4.77}$$

with an over relaxation factor α in the range of 1.06 to 1.08.

Residuals and convergence

Convergence of the solution is based on the scaled residuals to the momentum and continuity equations. The scaled residual of the discretised momentum is calculated according to

$$R_S^{\phi} = \frac{\sum_{cells\ p} \mid \sum_{nb} a_{nb}\phi_{nb} + b - a_p\,\phi_p \mid}{\sum_{cells\ p} \mid a_p\,\phi_p \mid} \tag{4.78}$$

when the momentum and continuity residuals fall below their tolerances the PISO algorithm loop ends.

4.3 Partitioned fluid-structure interaction modelling

Coupling a fluid model with a solid model is necessary when the interaction between the fluid and solid is significant. Since the mechanics of the fluid and solid differ they cannot be modelled together as a continuous whole. A monolithic approach can be taken where the coupling forms a single set of equations so that the FSI is solved in a single system. However, a partitioned (staggered) approach is the preferred method in FSI modelling where the fluid and solid are solved as two separate systems sequentially.

A number of staggered coupling methods exist. For strongly coupled FSI problems implicit coupling is necessary to mitigate the numerical instability inherent in partitioned FSI schemes known as the *artificial added mass effect*. To overcome this instability for the strongest coupled problems, certain relaxation techniques may also need to be included in implicit coupling. The monolithic coupling approach does not suffer from the added mass effect, however it is affected by a number of its own numerical issues.

This section gives a brief description of partitioned FSI modelling. More details on the FSI may be found for example in [100]. For a more detailed description of the approach used in this project please refer to the ANSYS Fluent User's Guide and the ANSYS System Coupling User's Guide [97, 101].

4.3.1 The semi-implicit staggered algorithm

The implicit staggered solution method may be started by solving either the fluid or solid model first. In the case where the forces on the solid are completely dependent on the fluid solution, the fluid is solved first. The fluid and solid are solved once each coupling step where the boundary solutions are transferred to the opposite solver once each solve is completed. The fluid and solid models are solved sequentially in this way until the change in both of the boundary solution transfers are considered negligible.

The General Grid Interface (GGI) algorithm presented in [102] is used in transferring the fluid model boundary solution, the pressure, as a conservative variable force, from the fluid boundary mesh to the solid boundary nodes. To transfer the non-conservative solid boundary solution, the displacement, the Smart Bucket (SB) algorithm described in [103] is used.

Once the fluid model receives its boundary displacement data from the solid model solution it needs to perform a number of mesh smoothing operations as explained in the next section. The boundary conditions are then updated and the fluid model is subsequently solved. If the fluid is only solved fractionally each coupling step the coupling is considered semi-implicit. This method of coupling helps in providing techniques to overcome the added mass instability discussed in Section 4.3.3. The semi-implicit coupling algorithm procedure used in this project is illustrated in Figure 4.6 where n_{fi} fluid iterations are done each coupling step.

The FSI system is converged when the change in the solution transfers between coupling steps have both converged along with the fluid FVM iterations. The solid model converges fully during each coupling step. The fluid model is required to solve at the end of each time step, regardless of if the staggered sequence starts with the fluid, so that the FSI boundaries are conformal at the end, and start, of each time-step. Coupling convergence is determined at the end of each coupling step from the normalised

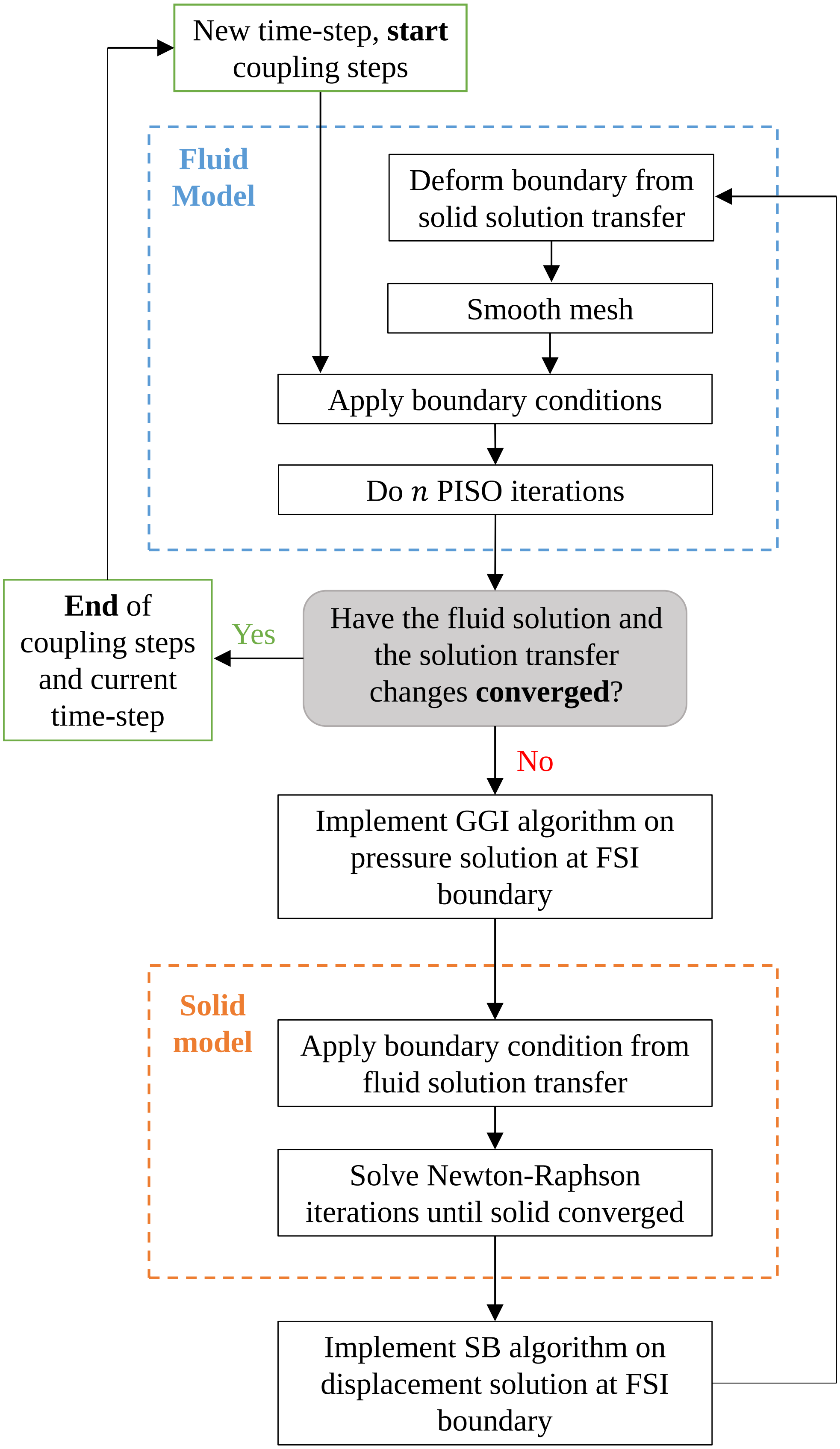

Figure 4.6: The semi-implicit staggered FSI coupling algorithm

root mean square of the change in the solution transfer which is given by

$$RMS_{change} = \sqrt{\left(\frac{\phi_i^n - \phi_i^{n-1}}{\frac{1}{2}\left(\left(\max|\phi| - \min|\phi| + |\bar{\phi}|\right)\right)}\right)^2} \tag{4.79}$$

where $|\bar{\phi}|$ is the mean of the magnitude of the data transfer values over the boundary.

4.3.2 Finite volume mesh adaption

The FSI boundary deformation causes the fluid FVM cells that share faces with the boundary to be deformed. To ensure that these cells maintain their mesh quality, the rest of the mesh is usually deformed by a mesh smoothing algorithm. The FVM requires a modification to incorporate the motion of the mesh.

A spring-based mesh smoothing algorithm was used to deform the mesh according to the FSI boundary deformation and maintain a good quality mesh. The method is efficient and performs well when the boundary deformation is predominantly normal to the boundary itself. Spring-based smoothing works best for tetrahedral cells but still performs well on non-tetrahedral meshes when there is very little tangential deformation of the mesh.

In this method the edges between any two mesh nodes are idealised as springs to form a network of interconnected springs. Displacement of the boundary mesh nodes cause an imbalance in the forces of the spring network according to Hooke's Law. Jacobi sweeps on all the interior nodes solve the equilibrium equation iteratively to a chosen convergence criterion such that the interior nodes deform with the boundary.

A second-order backward difference approximation of the first term in the above equation yields

$$\int_{\Omega} \frac{\partial\left(\rho\,\phi\right)}{\partial t}\,\mathrm{d}v + \int_{\partial\Omega} \rho\,\phi\Big(\left(\boldsymbol{v} - \boldsymbol{v}_m\right)\cdot\boldsymbol{n}\Big)\,\mathrm{d}a = \int_{\partial\Omega} \mu\,\mathrm{grad}\;\phi\,\boldsymbol{n}\;\mathrm{d}a - \int_{\partial\Omega} p\,\boldsymbol{n}\cdot\boldsymbol{e}_{\phi}\;\mathrm{d}a. \tag{4.80}$$

The approximation to first term in the equation above by the second-order backward differencing gives

$$\frac{\mathrm{d}}{\mathrm{d}t}\int_{\Omega}\rho\,\phi\;\mathrm{d}v=\frac{3\,(\rho\,\phi)^{t+\Delta t}-4\,(\rho\,\phi)^{t}+(\rho\,\phi)^{t-\Delta t}}{2\Delta t} \tag{4.81}$$

where the cell volume at $t+\Delta t$ is determined according to

$$V^{t+\Delta t}=V^{t+\Delta t}+\frac{\mathrm{d}V}{\mathrm{d}t}\,\Delta t. \tag{4.82}$$

To satisfy the mesh conservation law the volume time derivative of the control volume is calculated according to

$$\frac{\mathrm{d}V}{\mathrm{d}t}=\int_{\partial\Omega}\boldsymbol{v}_m\cdot\boldsymbol{n}\;\mathrm{d}a. \tag{4.83}$$

For second-order differencing scheme the volume time derivative of the control volume is given by

$$\frac{\mathrm{d}V}{\mathrm{d}t}=\frac{3}{2}\left(\sum_f\left(\boldsymbol{v}_m\right)_f\cdot\boldsymbol{A}_f\right)^{t}-\frac{1}{2}\left(\sum_f\left(\boldsymbol{v}_m\right)_f\cdot\boldsymbol{A}_f\right)^{t-\Delta t}. \tag{4.84}$$

4.3.3 The added-mass effect

The added-mass effect occurs as a result of the solutions and boundary conditions between the two models not being in sync. This effectively means that the solid model displaces and entrains fluid making the structural model appear to have ‘added-mass’. This ‘added-mass’ acts on the structural degrees of freedom at the interface between the solid and fluid [104].

The stronger the physics coupling between solid and fluid, the more unstable the added mass-effect becomes. The following criteria give a stronger coupling between the fluid and solid:

- a lower stiffness solid,
- a thinner solid geometry,
- a higher viscosity fluid,
- a greater pressure changes within the fluid,

- and the closer the fluid-solid density ratio is to unity.

When the added-mass effect is unstable a number of numerical modifications can be made to diminish the effect. If the temporal resolution requirements allow, a larger time-step size can be used to reduce effect of the instability. However, the best approach is to converge only fractionally toward the solution of either or both of the underlying models each at coupling step.

Iterative solvers give more flexibility in this regard by allowing one to converge only partially either, or both, of the physics models in a number of ways. In this case, decreasing the number of iterations per coupling step can greatly improve the stability of staggered coupling. Stability can also be increased by using more under-relaxation.

A useful technique in very strongly coupled FSI problems is to modify the FVM continuity equation so that the diagonal entries of the linear matrix system are rescaled according to

$$a_{ij} = a_{ij} + KV\delta_{ij} \tag{4.85}$$

for all $i, j \in 1, 2, ..., n_b$, where n_b is the number of cells adjacent to the FSI boundary, K is the scaling factor and V is the volume of the cell adjacent to the boundary. The Kroenecker delta function δ_{ij} is defined as

$$\delta_{ij} = \begin{cases} 0 & \text{if } i \neq j, \\ 1 & \text{if } i = j. \end{cases} \tag{4.86}$$

Increasing the scaling factor K improves the diagonal dominance of the cells adjacent to the coupling interface. This slows convergence rate of the fluid such that the force transfer changes are more smooth. The effect is similar to that of under-relaxation but is applied only to the solution on the boundary. The strength of the boundary source coefficient stabilisation method is that it slows the rate of convergence primarily on the boundary so that less overall efficiency is lost in modelling the FSI problem.

Chapter 5

Implementation, results, and analysis

In this chapter we present details of the implementation of the FSI model, as set out in the previous chapter, with specific reference to the patient-specific example. The patient-specific fluid model geometry is defined from PC-MRA scan data of a dialysis patient's arteriovenous fistula. The numerical model is configured and simulated in ANSYS® Fluent® software. The vessel wall geometry and mesh are then constructed from the fluid model mesh and used to define the solid model which is implemented in ANSYS® Mechanical™software. These two models are combined in ANSYS® Workbench™ software to form the patient-specific FSI model.

The structure of the chapter is as follows. In the Section 5.1 we present the MRI data and show how it has been manipulated and utilised to develop the patient-specific geometry and boundary conditions (BCs). In Section 5.2 we detail the set-up of the patient-specific fluid model, describe some of its features and characteristics, and present a mesh convergence analysis. We do the same for the patient-specific solid in Section 5.2, while also examining the behaviour of a number of element choices in the convergence analysis. The FSI model preprocessing requirement are then detailed in Section 5.4. The behaviour of this model is analysed and the results described in comparison with that of the fluid model.

5.1 PC-MRA acquisition and post-processing

The case studied is a brachio-cephalic fistula. All data were acquired from a number of PC-MRA scans which took place at Groote Schuur Hospital (Cape Town, South Africa). These were performed with a 1.5T MRI scanner (MAGNETON Symphony Siemens AG, Erlangen) with ECG leads providing data for cardiac gating. The images were sequenced and processed by our collaborator as described in [82]. The acquisition methods used were based on the 3D MRI velocity mapping package presented in [105].

A number of scans were done to first test and configure the PC-MRA and post processing technique. These were carried out in five healthy volunteers, five dialysis patients with a fistula and three with a graft. The scans on the patients were performed a minimum of 6 hours after dialysis treatment took place. No attempt was made however to control for relative hyperaemia, where higher blood flow rates than normal may arise after exercise or fluid consumption. Access patients were recruited from the chronic haemodialysis program at Groote Schuur Hospital Renal Unit.

The 3D velocity encoded acquisitions were performed relative to the sagittal plan. 2D PC-MRA scans were also performed in the axial plane. The region of interest was positioned such that the patients' entire vascular access could be captured with one set of acquisitions. Two slices were chosen at proximal and distal sites in the upper arm to record velocities with greater accuracy at the inlets and outlets of the arteries, veins, and/or grafts. Since it is only the orthogonal component of the velocity of these slices that is measured, the patients arm was positioned as best as possible such that the inlets and outlets ran perpendicular to the axial plane (the principal direction of flow is axial to the vessel). The 3D scans took between 20 and 30 minutes to complete, while the 2D scans took approximately one minute. The details of the sequences used in the scans for each of the patients are shown in Table 5.1 for the 2D scans and Table 5.2 for the 3D scans.

Images were first processed to remove typical noise and eddy currents. A new spatio-temporal algorithm, presented in [82], that combined the temporal phase unwrapping and Goldstein-Zebker-Werner cut methods [106], was used to unwrap the 2D data obtained from the haemodialysis patients. Each patient's 3D flow data were processed in the axial, or z-, direction. The scanning parameters used to scan the volunteers and patients are given in Table 3.1. Volunteer scans were used to optimise and test parameters for the patient scans.

Table 3.1: Details of 2D PC-MRA scans for volunteers and patients

Table 5.1: Details of the 2D PC-MRA scans for volunteers and patients [82]

Patient ID	v_{enc} **[cm/s]**	**№of Images**	**Pixel Spacing [mm/mm]**	**TR [ms]**	**TE [ms]**	**Flip Angle [°]**
Volunteer 1	15 30 40 60	12 22 22 22	0.70/0.70 0.70/0.70 0.94/0.94 0.94/0.94	84.0 49.6 46.4 44.0	4.17 3.41 3.17 2.89	15
Volunteer 2	20 80	9 11	0.70/0.70	79.2 66.0	3.82 2.73	15
Volunteer	[illegible]	[illegible]	[illegible]	[illegible]	[illegible]	15
Volunteer	[illegible]	[illegible]	[illegible]	[illegible]	[illegible]	15
Volunteer	[illegible]	[illegible]	[illegible]	[illegible]	[illegible]	15
Fistula	[illegible]	[illegible]	[illegible]	[illegible]	[illegible]	15
Fistula	[illegible]	[illegible]	[illegible]	[illegible]	[illegible]	15
Fistula	[illegible]	[illegible]	[illegible]	[illegible]	[illegible]	15
Fistula 4	80	14	0.70/0.70	66.0	2.73	15
Fistula 5	80 150 350	57 66 28	0.70/0.70	11.0 10.4 24.0	2.73 2.46 3.23	15
Graft 1	20 80	12 14	0.70/0.70	79.2 66.0	3.82 2.73	15
Graft 2	80	10	0.70/0.70	66.0	2.73	15
Graft 3	20 80	12 14	0.70/0.70	79.2 66.0	3.82 2.73	15

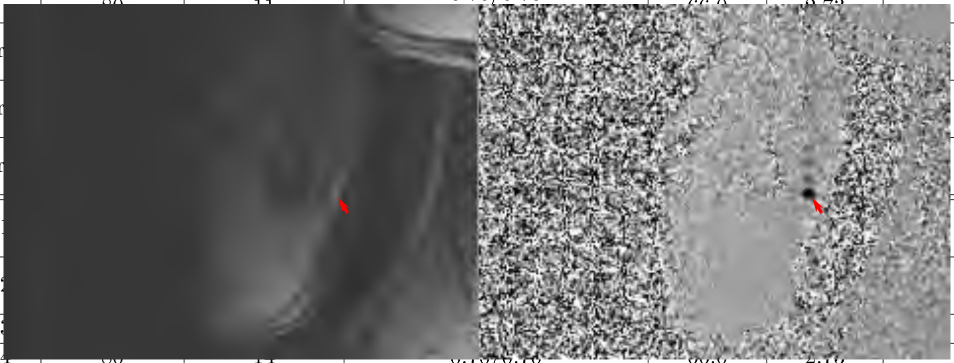

Figure 3.1: 2D PC-MRA magnitude and phase images; the red arrows show the location of the brachial artery. Flow from head to toe appears darker in the phase image.

3.2.2 4D PC-MRA

The 4D acquisition was performed in the sagittal plane and used velocity encoding in three orthogonal directions, that is the x-, y-, and z-directions. Table 3.2 gives the parameters used for each patient scan.

Two slices were chosen at proximal and distal sites in the upper arm of both patients and volunteers; a third slice was also chosen at the level of the anastomosis of each patient.

Table 3.2: Details of 4D PC-MRA scans for volunteers and patients

Several images were acquired during the course of several cardiac cycles at different time points, this produces a set of 2D magnitude and phase images over one cardiac cycle. These scans can be performed in approximately one minute.

Table 5.2: Details of the 3D PC-MRA scans for volunteers and patients [82]

Patient ID	v_{enc} **[cm/s]**	**№of Images**	**№of Slices**	**Pixel Spacing [mm/mm]**	**Slice Thickness [mm]**	**TR [ms]**	**TE [ms]**	**Flip Angle [°]**
Volunteer 1	60	20	20	1.72/1.72	2	45.6	3.10	7
Volunteer 2	20 90	14	20	1.56/1.56	2	56.0 52.8	4.38 3.89	7
Volunteer 3	20 90	28	16	1.56/1.56	2	27.2 26.4	4.18 3.89	7
Volunteer 4	90	26	16	1.56/1.56	2	26.4	3.89	7
Volunteer 5	20	28	16	1.56/1.56	2	27.2	4.18	7
Fistula 1	90	28	30	1.56/1.56	2	26.0	3.89	7
Fistula 2	20	28	16	1.56/1.56	2	27.2	4.18	7
Fistula 3	90	28	30	1.56/1.56	2	26.0	3.89	7
Fistula 4	90	28	40	1.56/1.56	2	26.4	3.89	7
Fistula 5	250	12	32	1.56/1.56	2	11.0	2.73	7
Graft 1	20	28	26	1.56/1.56	2	27.2	4.18	7
Graft 2	90	28	24	1.56/1.56	2	26.0	3.89	7
Graft 3	20	28	16	1.56/1.56	2	27.2	4.17	7

The imaged 3D volume was positioned in the volunteers' upper arm so that both the brachial artery and cephalic vein could be measured in one acquisition. For the patients, the volume was chosen to cover the brachial artery, the cephalic vein or graft, the anastomosis of the artery and vein or graft, and the brachial artery distal to the anastomosis.

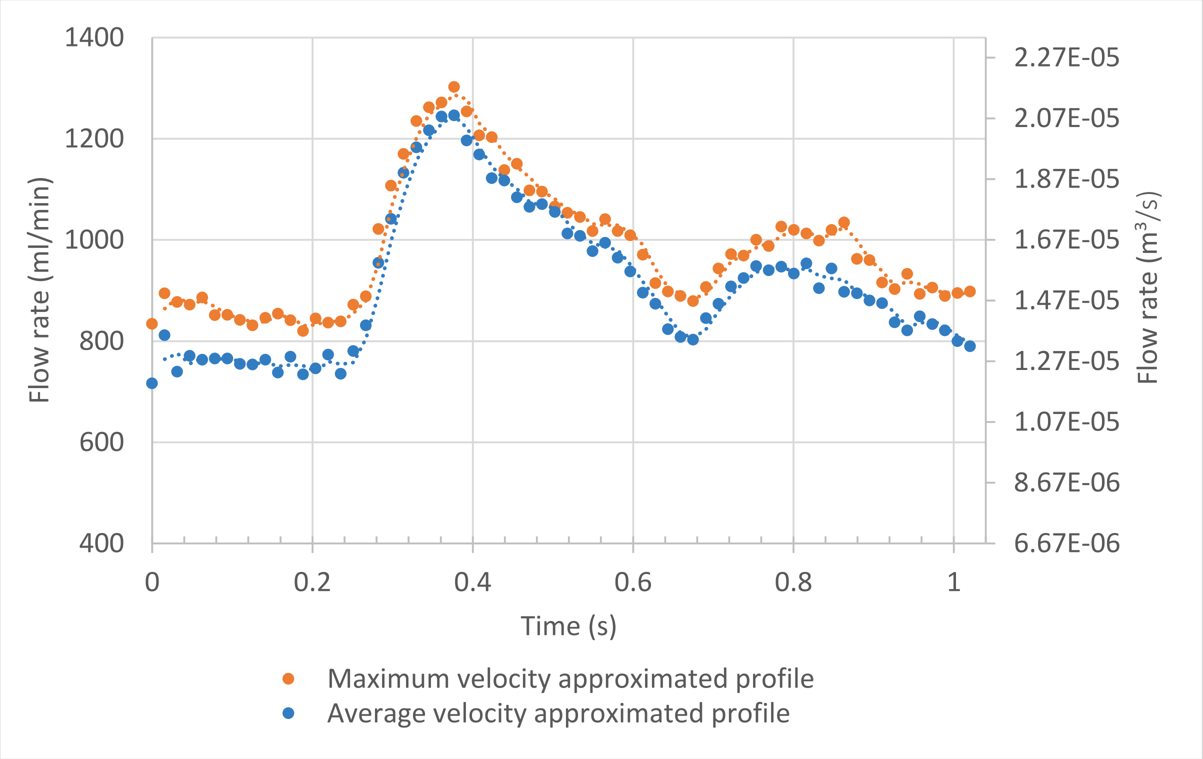

Figure 5.1: The flow rate waveform profiles approximated from the 2D PC-MRA inlet scan of patient 'Fistula 5'

to remove wrapping artefacts with a 3D branch cut method adapted from [107] and [108]. Unwrapping failed in 38 to 43 % of the data sets due, in part, to the low spatial resolution in relation to the geometry size, and to excessive wrapping caused by specifying an inadequate v_{enc} setting for a specific patient's vascular access blood flow characteristics.

Inlet flow rate profiles have been calculated from the 2D PC-MRA velocity data, positioned at the artery upstream of the anastomosis, of the patient-specific fistula under consideration (Patient ID - Fistula 5). The corresponding profiles are shown in Figure 5.1. The processed data from this scan was chosen for our model as it was determined to have superior flow and geometric data quality. The temporal resolution of this scan was set at 0.0157 sec and a pulse period of 1.02s was recorded by the ECG unit. We have used two methods to approximate the flow rate at the artery inlet. The maximum velocity recorded is used in the first, where it is assumed that the flow profile at the inlet is parabolic. In the second method a summation of velocity contribution from each voxel is taken to obtain the average velocity.

A further assumption that we were required to make in each of the methods above is that the inlet diameter stays constant and is circular. It also needs to be noted that it is

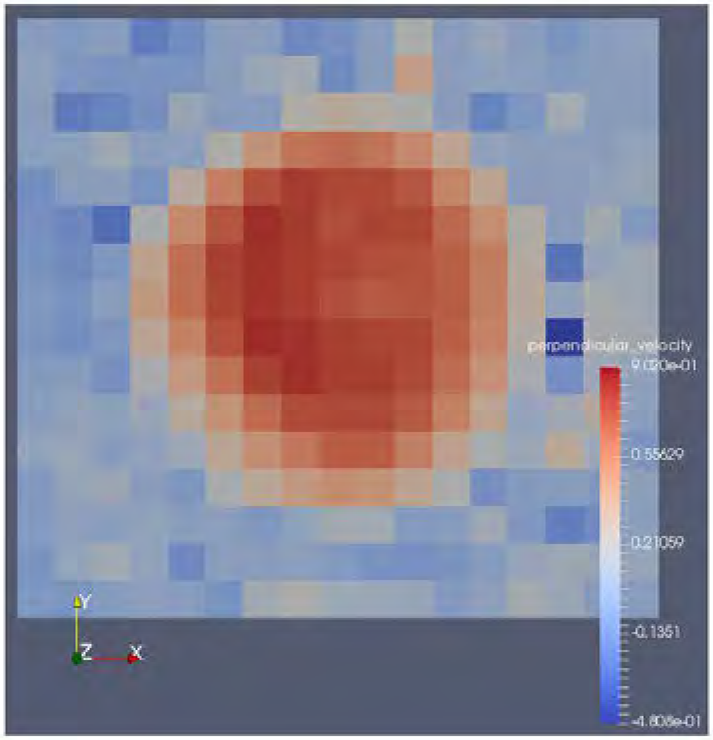

Figure 5.2: A rendering of the velocity data taken from the 2D PC-MRA inlet scan at peak flow. Each square pixel is a 2D voxel; the blue region surrounding the inlet is residual signal noise.

difficult to ascertain exactly where the vessel wall is located, as can be seen in Figure 5.2. Each of these assumptions introduces errors in the approximations of the flow rate. This inlet data could not be implemented in our models due to complications in the scans and the retrieval of data. The maximum velocity and average velocity methods result in a time-averaged flow rate of 980 ml/ min and 911 ml/ min respectively.

The results of the 3D PC-MRA scan were processed to visualise the measured velocities with velocity streamlines, this is shown in Figure 5.3.

5.2 Patient-specific fluid model

5.2.1 Geometry reconstruction of the fluid domain

The spatial data of the blood flow domain is extracted from the 3D PC-MRA scans. These data come in the form of a point-cloud dataset, this is represented in Fig-

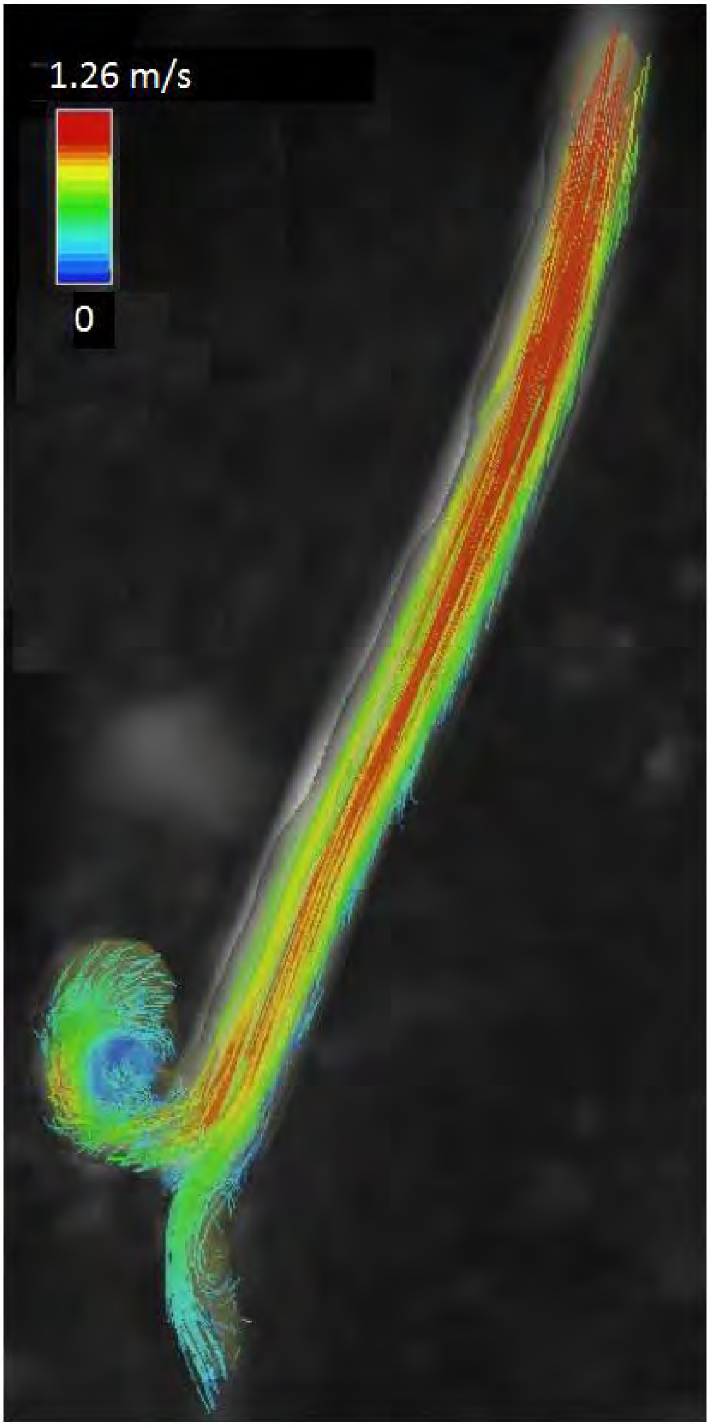

Figure 5.3: Patient ‘Fistula 5’ 3D PC-MRA velocity streamlines processed and generated by [82].

ure 5.4(a). Due to the relatively low spatial resolution of the 3D sequence and the size of the region of interest, a large amount of geometrical post-processing was required to smooth, simplify and extend the domain to create an acceptable fluid model. Attempts to automate the extraction and smoothing of the geometry using a number of software programs failed to generate a suitable and accurate approximation of the fluid domain; an example of such an outcome is shown in Figure 5.4(d). We were able, however, to generate a satisfactory fluid geometry by combining a number of manual 3D modelling construction techniques with several automated 3D modelling tools. The method is now summarised.

The points forming the outer surface of the point-cloud were extracted with MeshLab, an open source post-processing tool for 3D scans. An alpha meshing filter was applied to the point-cloud to produce the rudimentary surface mesh shown in Figure 5.4(b). A surface point-cloud could then be extracted from this alpha mesh, the result is shown in Figure 5.4(c). The surface point-cloud data was then exported to Solid Works® to develop, smooth and extend the boundaries of the fluid model domain.

Smooth circular curves were created manually through the surface points in planes perpendicular to the axis of the artery in one case, and the vein in the other (see Figure 5.4(e)). Two cylindrical surfaces were then swept through the curves constituting the artery and vein. These surfaces were blended together with a rounding tool to best follow the surface point-cloud at the anastomosis. Surfaces were then created perpendicular to the axis at each end of the artery and vein to enclose the fluid domain. This surface model, shown in Figure 5.4(f), was then exported to ANSYS® DesignModeler™ to ensure its compatibility with ANSYS Fluent software for final editing.

The ends of the domain were extended to varying degrees in DesignModeler to ensure that the inlet and outlet lengths were sufficiently long for the fluid model (see Section 5.2.2). The final fluid model is shown in Figure 5.5. Here the blood flow directions, and their relative flow rates (see Section 5.2.2), are indicated by the arrows. The artery inlet is indicated by A_i, while the artery and vein outlets are indicated by A_o and V_o, respectively. The line $A_N - A_N$ cutting across the model at the junction is the point at which the vein meets with the artery and forms the anastomosis, this is the approximate suture location of the fistula.

The length of the domain from the inlet to the anastomosis is approximately 100 mm,

(a) Raw MRI data point-cloud

(b) Alpha surface mesh

(c) Surface point cloud

(d) Automatic surface generation

(e) Manual surface generation

(f) Final SolidWorks geometry

Figure 5.4: Process by which the blood flow domain is developed: from (a) the raw MRI point-cloud data processed in MeshLab to (f) the final geometry created and smoothed in SolidWorks

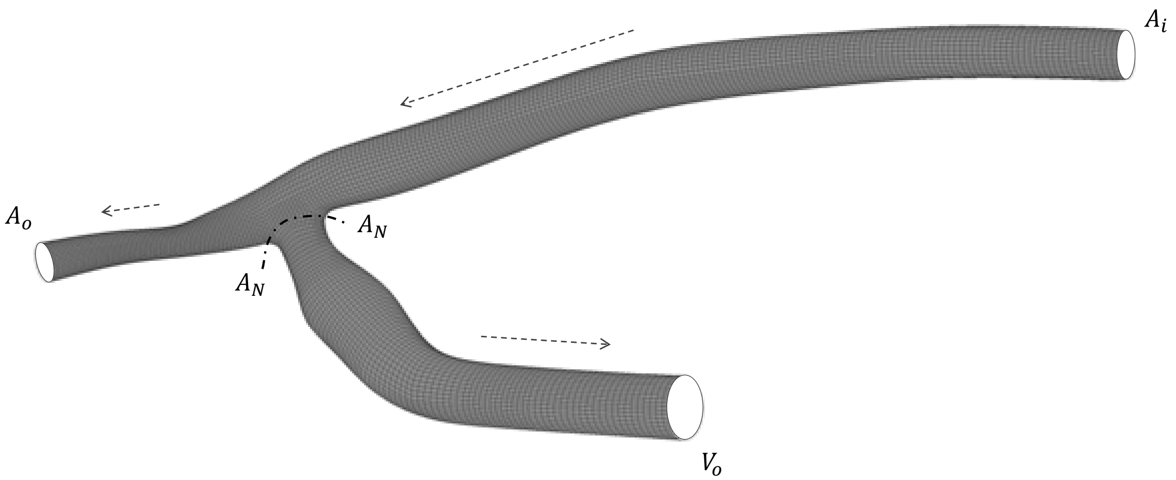

Figure 5.5: A view of the patient-specific fluid domain boundaries; blood flow directions are highlighted by dashed arrows.

while the lengths from the anastomosis to the artery outlet and to the vein outlet are 27 and 59 mm respectively. The average artery inlet, artery outlet, and vein outlet diameters are 6.89, 4.15, and 5.23 mm and have areas of 37.8, 13.4, and 21.2 mm^2, respectively.

5.2.2 Material behaviour and boundary conditions

Blood flows in a pulsatile manner from the brachial artery upstream toward the anastomotic junction of the fistula where it is shunted primarily back through the cephalic vein, the low resistance pathway, toward the heart as shown in Figure 1.1(a). The smaller proportion of blood that continues along the artery flows toward the down stream vessel structure, including the arterioles and capillaries in the lower arm and hand. The blood is modelled as a Newtonian fluid while the upstream, and down stream behaviour, is replicated with inlet flow rate profile and lumped parameter model outlet boundary conditions respectively.

In the arterial system of the arm, blood ordinarily demonstrates Newtonian behaviour, where the viscosity remains relatively constant, as a result of high shear rates (of above $100\,\mathrm{s}^{-1}$). However, shear rates lower than $100\,\mathrm{s}^{-1}$ are likely to occur in the mature vein of an AV shunt where velocities are lower due to the bifurcation of flow and considerable enlargement of the vessel. This results in shear-thinning due principally to Rouleaux disaggregation in blood plasma [109]. The significant non-Newtonian behaviour is more accurately simulated by a Casson or Carreau-Yusada material model [110].

Although studies have found that WSS in the enlarged veins of fistulae are under-predicted by a Newtonian model [66, 111], we decided to model it as such and limit the complexity of the fluid model to focus on creating an optimally stable FSI model. We thus assume blood to be an isotropic, homogeneous, and incompressible Newtonian fluid with a density of $1050\,\mathrm{kg\,m^{-3}}$ and a viscosity of $3.2\,\mathrm{Pa\,s}$. Note that Decorato et al. [66] found that the once the numerical instability brought about by the implementation of a Casson model was stabilised, its computational expense was comparable to that of a Newtonian model.

A standard approach in finite-volume method fluid modelling is to prescribe a velocity BC at the inlet of a domain and a pressure at the outlet, or outlets, for a well posed and robust numerical system [96]. Since the artery inlet face is not perfectly circular we were not able to prescribe a parabolic velocity profile at A_i. Instead of recreating a perfectly circular inlet we chose to prescribe a mass flow inlet condition at the artery inlet, an equivalent BC in incompressible flow problems. This produces a spatially constant velocity profile across the inlet that mimics the one prescribed in [66] over each cardiac-cycle. The mass flow inlet waveform M_i is shown in Figure 5.6. The cardiac-cycle period is $0.8\,\mathrm{s}$, and has a time-averaged flow rate and velocity of $616\,\mathrm{ml/\min}$ and $0.49\,\mathrm{m\,s^{-1}}$ respectively. This profile has been used in place of the MRI velocity data for reasons explained in Section 5.1.

Prescribing a mass flow rate BC results in a uniform velocity distribution that is unphysical; however, this is admissible provided that the inlet is far enough upstream for the physically accurate flow profile to develop before reaching the region of interest, the anastomosis in our case. Prescribing a parabolic velocity at the inlet would likely have allowed have allowed the use of a shorter inlet length, decreasing the number of DOF and thus the computation time for the fluid and FSI models. The pressure outlet BCs are imposed by a Windkessel, or lumped parameter model, as described in Section 5.2.2, while a no-slip boundary condition is imposed on the walls of the vessel.

The assumptions and BCs above result in a Womersley number and effective Reynolds number of 6.5 and 1124 respectively in the artery upstream of the anastomosis. Lam-

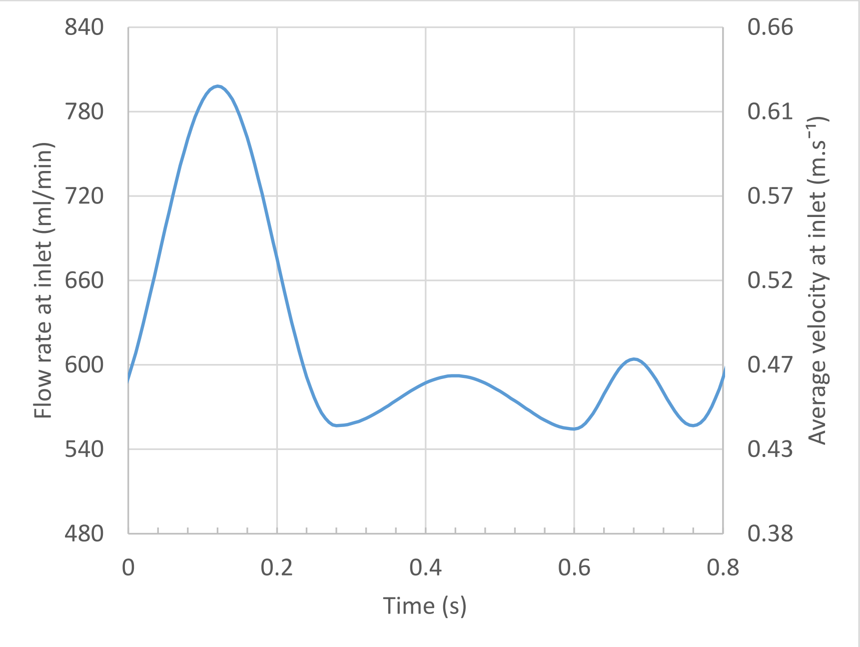

Figure 5.6: The mass flow boundary condition waveform prescribed at the artery inlet of the fluid model

inar flow is thus predicted in the entire domain with a boundary layer thickness of approximately 0.6 mm, a third of the radius of the inlet. The pulsatile nature of blood flow causes the flow profile to deviate from a parabolic (Hagen-Poiseuille) flow profile toward plug-like flow. This results in the flow profile developing more quickly than it would in the steady case [112, 113], at approximately 98 mm from the inlet. The entrance length was thus extended to a total of 100 mm, as described in the preceding section, to ensure that a fully developed flow profile is established before reaching the anastomosis. It should be noted that turbulent or "transition" flows occur in certain larger vessels where flow rates are much higher. This could also potentially develop in vascular access when abnormally high flow rates arise and/or due to the surface roughness of the vessel walls [114].

The lumped parameter model

A lumped parameter model simplifies the partial differential equations of a model of a physical system into ordinary differential equations with finite numbers of parameters. Lumped parameter models have been used extensively in modelling the cardiovascular system as electric circuit analogues, particularly the system of vessels downstream of the domain of interest [115–117]. This would otherwise be impractical and would likely be more susceptible to modelling error. In our fluid simulations we have tested purely

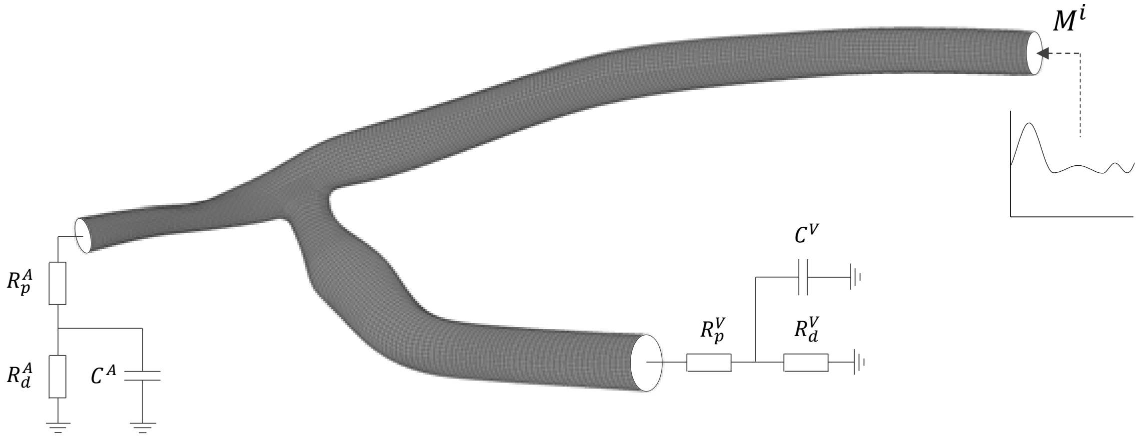

Figure 5.7: The boundary conditions applied at the inlet and outlets of the patient-specific blood flow model

resistive outlet models, as well as, two- and three-element Windkessel models. These models mimic the upstream vessel resistance, and in the case of the Windkessel models, the downstream vessel resistance and compliance as well.

We have implemented both types of Windkessel model with the three-element RCR Windkessel model shown in Figure 5.7. The electric circuit analogue of this model is a resistor, in series with a resistor and capacitor that are in parallel. The first, and lone, resistor acts as the proximal resistance (upstream resistance). The resistor and capacitor model the distal resistance and compliance of the downstream vascular bed respectively. The two-element Windkessel RC Windkessel model, used in [66], is simulated with the RCR Windkessel model by giving the proximal resistor negligible resistance. The differential equation of the three-element RCR Windkessel model is given by

$$\frac{\partial p}{\partial t} = R_p \frac{\partial Q_o}{\partial t} + \frac{p_o}{\tau} + \frac{p\,(R_p + R_d)}{\tau}, \tag{5.1}$$

where R_p and R_d are the proximal and distal resistance, Q_o is the volumetric flow rate at the outlet, and p_o is the average static pressure at the outlet. The time constant τ describes how quickly the system responds to a changes in flow rate and is given by $\tau = R_d\,C$. The state-variable form of the Windkessel equation is given by

$$p_o(t) = \big[p_0 - R_p\,Q_o(0)\big]\,e^{-t/\tau} + R_p\,Q_o + \int_0^t \frac{\exp[(\tilde{t} - t)/\tau]}{C} Q_o(\tilde{t})\,\mathrm{d}\tilde{t}. \tag{5.2}$$

The state variable form takes advantage of the viscoelastic like behaviour of the Windkessel model so that the difficulty in retaining history data in the numerical scheme is avoided. Dropping the first term in the equation and discretising implicitly by the Crank-Nicolson method, we obtain

$$p_o^{t+\Delta t} = R_p\, Q_o^{t+\Delta t} + \frac{h^{t+\Delta t}}{C}, \tag{5.3}$$

where $h^{t+\Delta t}$ is given by

$$h^{t+\Delta t} = \frac{\Delta t}{2}\, Q_o^{t+\Delta t} + \exp\left(\frac{\Delta t}{\tau}\right)\left(h^t + \frac{\Delta t}{2}\, Q_o^t\right). \tag{5.4}$$

The term $\left[p_0 - R_p\, Q_o(0)\right] e^{-t/\tau}$ in equation (5.2) can be neglected since it becomes negligible in less than one and a half cardiac-cycles and the simulation needs to be run longer than this to become sufficiently periodic (see Section 5.2.4). The resistance of the walls of the model itself also have an affect on the flow rate split in the model, and as periodicity is not reached any sooner if this term is retained, it was neglected. The purely resistive lumped parameter model is given simply by $p_o(t) = R_p\, Q_o$ and reaches periodicity in approximately the same time as the Windkessel outlet fluid models.

The ability to apply lumped parameter type BCs is not a standard feature in ANSYS Fluent software. However, its features can be enhanced and customised by writing a User-Defined Function (UDF), which is compiled and then implemented by the fluid solver each fluid iteration (FI). The solver executes specific *DEFINE* Macros at different stages of the solution process to carry out functions that the user defines. The details of the *DEFINE* Macros we implemented in the UDF are summarised in Table 5.3. The UDF source files were compiled within ANSYS Fluent software.

The following measurements are the minimum required to calibrate the Windkessel models adequately: the pressure at the inlet or one of the outlets, the flow rate at the inlet, and the approximate flow-rate split throughout the model. Increased calibration accuracy of Windkessel models, or more complex lumped parameter models, would be possible with pressure and flow rate waveform measurements at each of the inlets and outlets.

Blood pressure measurements are typically taken with a sphygmomanometer that uses

Table 5.3: Details of the UDF implemented to model the various lumped parameter boundary conditions

*DEFINE_* Macro	Executed at	Source code description:
INIT	Initialisation	Determines on which compute-node each of the outlets are located.
ADJUST	Each iteration	Determines the total flow rate at each outlet, then calculates the lumped parameter outlet pressure for each outlet by equations (5.3) and (5.4).
PROFILE	Each iteration	Applies the calculated pressure at each of the respective outlets.
EXECUTE_AT_END	End of time-step	Sets $h^t = h^{t+\Delta t}$.

an inflatable cuff to determine the systolic and diastolic blood pressure in the upper arm. However, dialysis patient's are instructed never to take the typical inflatable cuff pressure reading on an arm with an access site, since restricting blood flow may lead to access trauma [5]. Regardless, arterial pressures measured by this method are inaccurate and not that of the day to day loading conditions due to the restriction of blood flow.

No pressure data for a brachio-cephalic fistula is currently available to our knowledge. Measuring techniques with an intravascular catheter however have been used post operatively to determine the blood pressure distal to a Brachio-Cimino fistula [118]. This method is invasive but could potentially provide adequte readings of pressure proximal or distal to the anastomosis of a fistula or graft. The viability of this technique, or a non-invasive technique, to accurately pressure data for boundary condition to vascular access requires testing.

We follow the convention used by Decorato et al. [66], whereby the lumped parameter models at each of the outlets are calibrated to induce a flow split between the arterial and venous outlets of 30 % - 70 %, and to generate inlet pressures that range between 50 and 65 mmHg (approximately 6.5 and 8.5 kPa). The total resistance ($R_p + Rd$), and the time-constant (τ), of both lumped parameter outlet models are kept constant across each of the three fluid models. The values are given in Table 5.4.

Table 5.4: Lumped parameter boundary condition details

Outlet	R_p ($\mathrm{Pa\,s\,m^{-3}}$)	R_d ($\mathrm{Pa\,s\,m^{-3}}$)	C($\mathrm{m^3\,Pa^{-1}}$)	$\boldsymbol{\tau}$($\mathrm{s^{-1}}$)
	RCR Windkessel outlet BC model			
Artery	1.12×10^9	1.12×10^9	1.34×10^{-10}	0.15
Vein	4.6×10^8	4.6×10^8	1.74×10^{-10}	0.08
	RC Windkessel outlet BC model			
Artery	2.2×10^6	2.23×10^9	6.73×10^{-11}	0.15
Vein	9.2×10^5	9.2×10^8	8.7×10^{-11}	0.08
	Purely resistive outlet BC model			
Artery	2.23×10^9	-	-	-
Vein	9.21×10^8	-	-	-

5.2.3 Domain discretisation

The domain of the problem is discretised with hexahedral cells so that as few cells as possible are used and hereby minimise the computational expense of the problem. If the mesh is structured well a far improved cell quality can be maintained throughout the mesh to maximise the convergence rate of the fluid model.

The domain is discretised into an unstructured hexahedral mesh by a blocking approach where the geometry is overlaid by blocks that approximate the domain roughly. The edges and faces of the blocks are associated with the relevant edges and faces of the geometry so that an underlying hex mesh of the block is projected onto the geometry. This allows one to use hexahedral meshes on complex domains so that there is greater control over the directionality and quality of the mesh.

This strategy requires effort to set up initially. However, it is possible to automate this process for further models with a script if required. Apart from an increased convergence rate, the motivation for such this procedure is that the computational expense can be drastically decreased in part because a hexahedral mesh typically requires far fewer elements and vertices to mesh a geometry to the same level of accuracy as would be required by a tetrahedral mesh.

In Figure 5.8 we show how a hex block mesh can be applied to a circular domain.

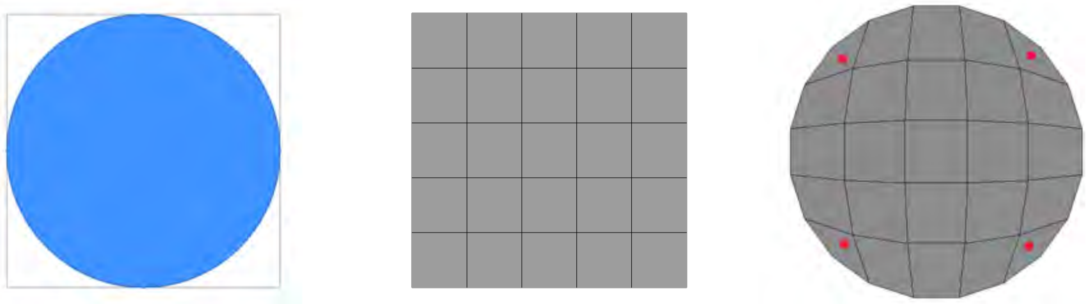

(a) Geometry and block (b) Underlying mesh (c) Mesh projection

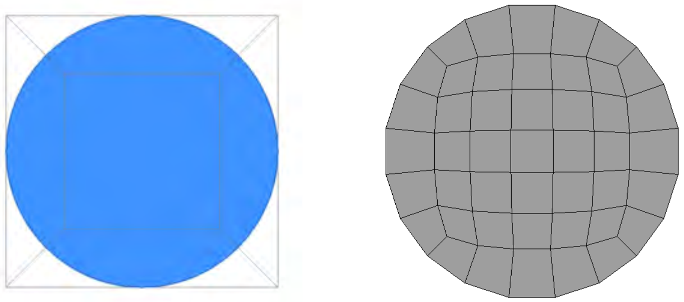

(d) O-grid blocks (e) Final projected mesh

Figure 5.8: The blocking method is shown for a simple geometry: (a) a circular surface (blue) and its block, (b) the blocks' underlying hexahedral mesh, (c) block mesh projection with skewed cells (red dots), (d) block split into an O-grid, and (e) the O-grid blocks' hexahedral meshes are projected onto the geometry generating a boundary layer and high quality of the mesh.

The initial block's underlying mesh is projected onto the edges of the domain. This simple method, however, causes highly skewed cells to form; as highlighted (red dots) in Figure 5.8(c) . Furthermore, the quality of these cells deteriorates further as the mesh is refined. An O-grid strategy, as shown in Figure 5.8(d), alleviates this issue. Additionally, an O-grid is used to generate the boundary layers to accurately capture the velocity gradient near to the wall and to gradually build curvature into the mesh as it reaches the outer circular shaped walls of the domain.

The blocking strategy used in the region of the anastomosis is shown in Figure 5.9. The O-grid at the artery outlet can be seen at the bottom left in each subfigure. In 5.9(a) the outer edges of the blocks (black lines) are projected onto the domain surface. These edges make up the outer faces of the blocks as shown in (b). The inner edges (blue) in (a), project the O-grid and boundary layers throughout the domain, ensuring a high quality mesh for each cell. Each block is shrunk in (c), to better display the internal blocking structure. The resulting mesh is shown in (d), where the boundary layers are visible at the artery outlet.

This blocking structure has further advantages. It ensures that the mesh scales well so that grid quality is maintained as the is refined. The blocking strategy has also been structured to minimise the amount of numerical diffusion by aligning the cells with general direction of flow through the domain. The mesh deformation that takes place in the FSI simulation is prone to developing skew cells, and in some cases cell inversion. This is issue is exacerbated as the quality of the mesh decreases (see Section 5.4.2). Additionally, the displacements of the FSI boundary mesh are predominantly perpendicular to the boundary itself, our strategy thus inhibits mesh deterioration further by ensuring that the cells are principally orthogonal to the outer walls of the fluid domain (the FSI boundary). Triangular prisms can be used with a tetrahedral mesh to accomplishes this to a degree, provided that the boundary layer thickness is large enough and the internal tetrahedral mesh is of sufficient quality.

5.2.4 Solver settings and solution behaviour

A large array of solver schemes and settings were assessed to find the fastest convergence rate while maintaining accuracy. A time-step size of 0.005 s was used for its temporal accuracy, convergence rate, and solution accuracy. The PISO pressure-velocity

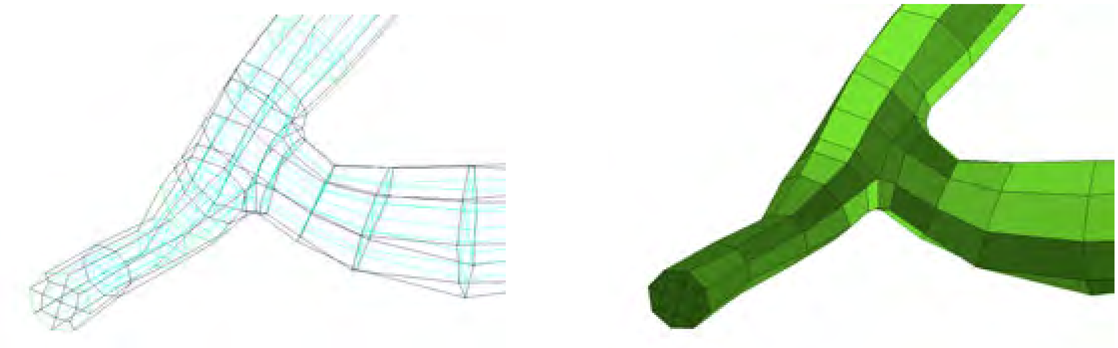

(a) Blocking edges

(b) Complete blocks

(c) Internal blocking

(d) Final mesh 3

Figure 5.9: The blocking strategy used at the anastomosis and artery outlet to generate a high quality hexahedral mesh with an O-grid for boundary layers. The outer edges and surfaces of the blocks are projected onto the geometry.

coupling scheme, described in Section 4.2.5, is the preferred solver in ANSYS Fluent software for transient problems. This scheme did perform best in our model particularly with Skewness Correction and Skewness-Neighbour Coupling deactivated. The under-relaxation factors (URF) were decreased from their default values to address the increased instability caused by the Windkessel outlet BCs. The critical solver settings we have used are summarised in Table 5.5.

For larger time-step sizes the URFs need to be reduced to ensure stability and to attain an optimal, but slower, convergence rate. The opposite is true if the time-step size is decreased with a URF upper limit of around 0.4 for pressure. An important quantity in this regard is the Courant number which gives the approximate number of cells the fluid passes through in one time-step. This is also referred to as the convective

Table 5.5: Critical fluid model solver settings for optimal convergence

PISO scheme settings	
Skewness Correction	0
Neighbour Correction	1
Skewness-Neighbour coupling	Off
Discretisation	
Pressure	2nd-order upwind
Momentum	2nd-order
Time	2nd-order implicit
Under-relaxation factors (Δt = 0.005s)	
Pressure	0.2
Momentum	0.467

Courant number which is calculated from

$$C_n = \frac{V_c \, \Delta t}{L_c}, \tag{5.5}$$

where V_c and L_c are the characteristic flow velocity and cell length respectively. The stability of a typical fluid solution is inversely proportional to the Courant number. For the final mesh and chosen time-step size the Courant number peaked at 3.8, 0.025s after the peak inlet flow rate occurs, while the maximum cell convective Courant number is 21.3. These values are more than adequate to ensure that the convergence rate is maintained to the required accuracy for typical flow problem.

To ensure that the model converges correctly for each time-step we monitored the scaled residuals (see Section 4.2.5), and the convergence of the velocity, pressure and WSS solutions over their respective domains. We note that the maximum values and integrals converged more than sufficiently if the scaled continuity residual (see Section 4.2.5) decreased to a value of 1×10^{-4}, hence this was chosen as the convergence criterion for our problem in both the fluid and FSI models. The residuals for the segregated x, y, and z momentum equations reduced to values between 1×10^{-5} and 1×10^{-6} at convergence, depending on the time-step size. With the optimal solver settings 44 iterations on average were required to converge within each time-step. A single cardiac cycle (pulse) requires less than 11 minutes to complete on an Intel®Xeon(R) E5 workstation with 16 cores (12 used) and 64 GB RAM.

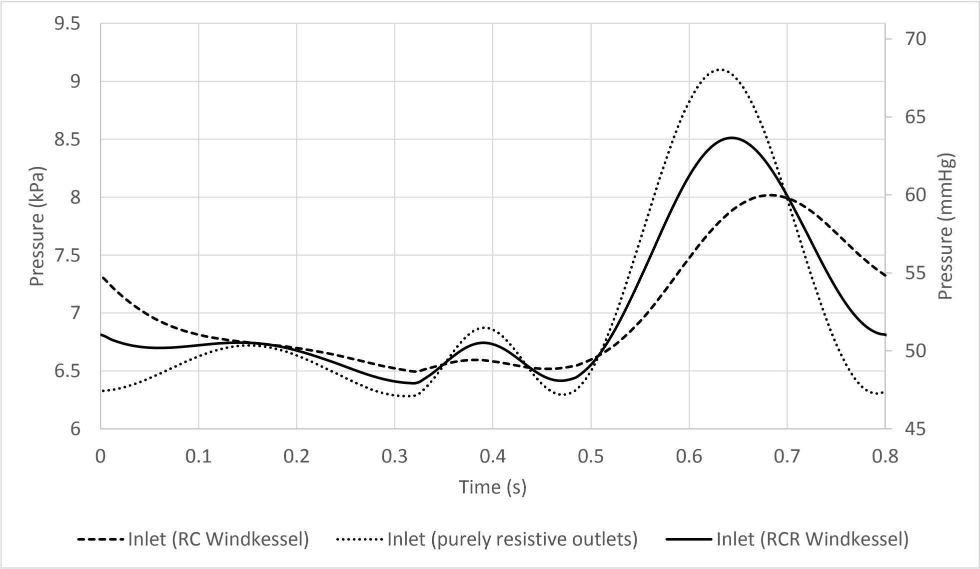

Figure 5.10: Pressure waveform solution plot at the inlet of each fluid model

Periodicity of the solutions to the velocity, pressure and WSS were all verified to have an error inferior to 1 %. The fluid models all reached sufficient periodicity within the second cardiac-cycle. The approximate points at which the fluid models became periodic was at 60 ,50 , and 80 % through the second pulse for the purely resistive outlet model, the RC Windkessel model, and the RCR Windkessel models, respectively. The results discussed below are those of the third cardiac-cycle simulated by each of the three fluid models.

The inlet pressure waveform solution at the inlet to each of the three fluid models is shown in Figure 5.10. The purely resistive outlet fluid model has a pressure wave that is exactly in phase with the inlet flow rate waveform, as expected. The RCR Windkessel fluid model solution has a smaller range of pressures throughout the pulse, as well as a small lag to the peak pressure. The solution to the RC Windkessel model solution has the smallest range of pressures, the greatest waveform lag and much of the detail of the profile is lost.

The average velocity waveform solutions at each of the outlets of the three models are plotted in Figure 5.11. In contrast to the pressure waveforms, there is very little lag difference between the velocity waveforms. Although there is not a great difference in average velocity between the artery and vein outlets in each model, the flow rate split remains close to a 30 %-70 % split in each.

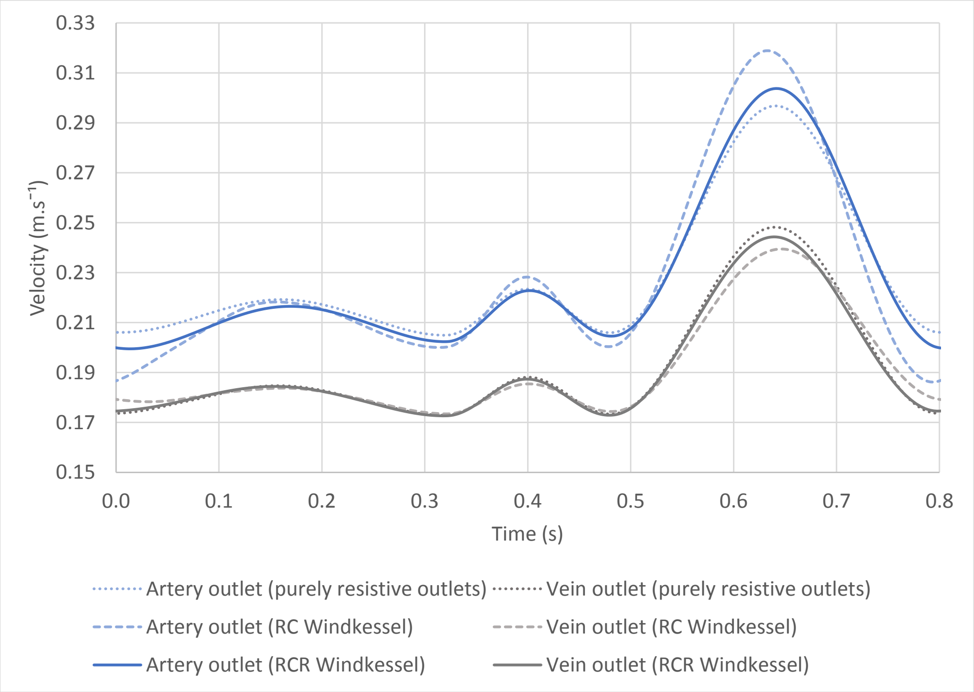

Figure 5.11: Average velocity waveform solutions at the outlets to the fluid models

5.2.5 Mesh convergence analysis

A mesh refinement analysis is carried out to make certain that the solution is mesh-independent and to find an optimal mesh choice for efficiency while achieving the required accuracy. The latter is determined by finding at which point the mesh is sufficiently fine; that is, where further refinement leads to negligible improvement. Since the solid and fluid meshes are conformal at the FSI boundary (see Section 5.3.1), this also serves to minimise the size of the solid problem, provided that the solid mesh is also sufficiently fine (see Section 5.3.6).

Four meshes were created with the meshing blocking strategy described in Section 5.2.3, of varying cell density and with a varying number of boundary layer cells. The details of these meshes are shown in Table 5.6. Mesh independence was tested with a transient analyses with results captured and compared at the peak inlet flow rate ($t = 0.64\,\mathrm{s}$). The following integrated solution quantities were obtained; the pressure and the velocity throughout the domain, and the WSS on over the fluid wall (FSI boundary). The maximum velocity within the domain was also recorded for each of the meshes.

Table 5.6: Details of the four meshes created for the fluid convergence study

Mesh	Cells	Nodes	Bnd. layers	Cell size
Coarse	43224	47615	4	0.524 mm
Medium	187152	197618	7	0.321 mm
Fine	345792	362725	8	0.262 mm
Reference	1178928	1216925	16	0.174 mm

The relative error with respect to the highest density, the reference mesh, was calculated for each quantity for more dense meshes, the results are summarised in Table 5.7. The convergence rates are plotted in Figure 5.12 with a linear rate of convergence indicated by the dotted line. It is evident that the relative (approximate) error decreases at a linear rate and that a negligible error in the integral of the WSS (1 %) is obtained by the medium mesh.

The WSS solution error is greater relative to the rest of the solution quantities. Further testing showed that the number of boundary layers and the growth rate are especially important factors in the accuracy of the WSS. Images of the contours to the WSS solution are shown in Figure 5.13, these show qualitatively the trend in the model's

Table 5.7: Solution errors to the fluid convergence study

	Pressure integral (Pa m^3)		WSS integral (Pa m^2)	
Mesh	Result	Error	Result	Error
Coarse	4.161×10^1	0.99 %	9.592×10^{-3}	3.09 %
Medium	4.193×10^1	0.22 %	9.801×10^{-3}	0.97 %
Fine	4.195×10^1	0.18 %	9.826×10^{-3}	0.72 %
Reference	4.202×10^1	-	9.897×10^{-3}	-
	Velocity integral (m^4 s^{-1})		Maximum velocity (m s^{-1})	
Mesh	Result	Error	Result	Error
Coarse	1.804×10^{-3}	0.44 %	9.180×10^{-1}	0.30 %
Medium	1.808×10^{-3}	0.19 %	9.148×10^{-1}	0.06 %
Fine	1.809×10^{-3}	0.16 %	9.157×10^{-1}	0.04 %
Reference	1.812×10^{-3}	-	9.153×10^{-1}	-

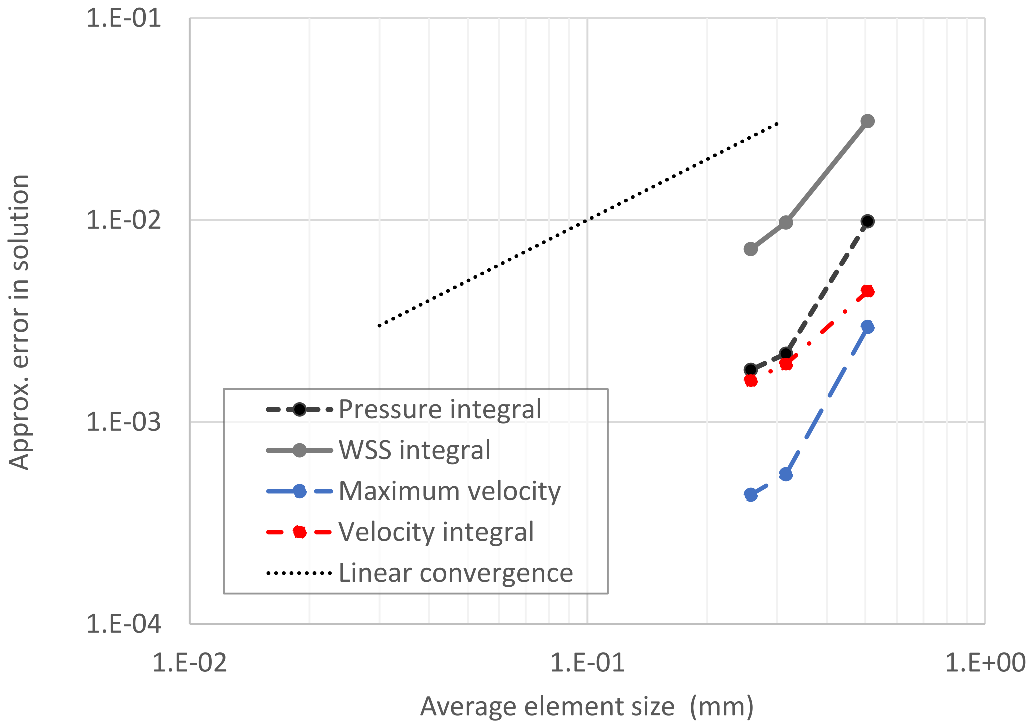

Figure 5.12: Plots of the convergence rates of fluid solutions during mesh refinement

ability to pick up the WSS concentration at the anastomosis as the mesh is refined. One can see that medium mesh in Figure 5.13(c) identifies the WSS concentration relatively accurately while the coarse does not.

The pressure solution on the boundary of the domain at the anastomosis is shown in 5.14, where the scale of pressures run from 8600 to 9000 Pa. It is clear that the pressure distribution is solved for accurately by the medium and fine mesh but not by the coarse mesh. The medium mesh was chosen to model the fluid in this section as well as in the final FSI model (see Section 5.4) since it is sufficiently accurate quantitatively and qualitatively. The conformal solid mesh is determined to be mesh-independent and sufficiently accurate as demonstrated in Section 5.3.6.

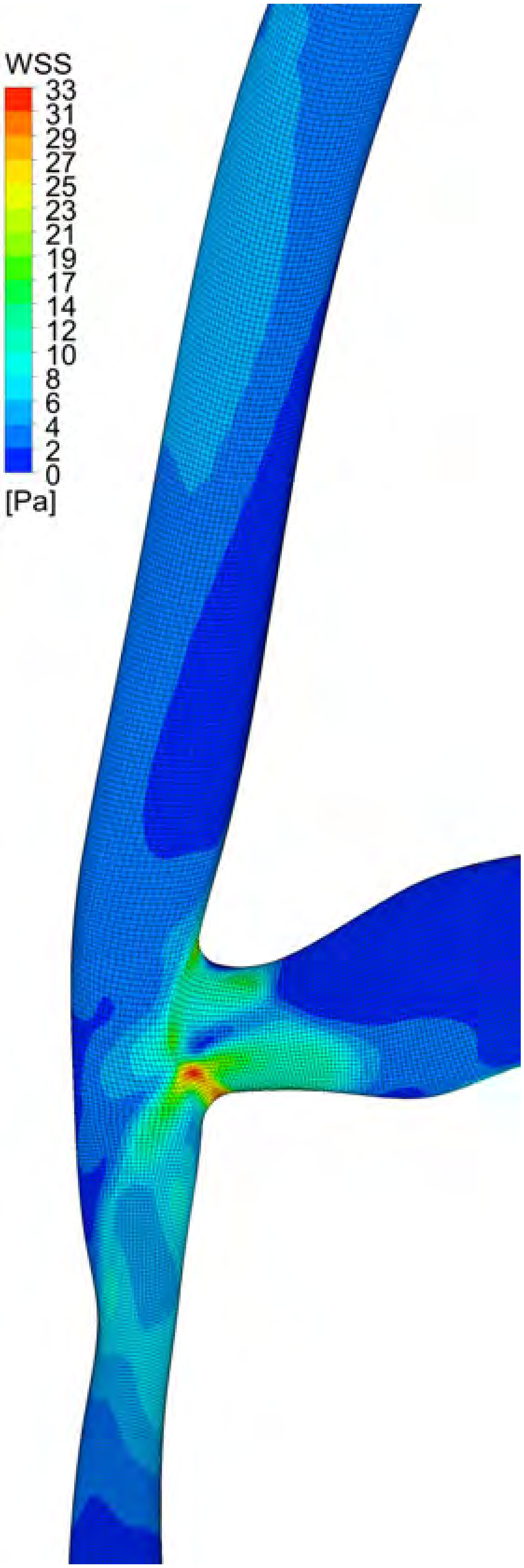

(a) Reference mesh

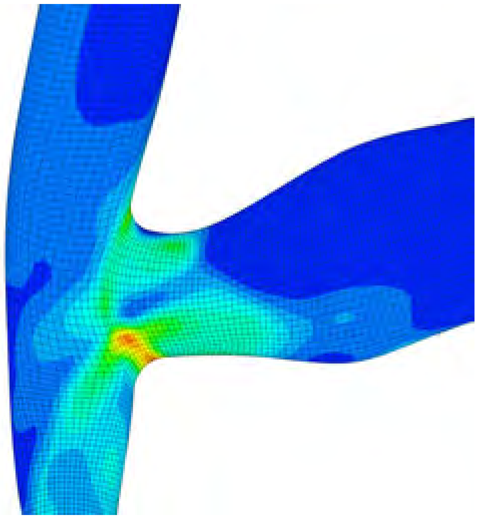

(b) Fine mesh

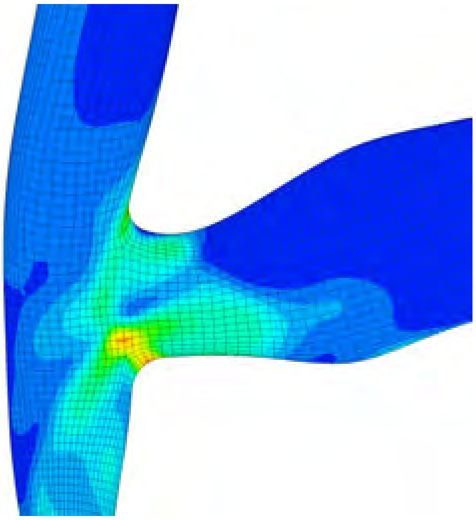

(c) Medium mesh

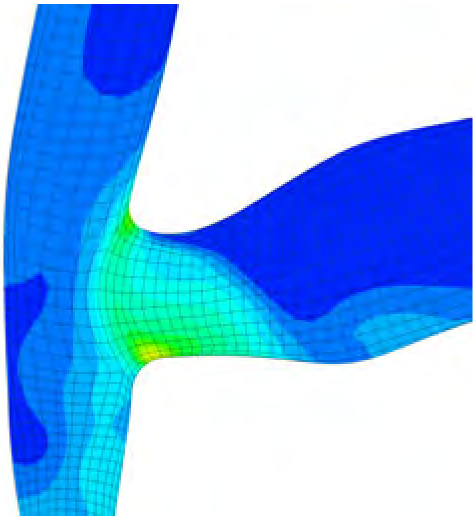

(d) Coarse mesh

Figure 5.13: Comparison of the WSS solutions at the anastomosis between the high medium and low density meshes

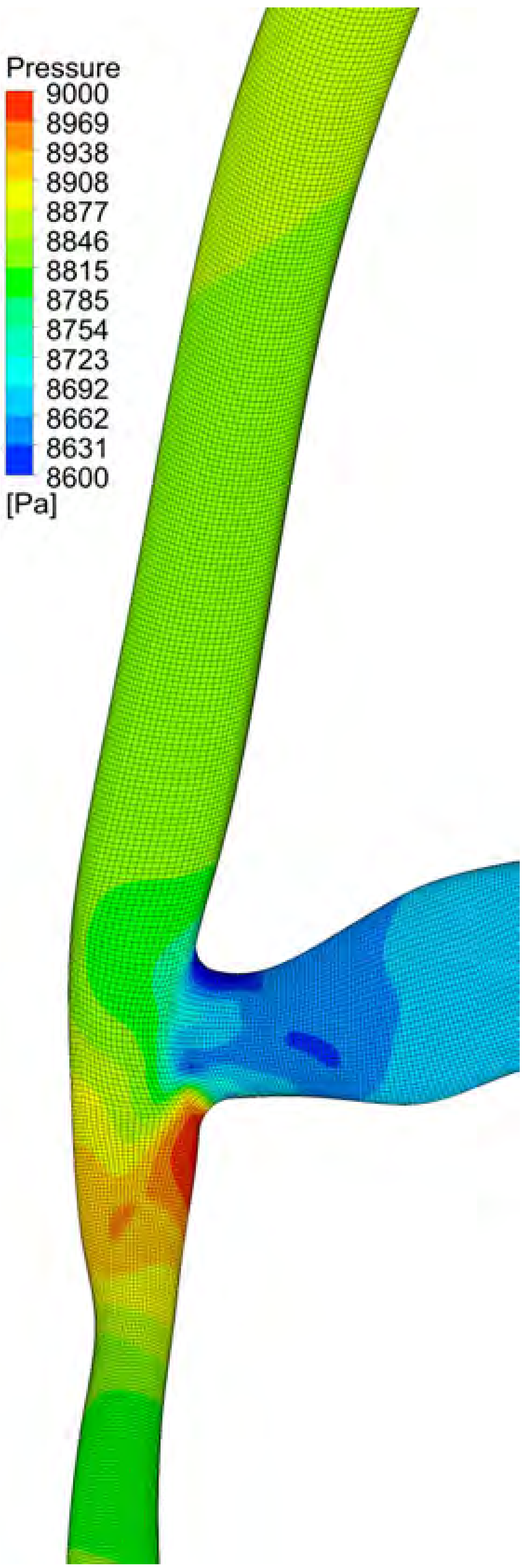

(a) Reference mesh

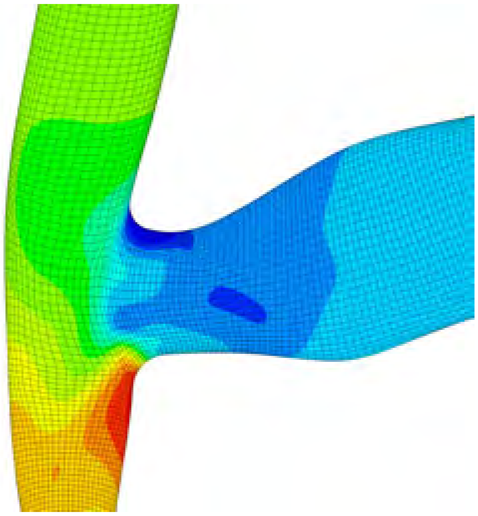

(b) Fine mesh

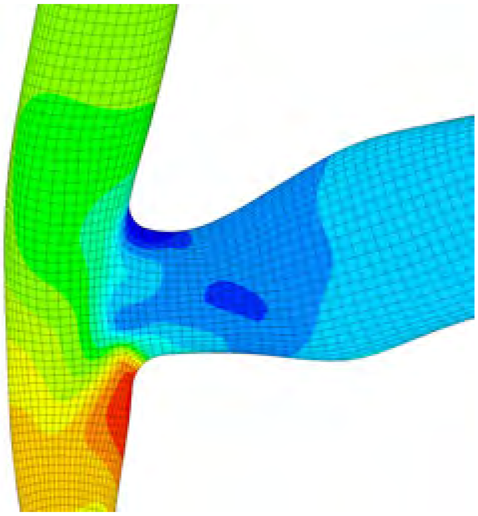

(c) Medium mesh

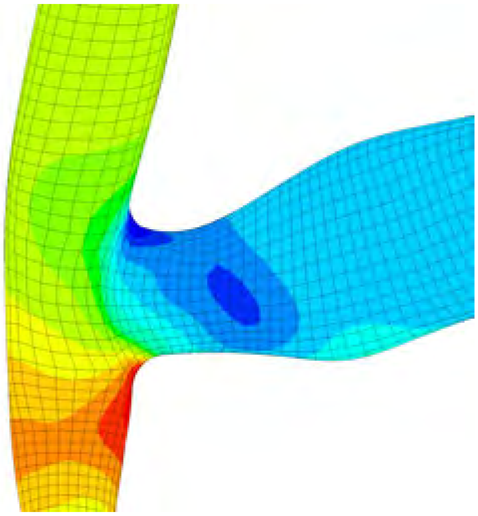

(d) Coarse mesh

Figure 5.14: Comparison of the pressure solutions at the anastomosis between the high medium and low density meshes

5.3 Patient-specific solid model

5.3.1 Geometry and mesh

The resolution used in the PC-MRA sequences is far too low to segment or even locate the vessel walls. As such, the thickness of the vein and artery cannot be determined from the MRI scan. It has thus been assumed that the vein has a constant thickness of 0.4 mm, a thickness typical for a cephalic vein prior to AVF creation [118]. The arterial thickness is set to 1/10th of the lumen diameter, the approximate ratio according to [119].

Shell elements can be used to generate an efficient solid model for an AVF with fewer degrees of freedom, as used in [66]. However, the use of shell elements requires the inlet and outlet extremities to be fixed in space, which is unphysical and likely to lead to significant error if the inlet and outlet lengths are short as in our model. A Robin BC is applied on the outer surfaces of the vessel walls to mimic the behaviour of the tissue surrounding the vessel walls. This constrains the model adequately while allowing it to deform more naturally. It would require a considerable number of additional DOF, and unnecessary computational expense, to model the surrounding tissue. At present a Robin BC cannot be applied to shell elements in ANSYS Mechanical software.

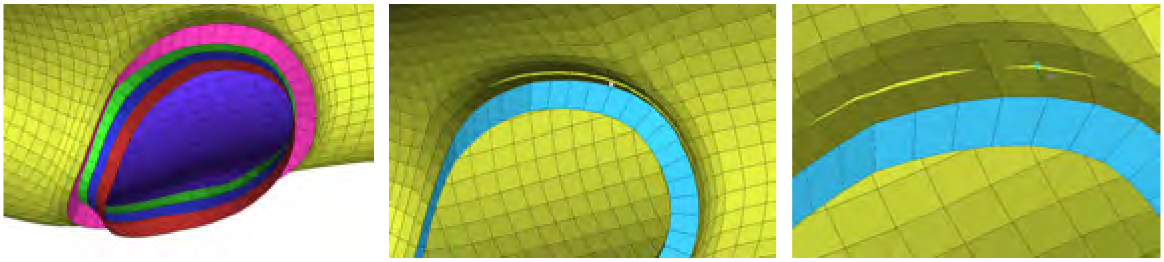
(a) (b) (c)

Figure 5.15: Generating the mesh and geometry in ICEM CFD: (a) boundary mesh sectioned at anastomosis - green, blue, and red sections, yellow and pink surfaces - artery, (b) sections extruded individually to create staggered taper, and (c) nodes joined at mid-point to create smooth taper.

To incorporate the Robin BC the fluid boundary mesh is extruded to generate the geometry of the vessel walls. The change in thickness between the artery and vein is applied by first extruding the vein and artery separately to their respective average thickness. The cells at the anastomosis are then tapered between the artery and vein manually in ICEM CFD. We were unable to automate this process, or join the artery and vein with a more natural curve, due to the complexity of the geometry.

To manually taper the mesh, the boundary mesh was first sectioned at the anastomosis as shown in Figure 5.15(a). Each section was then extruded separately to form a stepped taper. The fluid artery wall was extruded to form the artery vessel walls (yellow and pink faces). The narrow sections (green, blue, and red) are then extruded to form a stepped taper between the artery and vein. The first section (green) is extruded, as shown in Figure 5.15(b), and forms the arterial side of the anastomosis. The final smooth transition is formed by manually joining the relevant nodes at their mid-point as shown in Figure 5.15(c). An estimate had to be made as to where the artery and vein domains join; we have assumed here the two meet a third of the way down the taper from the artery (at the blue face).

5.3.2 Material model

The vessel walls are made up of a complex set of layers of tissue with helically distributed collagen fibres [120]. Increased tensile stress and deformation cause these fibres to reorientate in the direction of the principal strain so that the tensile strength of the vessel increases in this direction. Anisotropic hyperelastic material models are able to model this tissue and fibre behaviour. However, we were only able to apply this material model to perfectly cylindrical domains in ANSYS Mechanical software. It is currently not able adequately apply fibre orientations to a complex domain such as a patient specific fistula, though it is possible to do this loosely when combined with ANSYS® Composite PrepPost software. The viability or accuracy of this method was not tested.

We have assumed that the vessel walls follow the 3$^{\text{rd}}$-order Yeoh model described in Section 3.5.1. The mechanical properties are differentiated between the artery and vein. The material constants were obtained from [66] which have been determined form the experimental data of [121] for the venous tissue, and of [122, 123] for the arterial tissue, the latter having a larger compliance. The relationships between the stress and strain of each material model are shown in Figure 5.16.

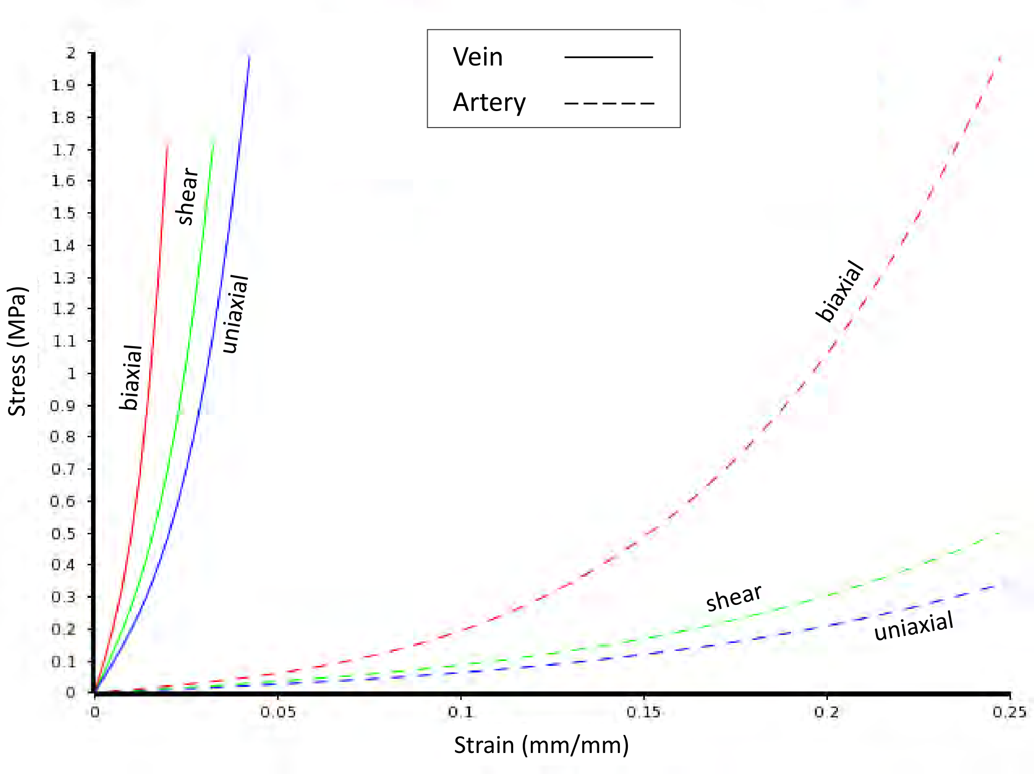

Figure 5.16: Artery and vein material stress-strain curves

5.3.3 Boundary and initial conditions

The model is constrained at the ends of the domain, at the inlet and outlet extremities by Dirichlet BCs, and on the outer surface of the solid domain by a Robin BC, as defined in Section 3.6.1. The inlet is fixed in place fully to aid in stabilising the final FSI model where the pressure, and pressure changes, are greatest. This BC has negligible effect on the overall solution, especially in the region of interest, since it is far from the anastomosis. At the outlets, nodes are prevented from displacing axially, but are free to translate parallel with the surface made by each outlet, this may be called a frictionless BC.

If the size of the domain was such that the inlet and outlets are all long, i.e. far enough from the region of interest, the extremities can all be made fixed without affecting the accuracy of the desired solution. However, this would require a greater number of DOF and increase the computational expense considerably, particularly in the respective FSI model. For this reason we have chosen to limit the length of the outlets and allow them to deform axially as is physically accurate.

No data is available on the typical stiffness characteristics of the tissue surrounding

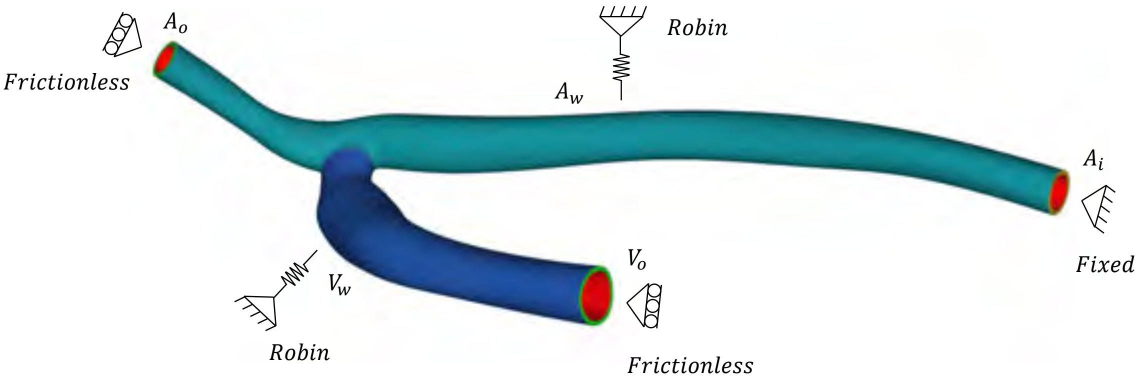

Figure 5.17: Solid model BCs. Robin BC at outer artery and vein walls (A_w and V_w). Frictionless BCs at the artery and vein outlet sections (A_o and V_o). Zero displacement BC at artery inlet (A_i). Pressure is applied on the inner FSI boundary of the artery and vein (red inner walls).

the veins and arteries in the upper arm. The Robin BC has thus been applied to constrain the model so that it does not deform excessively when the outlets are not held fixed, and also to test the numerical behaviour of the boundary condition in a biomechanical and FSI setting. The stiffness of the Robin BC was thus set at $k = 0.01\,\mathrm{N\,mm^{-3}}$ to constrain the model sufficiently but have negligible effect on the strain in the vessel walls. The set of BCs used in the final solid and FSI models are depicted in Figure 5.17. The artery inlet, outlet and outer walls are indicated by A_i, A_o, and A_w respectively, while the vein outlet and outer walls are indicated by V_o and V_w.

The forces exerted by the blood flow and pressure on the internal vessel walls in the fistula drive the solid model in the case of the FSI. We simulated this roughly by subjecting the internal surface of the solid domain to a constant pressure of 9100 Pa, the approximate peak pressure obtained from the fluid model (see Section 5.2.4). It is possible to apply a pressure BC from a fluid model solution with a one-way FSI simulation. This, however, would have required a fair amount of set-up time and limited the number of tests we could perform with the BCs and element formulations. While certainly not physically accurate, the variations in pressure on the boundary of the fluid are relatively small and gradual (see Figure 5.14). Thus, the behaviour, performance, and validity of the numerical model can still be tested with this approximation (see Section 5.3.6).

Robustness tests of the solid model with various configurations of BCs were also carried out. In each case fixed or sliding BCs were used at the inlets and outlets.

Models were also tested with the outer surface constrained with various Robin BC stiffnesses or with it left unconstrained. When the Robin BC stiffness is set too high the solution has difficulty converging or fails to converge at all (while the stiffnesses that produced credible deformations did not have convergence difficulties). All the inlet and outlet displacement-based BC configurations solved successfully with the inclusion of a Robin BC, this includes the least constrained configuration with only sliding BCs and the Robin BC. We were also able to successfully run a simulation with the inlet fixed, the outlets given sliding BCs, and the outer boundary completely unconstrained. The outcome of these tests demonstrate the robustness of the numerical scheme, and that any of these BC configurations are feasible for use in future work.

Considering initial conditions, it must be noted that cardiovascular vessels, such as those in vascular access, are in a stressed state due to the continuous pulsatile pressure generated by the heart. Likewise, the effects of prestressing have not been considered in the present study. Prestressing was not mentioned and is presumably not incorporated in the FSI project by Decorato et al. [66] (see Section 5.4.3).

5.3.4 Element formulations

We examined the performance of a number of element types and formulations in modelling the vessel walls. All elements used a mixed displacement-pressure formulation with hydrostatic pressure as the internal variable. The elements considered include the following:

- $Q'2$-P1 serendipity 20 noded hexahedral with a further 2 internal nodes and 4 pressure DOF.
- Q1-P0 hexahedral with 1 pressure DOF and selective reduced integration (SRI) where shear strains or volumetric strains are evaluated in the element midpoint only.
- Q1-P1 hexahedral with the enhanced strain formulation (ESF) with 4 pressure DOF and a further 9 enhanced strain DOF.

These elements are designed to handle the incompressibility constraint as described in Section 3.5.1 and hence circumvent problems associated with volumetric locking.

The enhanced assumed strain element is also designed to deal with bending dominated problems as described in Section 4.1.3. The $Q'2$-P1 element produced negligibly different results when using full integration or uniform reduced integration (URI), however we chose to use the latter method as it was marginally more efficient in our case.

The use of the higher-order $Q'2$-P1 serendipity element produced the most accurate results. However, the addition of the mid-side nodes on the edges of the element meant that the fluid and solid meshes would not be conformal at the FSI boundary. A further drawback to using higher-order elements is the additional computational expense required for the extra displacement DOF.

Earlier tests were also carried out with two types of tetrahedral elements. A higher-order tetrahedral (P2-P0) element with one hydrostatic pressure DOF and a the lower-order tetrahedral (P1-P1) element with hydrostatic pressure introduced by an additional DOF at each node. The P1-P1 element uses a stabilised pressure formulation. These tetrahedral elements performed poorly compared with the hexahedral elements; to achieve the comparable accuracy a far greater number of DOF were required for the P2-P1 elements while the P1-P1 elements performed poorly regardless.

5.3.5 Solution method

The solution procedure occurs in two stages to first speed up the solution process in stage 1 and then to mimic to some degree the transient behaviour in stage 2. In the first stage the pressure BC is applied at 9000 Pa with a time-step size of 1s so that the model acts as if it is being increased in pressure from 0 to 9000 Pa over this duration. A time-step size of 0.005s is then used in the subsequent time-step to increase the internal pressure to its maximum value of 9100 Pa.

A direct solver with a full Newton-Raphson method is used to iterate toward the solution (an iterative solver cannot be used with the mixed displacement-pressure formulation in ANSYS Mechanical software). Line search and stabilisation methods were not required to converge. It was found that it was unnecessary to use multiple substeps to ramp the pressure BC in each time-step. This only lengthened the solution time showing that Newton iterations alone were enough to converge efficiently to the solution at each stage.

5.3.6 Mesh and convergence analysis

As in Section 5.2.5, we investigate the effect of mesh density and mesh structure on the solution to show that it is mesh-independent and to find an optimal mesh to use for the FSI model. Additionally, this has been done with each of the element types described in the preceding section to compare their relative accuracy and efficiency.

We carried out two mesh convergence studies since having to manually taper and join nodes for high density meshes would take far too long. An extensive convergence analysis was therefore performed on four underlying meshes where the vein are walls assumed to have the same thickness dimension as the artery, these could be meshed far more quickly. This allowed us to carry out a complete analysis in a reasonable time. A smaller convergence analysis was then carried out with the tapered mesh geometries for two underlying meshes.

For each mesh, mid-side nodes could simply be added to the lower-order element mesh to create the higher-order element meshes. Each element type is tested with a mesh that has one, two, three, and four layers of elements through the thickness of the vessel walls. The meshes were refined in this way as multiple layers of 3D elements are required in bending dominated problems to alleviate locking in extreme cases.

Initial mesh convergence analysis

The first convergence study was carried out with a Robin BC stiffness of $0.02\,\mathrm{N\,mm^{-3}}$. We found that this stiffness was too restrictive and decreased this to $0.01\,\mathrm{N\,mm^{-3}}$ for the smaller convergence study, and for the final FSI model. The details of the meshes, as well as the results, of the larger convergence study are summarised in Table 5.8.

The simulations for these models were performed on Intel®Core(TM) i7 workstation with 4 cores and 16 GB RAM. The reference mesh model was too large a problem for this workstation, this was solved with an Intel®Xeon(R) E5 workstation with 16 cores (4 used) and 64 GB RAM.

The error in the solution, relative to the reference model solution, is calculated for the strain energy, L2-norm, maximum deformation, maximum principal strain, and the maximum shear strain (see Table 5.8). The errors in the L2-norm are plotted on a

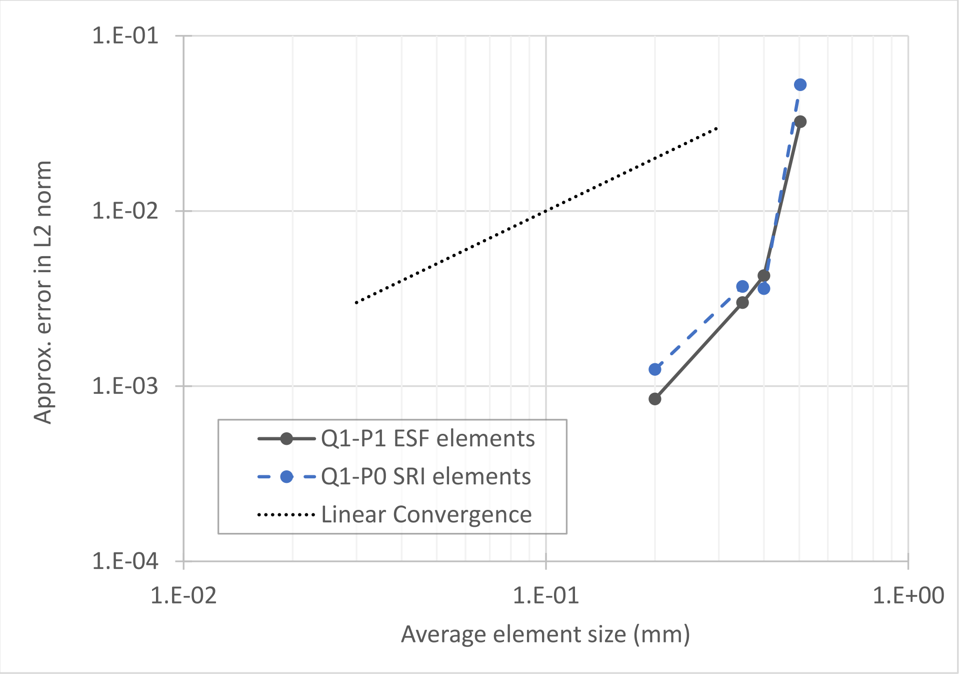

Figure 5.18: Convergence plot of the error in the L2-norm with mesh refinement (initial mesh convergence analysis)

Table 5.8: Details and results of the large mesh convergence study

	Element type	**Q1-P1 ESF**				**Q1-P0 SRI**				**Q'2-P1 URI**			
	Element layers	**1**	**2**	**3**	**4**	**1**	**2**	**3**	**4**	**1**	**2**	**3**	**4**
	No. of elements	15744	31488	47232	251904	15744	31488	47232	251904	15744	31488	47232	251904
	Ave. elem. size (m^3)	1.28E-10	6.38E-11	4.25E-11	7.98E-12	1.28E-10	6.38E-11	4.25E-11	7.98E-12	1.28E-10	6.38E-11	4.25E-11	7.98E-12
	No. of dof	94890	142335	189780	946785	94890	142335	189780	946785	331695	521265	710835	3595653
	No. eqns. Solved	157194	267279	377364	1951041	109962	172815	235668	1195329	392991	644529	896067	4593861
	Calc. time (s)	23.8	39.8	53.2	2065.3	23.3	43.7	63.3	1046.2	55.8	142.6	425.2	n/a
	Relative calc. time	0.01	0.02	0.03	1.00	0.01	0.02	0.03	0.51	0.03	0.07	0.21	n/a
Strain Energy	**Value (J)**	2.208E-03	2.222E-03	2.226E-03	2.227E-03	2.254E-03	2.231E-03	2.228E-03	2.229E-03	2.231E-03	2.230E-03	2.230E-03	2.230E-03
	Error (%)	0.97%	0.34%	0.17%	0.14%	1.10%	0.07%	0.09%	0.02%	0.07%	0.02%	0.02%	0.00%
L2Norm	**Value**	3.461E-07	3.339E-07	3.343E-07	3.350E-07	3.529E-07	3.365E-07	3.340E-07	3.357E-07	3.346E-07	3.346E-07	3.346E-07	3.353E-07
	Error (%)	3.24%	0.43%	0.30%	0.08%	5.24%	0.36%	0.37%	0.12%	0.19%	0.19%	0.22%	0.00%
Max Def	**Value (m)**	5.777E-04	5.766E-04	5.773E-04	5.770E-04	6.421E-04	5.896E-04	5.812E-04	5.803E-04	5.777E-04	5.779E-04	5.777E-04	5.776E-04
	Error (%)	0.03%	0.17%	0.04%	0.10%	11.18%	2.09%	0.64%	0.47%	0.02%	0.05%	0.03%	0.00%
Max principal strain	**Value (m/m)**	0.098	0.109	0.117	0.127	0.118	0.108	0.114	0.125	0.167	0.137	0.146	0.143
	Error (%)	31.26%	23.78%	18.41%	11.50%	17.45%	24.36%	20.26%	12.60%	16.35%	4.41%	1.90%	0.00%
Max shear strain	**Value (m/m)**	0.193	0.222	0.238	0.256	0.212	0.212	0.226	0.244	0.241	0.247	0.259	0.268
	Error (%)	28.16%	17.28%	11.34%	4.42%	20.96%	21.09%	15.62%	9.06%	10.19%	7.75%	3.52%	0.00%

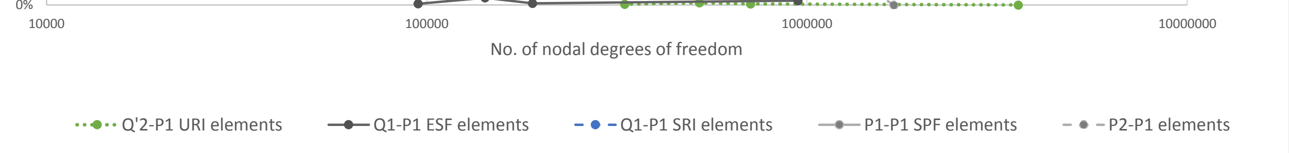

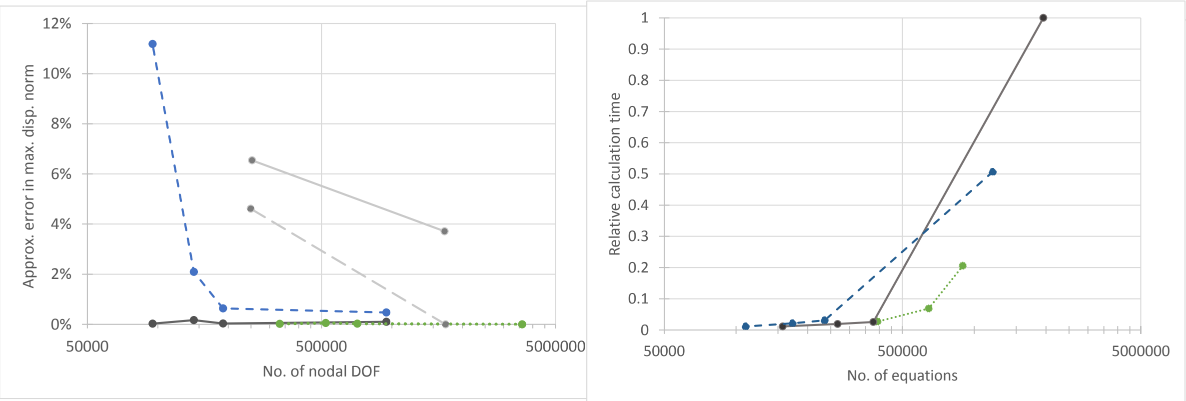

(a) Max. disp. norm error

(b) Relative calculation time

Figure 5.19: Plots of the displacement convergence and relative calculation times of the initial mesh convergence analysis

log-log scale in Figure 5.18 for the lower-order elements, the overall convergence rate is linear for both formulations as indicated by the dotted line. The error in the L2-norm drops below 1% for both formulations when two or more element layers are used. The Q1-P1 ESF elements seem to perform slightly better than the Q1-P0 SRI elements when the mesh with one layer of elements is used with a 3% error in the L2-norm compared with a 5% error in the case of the latter.

The errors in the maximum displacement norm of the solution is plotted in Figure 5.19(a). The results to the tests performed on the tetrahedral elements are also plotted in Figure 5.19(a) and 5.19(b) (see Section 5.3.4).In this case the Q1-P1 ESF elements outperform the Q1-P0 element by far when one layer is used, with an error less than 1% for the former and more than 11% for the latter. It is interesting to note that the Q1-P1 ESF model solves as efficiently as the Q1-P0 SRI model for one layer of elements and more efficiently for two or three element layers, though the number of equations solved is greater (see Figure 5.19(b)). This trend does not continue, however, as the enhanced strain formulation takes twice as long to solve for the densest mesh. Note that the graphs in Figure 5.19 have been plotted on a semi-log scale so that results for the Q′2-P1 URI element meshes can also be shown. One can also see that qualitatively the Q1-P1 ESF element outperforms the Q1-P0 element in Figure 5.20.

As shown in Figure 5.21(a) the convergence rate of the maximum principal strain is

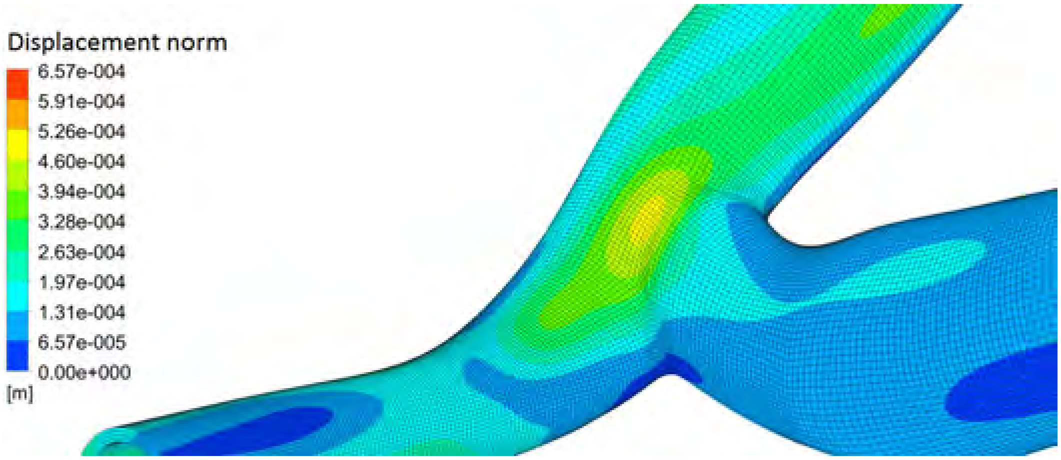

(a) Four layer, high node density, $Q'2$-P1 URI mesh

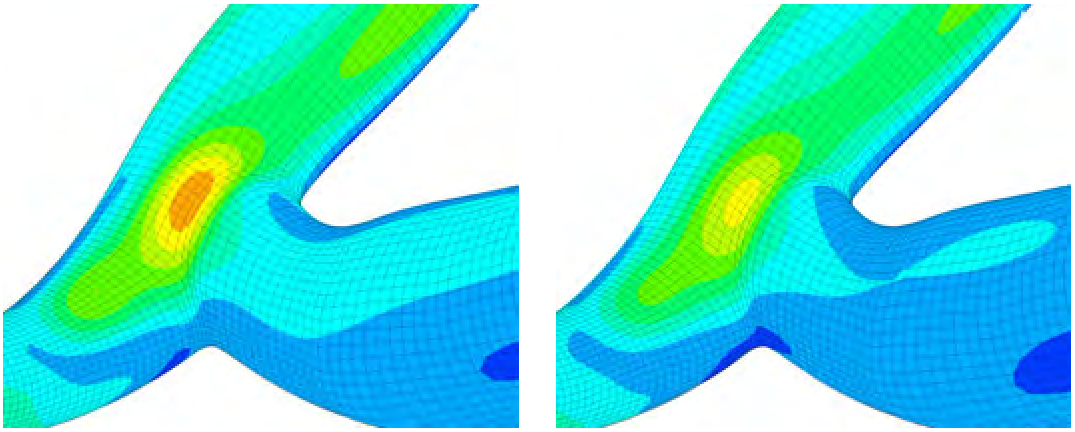

(b) One layer Q1-P0 SRI mesh

(c) One layer Q1-P1 ESF mesh

Figure 5.20: Comparison of the displacement norm solution contours on the outer boundary of the artery-vein anastomosis (Initial mesh convergence study)

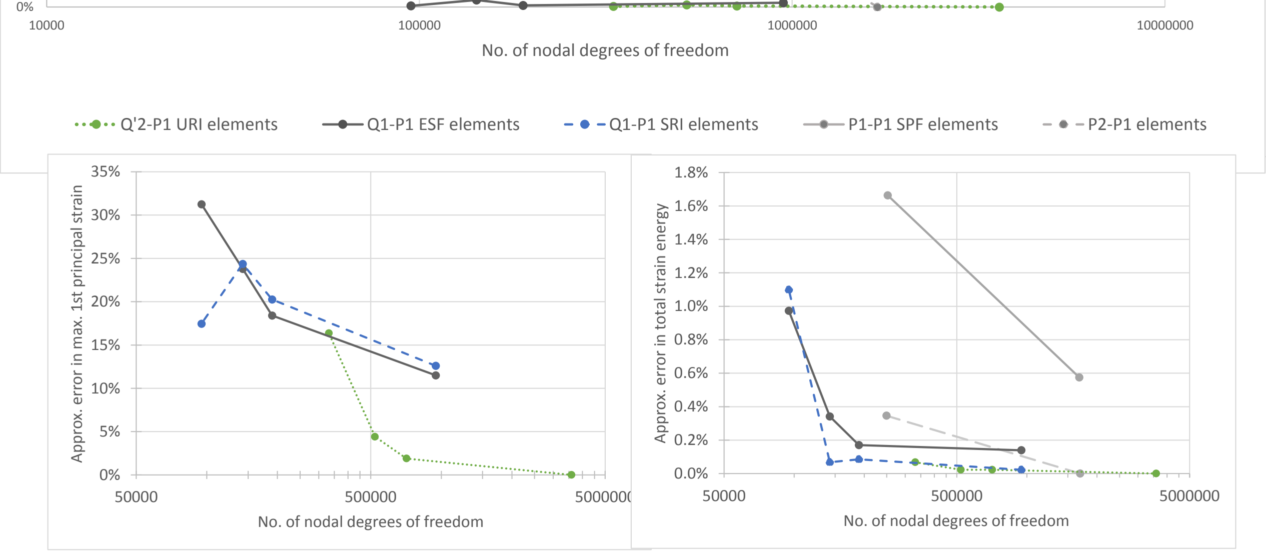

(a) Error in maximum principal strain

(b) Error in total strain energy

Figure 5.21: Graphs of the mesh convergence behaviour of various element types for the patient-specific solid model where the artery and vein are assumed to both have a thickness of 0.6mm.

far slower. This is due to a form of stress concentration near the anastomosis that can be seen in Figure 5.22. From a qualitative perspective, however, the overall strain solution of both one-layer models are relatively accurate, although the enhanced strain formulation model appears to do slightly better. The trends in the strain energy error behaviour are very similar for each element type and show a negligible error of 1% for the single layered meshes (see Figure 5.21(b)).

Secondary mesh convergence analysis

The secondary convergence analysis uses the final patient-specific geometry with the tapered anastomosis and a Robin BC stiffness of $0.01\,\mathrm{N\,mm^{-3}}$. The details of the meshes and the results of this secondary convergence study are summarised in Table 5.9. Again the reference mesh for the error analysis is on the far right of the table, the highest density Q′2-P1 mesh, this time with two layers of elements through the thickness.

The errors in the L2-norm are plotted on a log-log scale in Figure 5.23 for the lower-order elements. In this analysis the error in the L2-norm is inferior to 1 % for the 1 layer Q1-P1 ESF mesh while the Q1-P0 formulation maintains its error of just above 5 % for the same mesh. The accuracy of the displacement solution is for the enhanced strain results for the single layered mesh could be due to the decreased stiffness in the

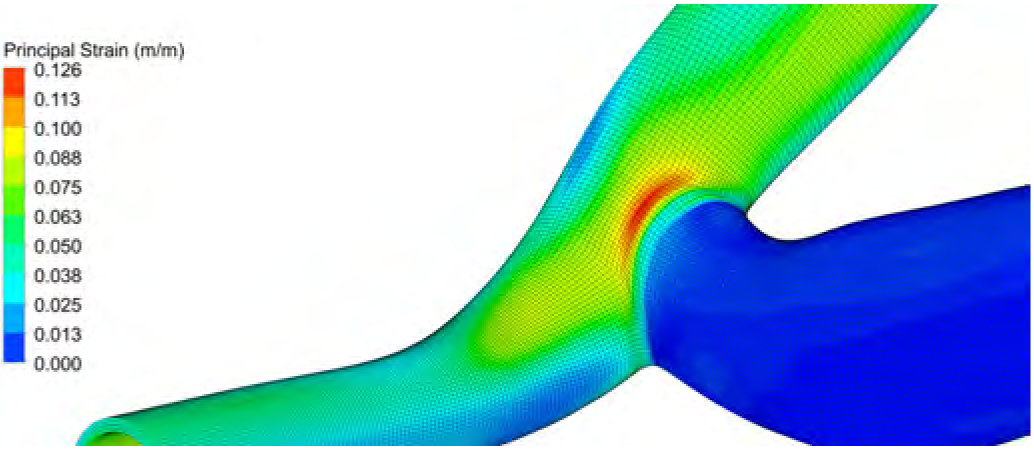

(a) Four layer, high node density, Q′2-P1 URI mesh

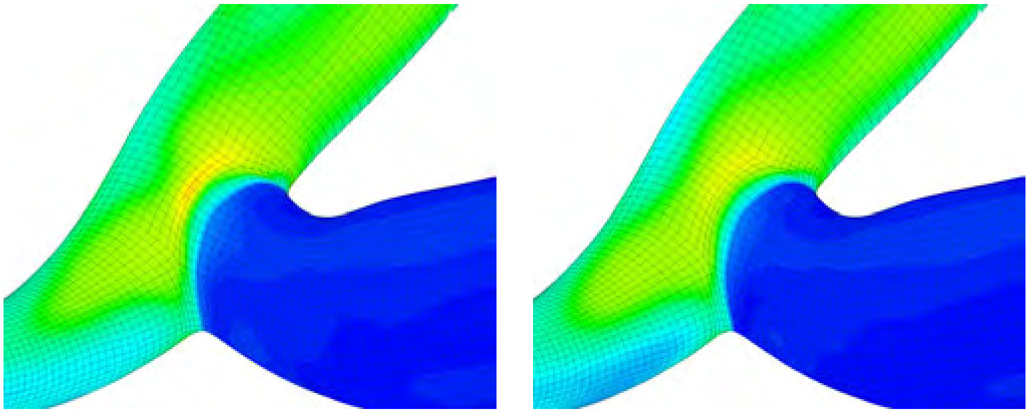

(b) One layer Q1-P0 SRI mesh

(c) One layer Q1-P1 ESF mesh

Figure 5.22: Comparison of the maximum principal strain solution contours on the outer boundary of the artery-vein anastomosis (actual geometry mesh convergence study).

Table 5.9: Details and results of the actual geometry mesh convergence study

	Element type	**Q1-P1 ESF**		**Q1-P0 SRI**		**Q'2-P1 URI**	
	Element layers	**1**	**2**	**1**	**2**	**1**	**2**
	No. of elements	15744	31488	15744	31488	15744	31488
	Ave. elem. size (m^3)	1.28E-10	6.38E-11	1.28E-10	6.38E-11	1.28E-10	6.38E-11
	No. of dof	47232	94464	47232	94464	47232	94464
	No. eqns. Solved	157386	267567	110154	173103	393471	645297
	Calc. time (s)	24	48	29	40	68	301
	Relative calc. time	0.08	0.16	0.10	0.13	0.22	1.00
Strain Energy	**Value (J)**	2.256E-03	2.270E-03	2.294E-03	2.277E-03	2.279E-03	2.278E-03
	Error (%)	0.96%	0.32%	0.71%	0.00%	0.05%	0.00%
L2Norm	**Value**	3.840E-07	3.847E-07	4.067E-07	3.857E-07	3.858E-07	3.853E-07
	Error (%)	0.3%	0.2%	5.6%	0.1%	0.1%	0.0%
Max Def	**Value (m)**	6.566E-04	6.418E-04	7.562E-04	6.420E-04	6.501E-04	6.517E-04
	Error (%)	0.74%	1.52%	16.03%	1.50%	0.25%	0.00%
Max principal strain	**Value (m/m)**	0.1056	0.1137	0.1096	0.1124	0.1757	0.1450
	Error (%)	27.20%	21.58%	24.40%	22.48%	21.19%	0.00%
Max shear strain	**Value (m/m)**	0.2041	0.2296	0.2070	0.2184	0.2567	0.2558
	Error (%)	20.21%	10.25%	19.07%	14.60%	0.36%	0.00%

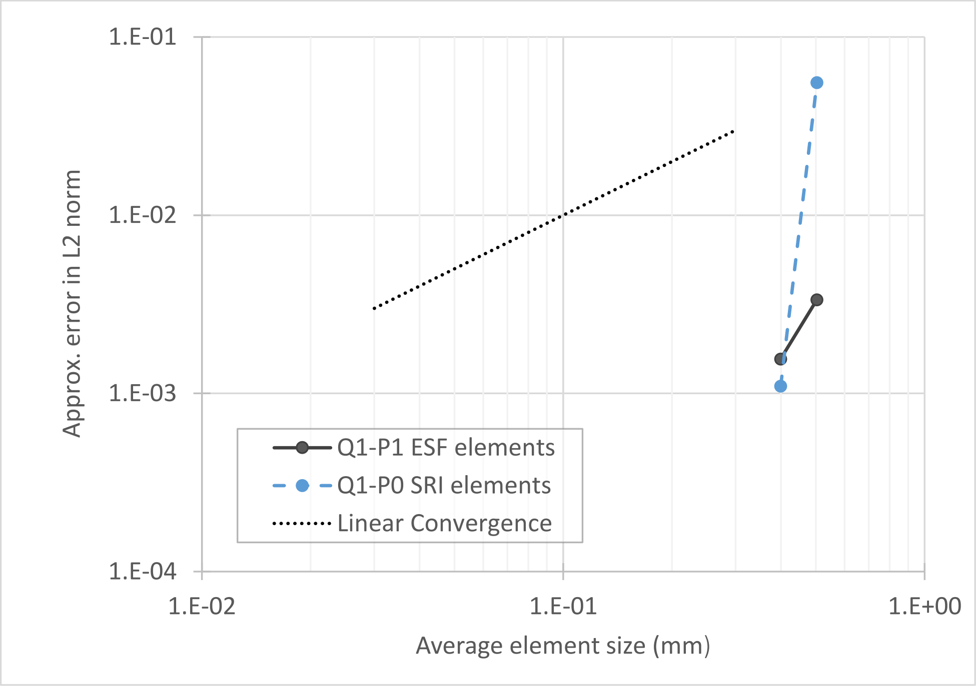

Figure 5.23: Actual geometry convergence plot of the error in the L2-norm with mesh refinement

Robin BC or as a result of the change in element sizes in the vein.

The enhanced strain single-layer mesh predicts the displacement solution more accurately than its counterpart, this can be seen qualitatively in Figure 5.24. Here, both double layered lower-order element meshes appear to behave similarly, although in terms of the L2-norm, the enhanced assumed strain elements do perform marginally better (see Table 5.9). The superior performance of the enhanced strain elements is highlighted if we look at the error in the maximum displacement solution, it is less than 1 % while the Q1-P0 SRI elements yield an error of 16 %.

The solutions obtained in both convergence studies show that as the number of DOF are increased each model converges. The effectiveness of the enhanced strain formulation in solving the displacement solution is clear; this element formulation provides the best trade off between efficiency and solution accuracy except in the case of the reference mesh. The enhanced assumed strain formulation is able to capture the displacement solution with sufficient accuracy with the single-layer mesh. This combination of mesh and element formulation minimises the computational expense of the solid model.

The importance of the FSI model is in the accuracy of the fluid solution. The solid

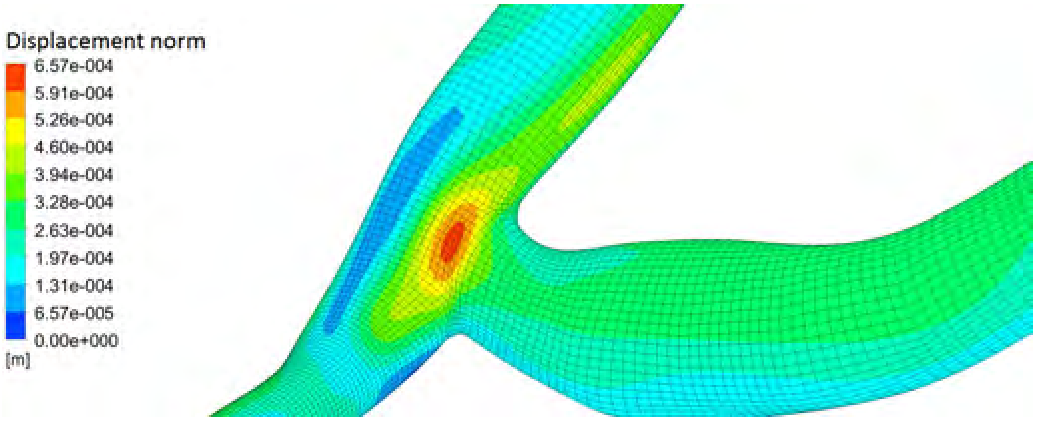

(a) Two layer $Q'2$-P1 URI mesh

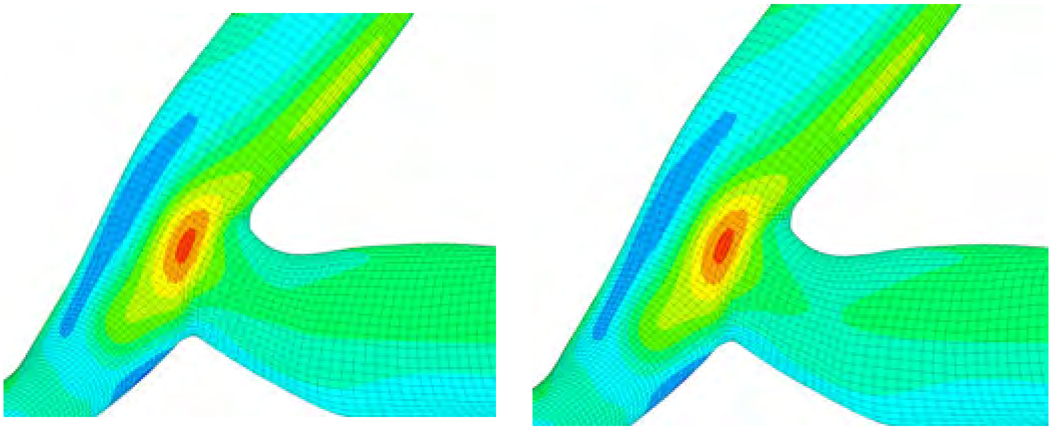

(b) Two layer Q1-P1 ESF mesh

(c) Two layer Q1-P0 SRI mesh

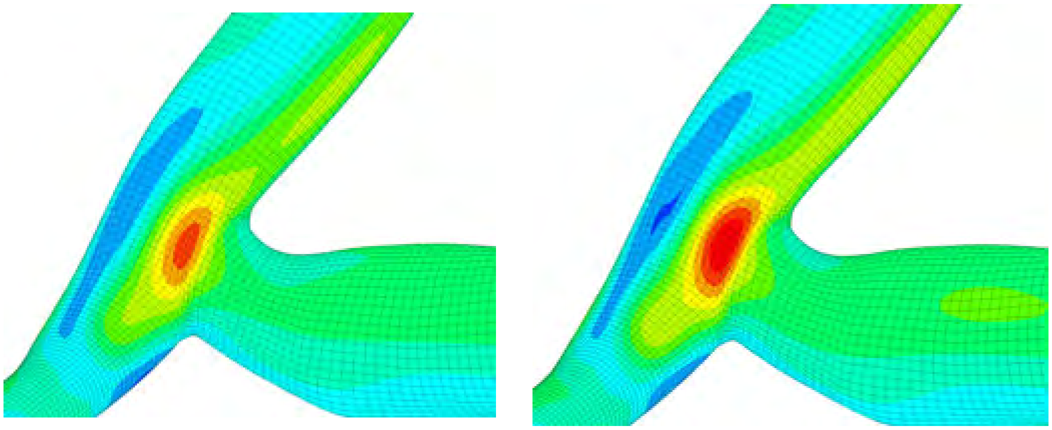

(d) One layer Q1-P1 ESF mesh

(e) One layer Q1-P0 SRI mesh

Figure 5.24: Comparison of the displacement norm solution contours on the outer boundary of the artery-vein anastomosis for the final solid mesh convergence and performance study.

model enhances the accuracy of the fluid solution by taking the deformation of the vessel walls into account. The stress and strain solution accuracy is not essential provided that the displacement solution is accurate. We have thus chosen to use the single-element layer mesh with the enhanced assumed strain formulation elements to model the solid for the FSI model. This reduces the computational expense considerably compared to using the alternatives, the single layered Q$'$2-P1 SRI mesh and the double layered meshes of each element type.

If a highly accurate stress-strain solution is required for a model such as ours at least three or four layers of elements should be used through the thickness of the walls. It would also be advisable to use higher-order elements for such a model as this has been shown to provide superior accuracy for a comparable computational expense. An FSI model using a mesh such as this would take far longer to complete than the model we have developed.

5.4 The patient-specific FSI model

5.4.1 Boundary and initial conditions

The BCs imposed on the fluid and solid models for the FSI case are the same as those described for the RCR Windkessel fluid model in Section 5.2.2, and the solid model in Section 5.3.3, excluding the BC prescribed at the FSI boundary in each model. The fluid model pressure solution at the FSI boundary is applied as a BC to the solid model while the fluid model FSI boundary is displaced according to the solid model displacement solution at the FSI boundary; this occurs in each coupling step (CS) as described in Section 4.3.1. The FSI boundary in the fluid model remains a no-slip BC, and its deformation induces fluid mesh motion (adaption) as described in Sec. 4.3.2.

5.4.2 Numerical set-up and behaviour

In this section we note a few of the adjustments that are required to run, stabilise, and optimise an FSI simulation. We remark on a few of the key distinguishing features in modelling the FSI by a staggered approach when an iterative fluid solver is used.

The unstable, overdamped and optimally stabilised behaviour of the fluid and solid solutions to our FSI model are then shown. Finally, the settings that optimise the FSI model are explained and summarised.

The staggered FSI algorithm we have used follows the approach described in Section 4.3.1.Mesh smoothing is required for movement of the fluid domain induced by the solid deformation. A number of mesh smoothing methods exist to cater for various forms of mesh motion. The "spring-based smoothing" method, described in Section 4.3.2, is a very efficient mesh smoothing technique which maintained the initial fluid mesh quality throughout the simulation. An adjustment of the "Laplace Node Relaxation" parameter was necessary to avoid cell deterioration however. the "linearly elastic solid-based" mesh smoothing method performed poorly in comparison while we were unable to achieve a stable FSI model with diffusion-based smoothing.

The spring-based method performs well for a tetrahedral mesh and when the the boundary deformation is largely orthogonal to that of the boundary surface itself, as it is in our case. The "Laplace node relaxation" parameter needs to be increased from its default value to 1 to ensure that the internal fluid mesh nodes follow the boundary nodes correctly. This ensures that cell inversion and solution divergence do not take place. It is expected that values below unity could be used as long as they are close enough to 1, this has not been tested however. The artery and vein outlet faces require a "dynamic mesh zone geometry" with a "faceted" definition for the mesh motion to function correctly.

The FSI is driven by the forces generated by the fluid model. Since the fluid solves iteratively the changes in forces that are sent to the solid can be controlled to a degree by only fractionally solving the fluid each coupling step. This is the mechanism by which the FSI model is stabilised. The solid model on the other hand converges fully (with a direct solver) each coupling step. The following simple changes to the FSI and fluid models have a stabilising effect on the FSI coupling:

- decreasing the number of fluid iterations per coupling step,
- decreasing the fluid URFs,
- increasing time-step size.

Increasing the time-step size can adversely affect to the convergence rate of the FSI

Table 5.10: Computational time per cardiac-cycle for the FSI model

Time-step size	No. of time-steps	Coupling iterations per time-step	Total CPU time per pulse
0.01 s	80	25	5.6 hrs
0.005 s	160	24	10.7 hrs
0.002 s	400	17	17.8 hrs

model however. This is as a result of the increased time-step size decreasing the rate of convergence of the fluid. This means that more fluid iterations can be taken each coupling step while maintaining the FSI coupling stability. However, more coupling steps will be required to converge to the fluid and overall FSI solutions (see Table 5.10). The effect is that the overall FSI convergence rate decreases if the time-step is increased.

Although the convergence rate of the FSI solution is negatively affected by an increased time-step size the overall computational expense is decreased since fewer time-steps need to be taken to complete a simulation. The time required to simulate a FSI simulation of a single cardiac-pulse for each time-step size is shown in shown in Table 5.10. This table also shows the number of coupling steps required to converge each time step and the number of time-steps required to complete a simulation of a cardiac-pulse. The computational time maintains a linear indirectly proportional relationship to the time-step size over the range of models tested. The FSI models were run on a Xeon(R) E5 workstation with 16 cores and 64 GB RAM, the fluid model was run on 12 of the cores and the solid on four.

When simulating the FSI with the 2 layered enhanced strain element mesh the computational time was doubled. This arose not only due to the increased number of solid model DOF but also because the solid model required two Newton iterations to converge each coupling step, in contrast to the single Newton iteration required by the smaller mesh.

We have found that the parameter that affects the FSI stability the most is the number of fluid iterations carried out each coupling step. The less the fluid solution converges each coupling step the more stable the FSI model is, this is easily achieved by carrying out fewer FIs per coupling step. Another method is to lower the fluid URFs, this however has less of an effect on stability, and the effect diminishes further as the URFs are lowered. Excessively lowering URFs is a very inefficient method in decreasing the rate of convergence and increasing the stability of the fluid.

The changes described above affect how much the fluid solution converges globally each coupling step. This is not optimal since the FSI instability is caused purely by the changes in the solution at the FSI boundary. The boundary source coefficient stabilisation method described in Section 4.3.3 slows the convergence rate primarily on the FSI boundary. This method increases the stability of the FSI coupling while the fluid convergence rate is not affected to the same degree as it is when URFs or number of fluid iterations are decreased.

In weakly-coupled FSI problems it is sometimes possible to achieve stability by ramping up the pressure solution that is transferred to the solid over a number of the coupling steps (as opposed to applying any of the changes above); this is implemented in the ANSYS Workbench software's System Coupling component. In strongly coupled problems, however, this will only delay the onset of the growth of the instability. Once the instability takes hold the solutions to both models oscillate with increasing degree until inversion of a cell or element occurs, causing the FSI simulation to fail (see Figure 5.25).

A combination of all of the above methods was required to optimally stabilise the model. The number of iterations needs to be decreased drastically, in our case to 4 iterations per time-step (down from the 44 iterations required for convergence in the fluid problem, see Section 5.2.4). The use of boundary source coefficient stabilisation negatively affected the stability of the fluid problem as it interacted badly with the Windkessel BCs on the fluid outlets. We were able however to use a larger amount of boundary stabilisation if the URFs were decreased. Lastly, we found that ramping the boundary solution transfer from the fluid for the first few iterations decreased the total number of coupling steps required to achieve FSI convergence. This is most likely the case because the iterative solution changes are drastic for the first few iterations, again largely due to the Windkessel BC, and the ramping ensures that the solid model does not follow closely these initial fluid solutions which have a stabilising effect.

To initially stabilise a staggered FSI model such as ours it is best to start by decreasing the number of fluid iterations to one or two and decrease the URFs as we have done by a half (from that of the fluid model). The number of fluid iterations can then be increased, until either the number of coupling steps start to increase, or if the model becomes unstable. Boundary stabilisation can then be applied and increased until the number of coupling steps is minimised. One may want to adjust each of these parameters slightly to attempt to further optimise the model. Lastly the total number of coupling steps can be reduced by one or two with the addition of pressure ramping over a number of the first few coupling steps.

The solution behaviour of our patient-specific FSI model, in unstable and overly stable (overdamped) states, is shown Figure 5.25. The maximum pressure on the FSI boundary in the fluid model is plotted against the coupling step number in Figure 5.25(a). The pressure is plotted for each fluid iteration so that one can see how the fluid progresses in the fluid model as well as the overall FSI model for two full time-steps. Four FIs have been used per coupling step for each time-step. Plotted in Figure 5.25(b) is the absolute value of the maximum displacement on the FSI boundary at the end of the coupling step. This is the maximum displacement that is transferred across the FSI boundary from the solid model to the fluid model.

In the first time step in Figure 5.25, the FSI model has been overdamped by applying too high a boundary source coefficient stabilisation to the fluid model. The initial wavelike behaviour of the pressure caused by excessive boundary stabilisation is also evident. Overdamping by other methods of stabilisation do not cause the same wavelike behaviour. On the other hand, too little stabilisation is used in the second time time-step so that the FSI model becomes increasingly unstable and eventually fails due to excessive mesh distortion. The individual coupling steps are now clearly visible in the second time-step; each oscillating maximum and minimum is the end of the last fluid iteration during that particular coupling step, and the start of the next coupling step. Notice that the model is initially stable due to the use of ramping in the first six coupling steps, before the ramping is complete; however, the model has already become unstable.

We were able to stabilise the added-mass effect for all the time-step sizes tested through the range $2 \times 10^{-2}\,\mathrm{s}$ to $1 \times 10^{-3}\,\mathrm{s}$. Decorato et al. [66] stated that they were unable to stabilise their FSI model for a time-step size of $2 \times 10^{-2}\,\mathrm{s}$. We believe this discrepancy could be due to the coupled pressure-velocity coupling scheme used in CFX and/or it could be as a result of the fact that they did not use boundary stabilisation in their FSI model. Only the changes to the URFs were mentioned in their work, the number of fluid iterations per coupling step was not mentioned, nor was boundary

Table 5.11: FSI settings for optimal efficiency with a time-step size of 0.005s

Stabilisation setting	Value
Pressure URF:	0.1
Momentum URF:	0.233
Boundary stabilisation method	Volume-based
Boundary stabilisation scale factor	200
No. of flu. iters per coup. iter.	4
No. of pressure ramping coup. iters	6

stabilisation.

The parameters that ensured optimal damping and simulation efficiency for a sufficiently small time-step size of 0.005 s are given in Table 5.11. The numerical behaviour of the maximum pressure and maximum displacement on the FSI boundary for the optimally damped model is shown in Figure 5.26. The results are shown and discussed in the next section.

5.4.3 FSI and fluid model results and analysis

The solutions to the average velocity at the outlets of the FSI and fluid models are plotted in Figure 5.29. The velocities are lower in both the artery and vein, although the difference is far greater in the artery. This is also evident in Figure 5.27 where the velocity streamlines at the anastomoses of the FSI and fluid are shown. This is as expected since the artery is more compliant than the vein.

The maximum deformation and principal strain in the artery are approximately 1.5 and 4 times greater than in the vein respectively. The plots of the maximum deformation and principal strains throughout the cardiac-cycle are plotted in Figure 5.28. Note that the velocities in the artery of the FSI model is lower than the respective velocity in the fluid model throughout the cardiac cycle. This should not be the case since the models are based on the same geometry and should agree at some stage of the cardiac-cycle. This is as a result of the large initial deformation in the FSI model

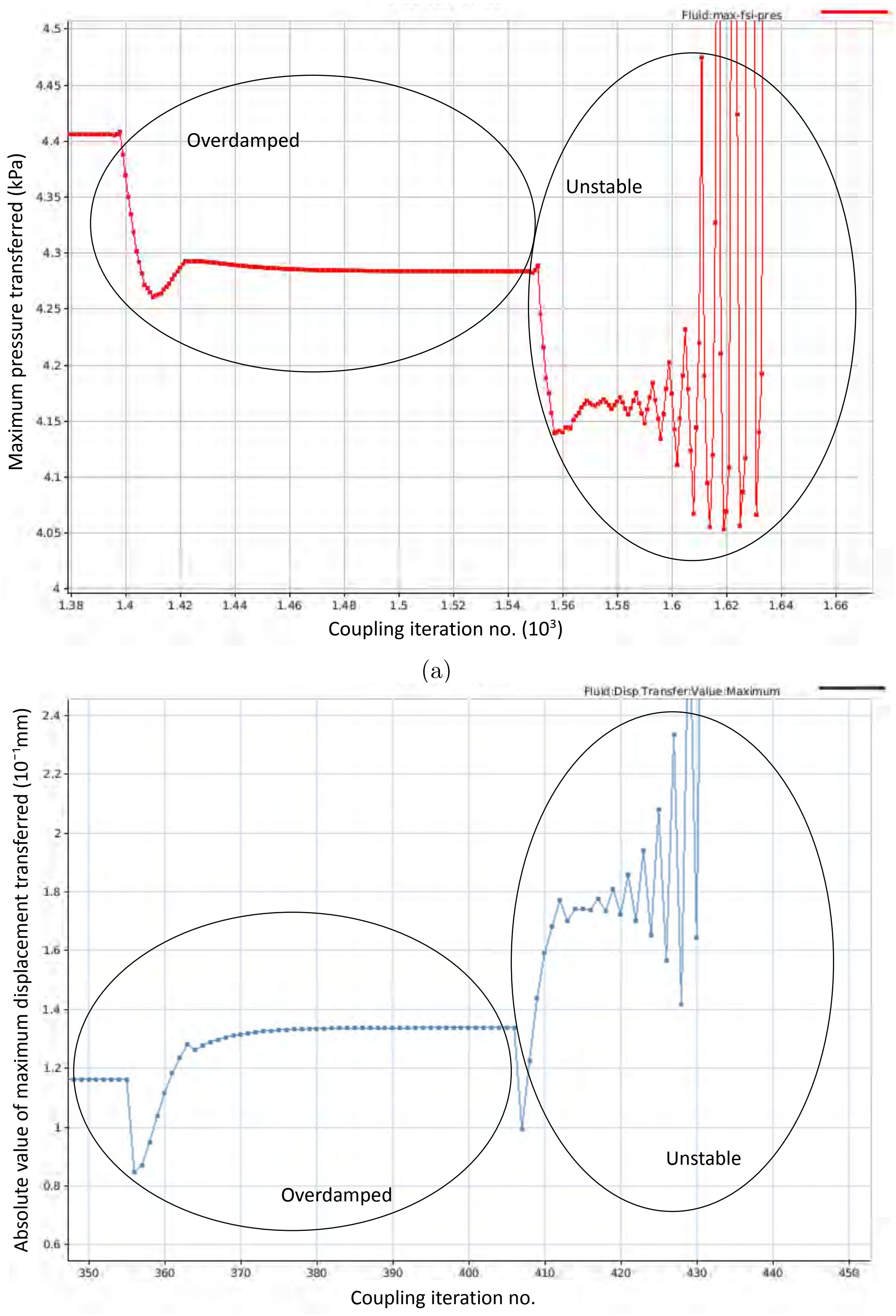

(a)

(b)

Figure 5.25: Unstable and overdamped solution behaviour at the FSI boundary: (a) maximum pressure (b) maximum displacement

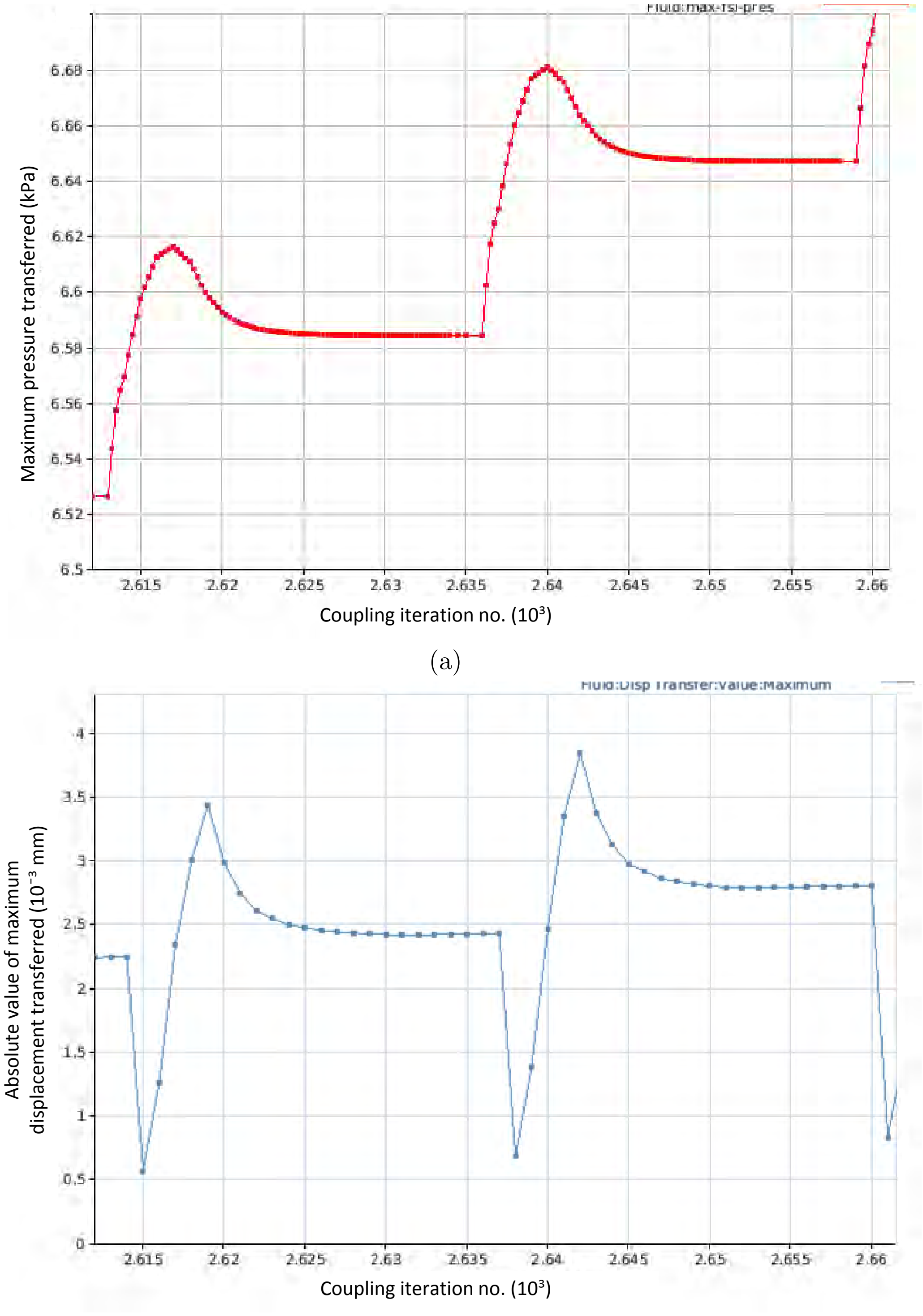

(a)

(b)

Figure 5.26: Solution behaviour at the FSI boundary for two full time-steps of the optimally damped FSI model: (a) maximum pressure (b) maximum displacement

as the solid model is not prestressed (see Section 5.3.3).

Because the initial configuration of the solid model is unstressed the geometries of the FSI and fluid simulation do not agree at the start of the simulation. The initial pressure causes the FSI model to deform initially while the fluid model obviously maintains its form. And since the artery deforms to a greater degree than the vein, the velocities in the artery are lower in the FSI model throughout the cardiac cycle. This is not the case for the vein, partly because it is more stiff and it is likely also because the change in velocities cause a change in resistances within the model. This must lead to a slightly different flow rate split causing the Windkessel outlet models re-equilibrate the overall FSI pressure and flow rate behaviour.

The problem here is also highlighted by the principal strain waveform in the solid. The minimum strain in the artery during the pulse is 0.84 and peaks at 0.98. Thus the total change in strain in the artery over the cardiac-cycle is 0.14 which is only 6 % of the initial strain or minimum strain. In the case of the vein this comes out at just over 5 %. The initial deformation and strain is not only incorrect but it is excessive. These results prove that pre-stressing the solid model is absolutely essential to accurately model the fluid-structure interaction of vascular access. Furthermore quantitative comparisons between the fluid and FSI model have little merit unless the FSI model is prestressed. This is likely the case for most, if not all, cardiovascular FSI modelling scenarios.

Regardless of the above, the relative velocity distributions and flow features predicted by both models are almost identical as seen in Figure 5.27. It must be taken into account that very small differences upstream in a fluid model can change the positioning of streamlines downstream to a large degree. The fistula anastomosis is viewed here in such a way that the artery is on the left and the blood flow is approaching the junction from the top of the figure. This presents the best view of the recirculation region in the vein on the right.

The solutions to the area-weighted average WSS over the FSI boundary in the FSI and fluid models are plotted over in Figure 5.30. Plotted in the same figure is the amount by which the fluid model overestimates the average WSS over the boundary when compared with the FSI model. The peak WSS in our fluid model is overestimated by approximately 12 % this is in comparison with the corresponding WSS overestimation

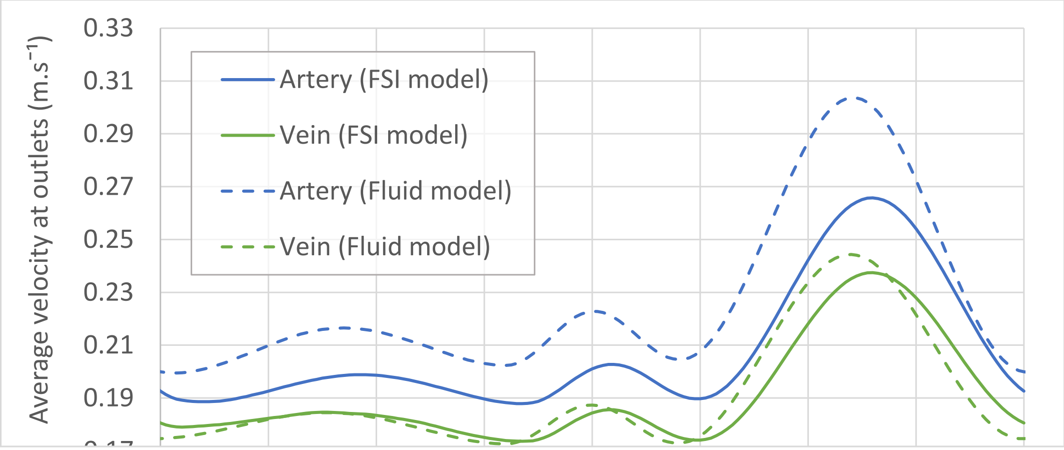

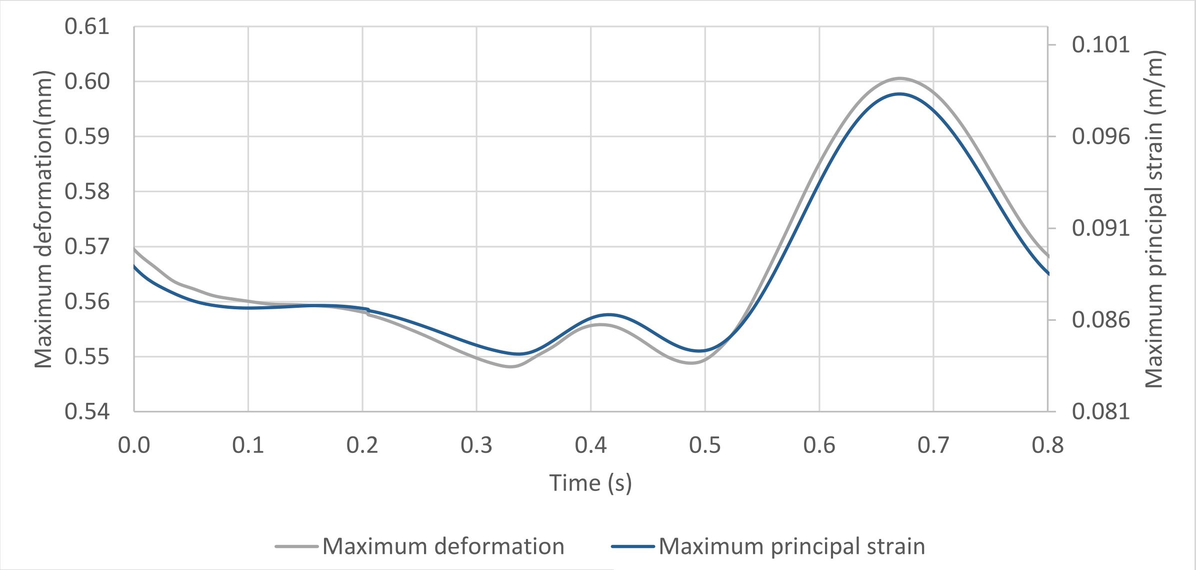

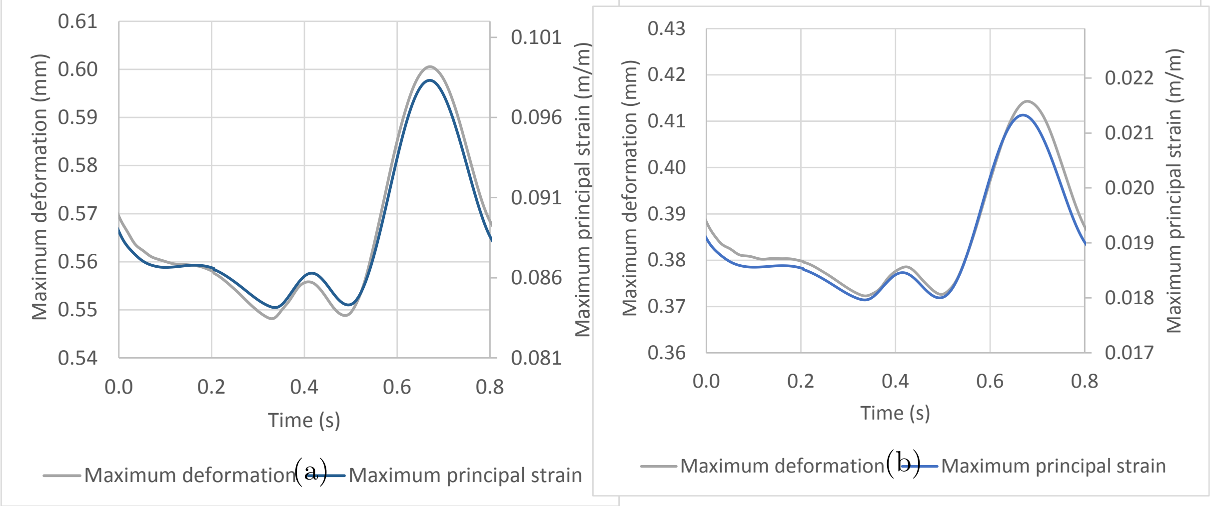

(a)

(b)

Figure 5.28: Transient profiles of the maximum deformation and maximum principal strain predicted by the FSI model: (a) in the artery walls and (b) in the vein walls

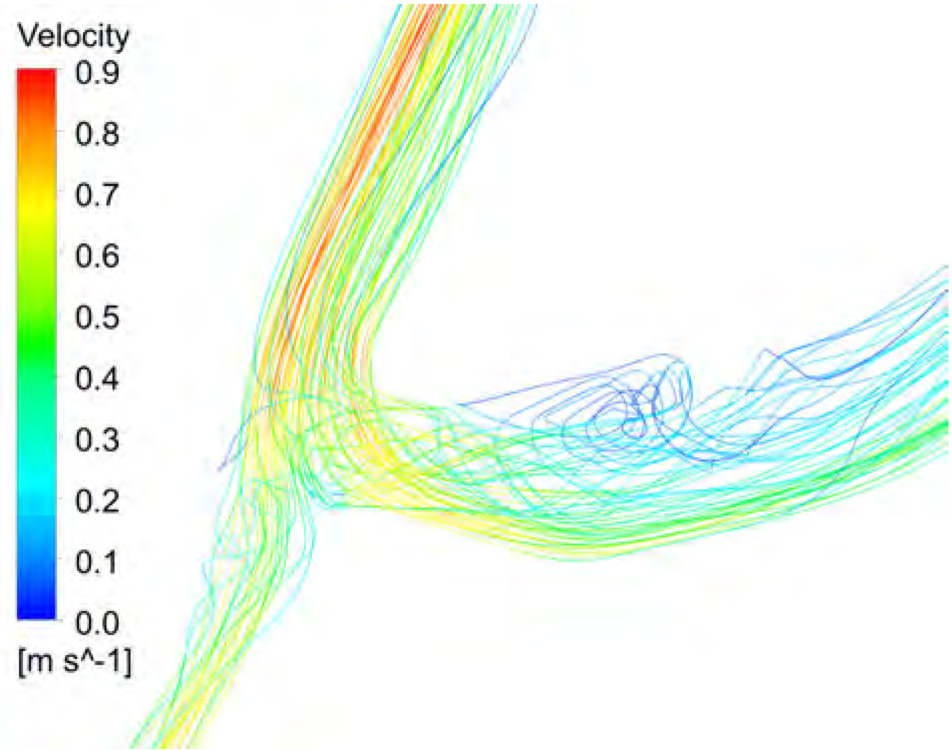

(a) Fluid model

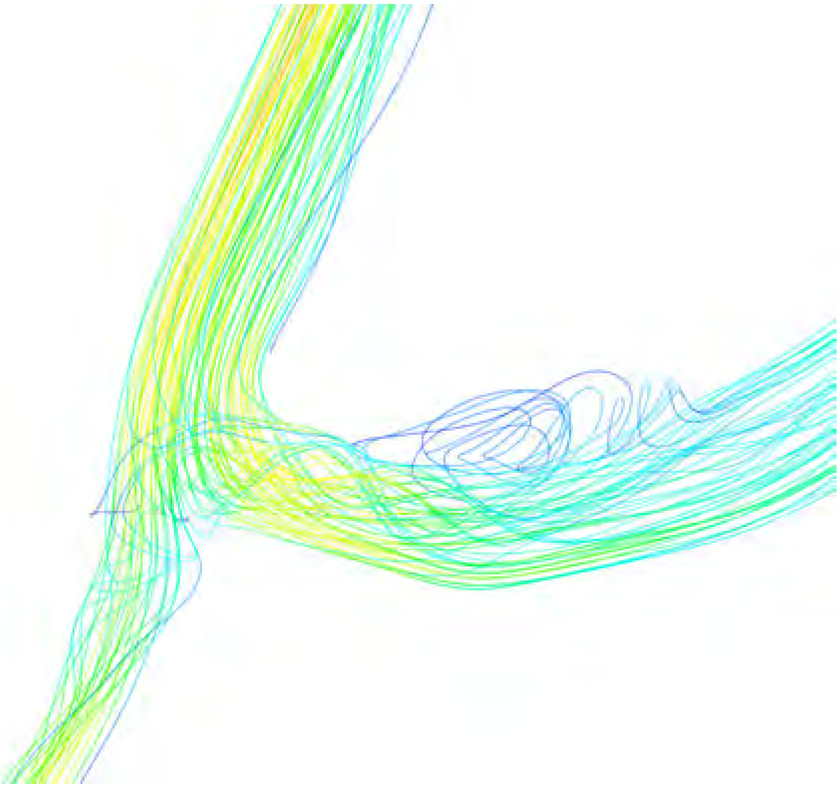

(b) FSI model

Figure 5.29: The velocity streamlines at the anastomosis and recirculation zone: (a) fluid model and (b) FSI model

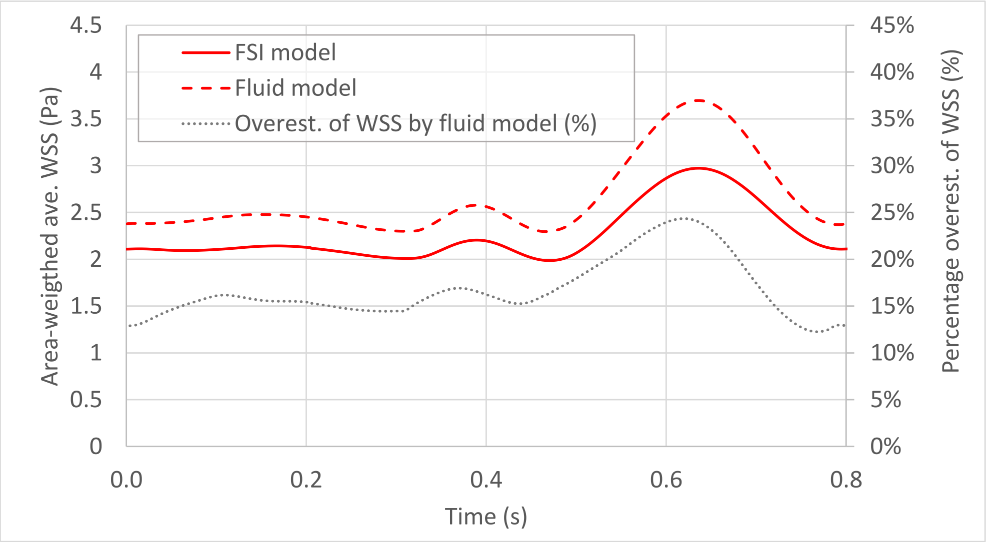

Figure 5.30: Maximum deformation and principal strain profiles in the FSI model

of 15 % by Decorato et al.[66]. The WSS distributions of the fluid and FSI models at peak flow rate are shown in Figure 5.31.

The velocity streamlines of the FSI model are shown alongside the PC-MRA velocity streamlines in Figure 5.32. These results relate to the peak flow rate. The fistula is viewed such that the artery is on the right with blood flow approaching the junction from the top right. Since the flow profile imposed at the inlet is not the patient-specific profile (see Section 5.1) the velocity magnitudes cannot really be compared here. It is evident that the FSI solution predicts the same flow features as the MRI sequence and that the relative velocity distribution is similar too. One further reason that they are not more similar is most likely due to errors in the mapping of the blood flow region from the relatively low resolution from the MRI side and in the process of developing the computational domain (see Section 5.2.1).

The fluid model velocity streamlines solution is shown alongside the PC-MRA velocity streamlines in Figure 5.33 in the region of the anastomosis. Again the artery is on the right and the flow approaches the junction from the top right. Zooming in on the anastomosis, it is now easier to see the similarity between the measured and modelled flow features at the juction, particularly at the recirculation region in the vein where blood flow stagnates.

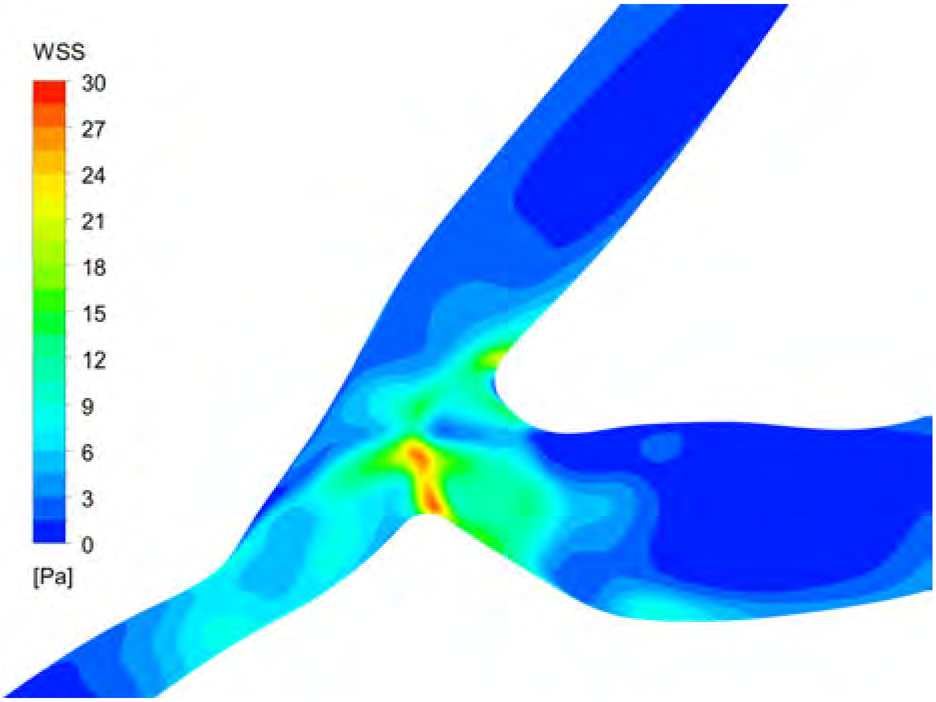

(a) Fluid model

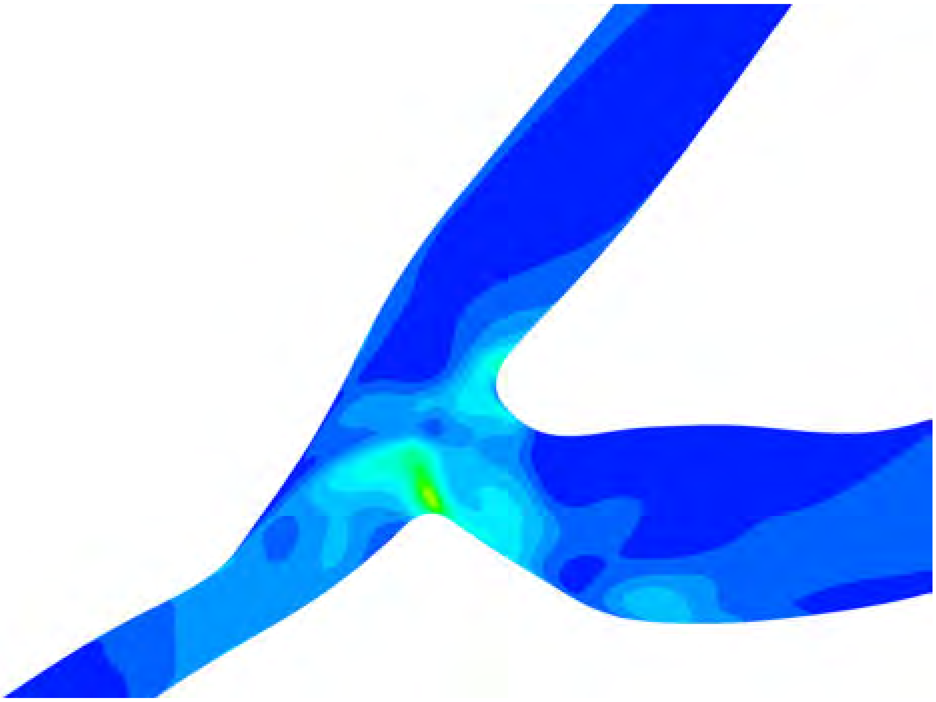

(b) FSI model

Figure 5.31: WSS solution contours: (a) fluid model and (b) FSI model

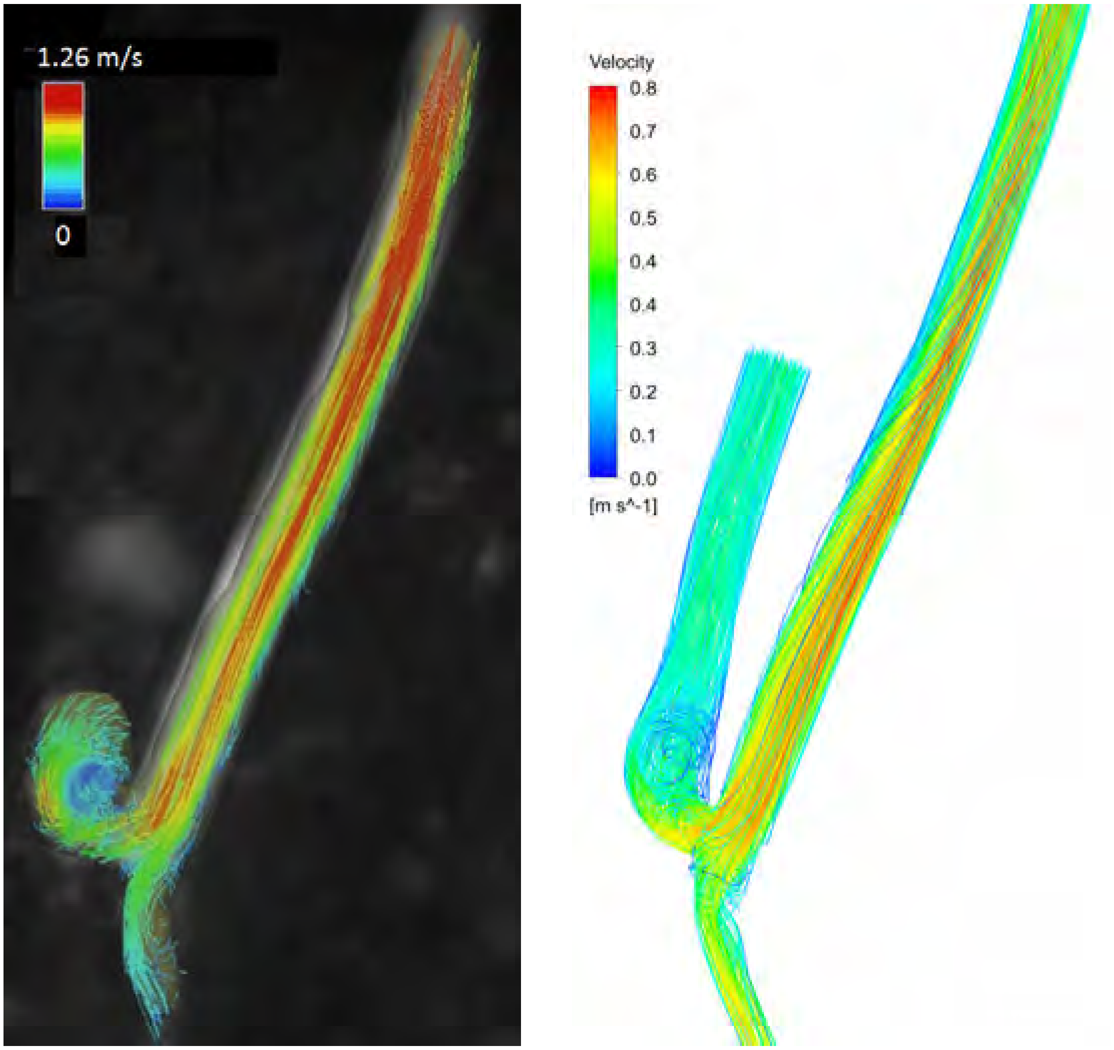

(a) (b)

Figure 5.32: Comparison of relative velocity streamlines: (a) PC-MRA sequence and processing [82] and (b) FSI model solution (legends and velocity magnitudes differ - flow conditions applied not that of patient-specific acquired data - see Sections 5.1 and 5.2.2)

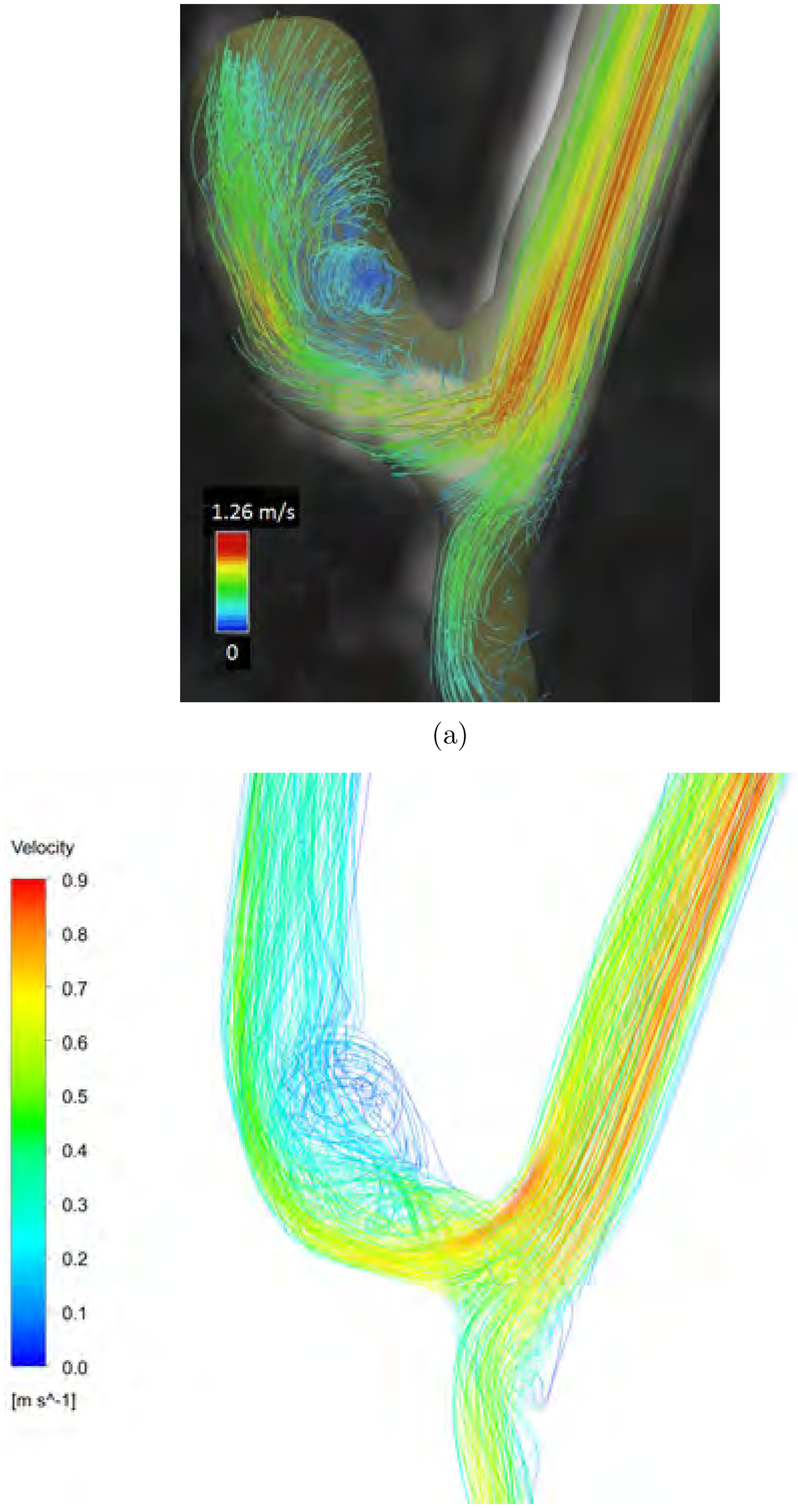

(a)

(b)

Figure 5.33: Comparison of relative velocity streamlines: (a) PC-MRA sequence and processing [82] and (b) fluid model solution (legends and velocity magnitudes differ - flow conditions applied not that of patient-specific acquired data - see Sections 5.1 and 5.2.2)

These results show that the FSI and fluid models predict very similar flow patterns even though these models cannot be compared quantitatively due to the lack of prestressing in the FSI model. Both models also agree qualitatively with the PC-MRA data in terms of flow features despite the fact that the flow conditions are very different. The WSS are the important criteria here however, and since the WSS are dependant on the velocities, an accurate solution to the velocity distribution is crucial. Prestressing is therefore vital to accurately predicting the WSS solution in FSI modelling of vessels. Although WSS are likely overestimated to much less of a degree to that found in our model or in [66], the deformations during the cardiac-cycle would ensure that WSS would be overestimated to some degree, especially at the peak flow rate. The comparative error between an FSI and fluid simulation of a fistula still needs to be deduced.

Chapter 6

Conclusions and recommendations

This thesis has presented the development and solution of a semi-implicit staggered FSI simulation of a patient-specific fistula. The approach has made use of ANSYS® Fluent® and ANSYS® Mechanical™ software, in conjunction with a semi-implicit staggered coupling algorithm, implemented in ANSYS® Workbench™ software, that solves the fluid and solid problems consecutively. The fluid is solved iteratively, providing the principal stabilisation features to the FSI model, while the solid direct solver converges fully and provides no form of stabilisation to the staggered scheme. It was found the FSI model could be optimally stabilised by combining a number of solution damping techniques within the iterative fluid solver, including FSI boundary stabilisation, together with a boundary transfer ramping algorithm in the coupling algorithm.

PC-MRA data has been used to develop patient- specific models that mimic the conditions scanned in an arteriovenous fistula. The small scale of the artery and vein dimensions in the arm limits the accuracy of the geometry of the model at the resolution of typical MRI scanners. It is recommended that more powerful MRI scanners with a higher resolution sequence be used in future studies, to better capture and define the domain of the model and obtain higher quality flow data.

A crucial element in sequencing a PC-MRA scan of a vascular access shunt, is to measure the patients blood flow prior to scanning. This ensures that the v_{enc} parameter is set correctly since blood flow rates can vary greatly between dialysis patients. This maximises the quality of the flow data obtained and minimises the amount of post-processing required of the data. The development of automated 3D smoothing and reconstruction techniques that are robust and which accurately extract the fluid domain from the scan would simplify the preprocessing stage of the modelling considerably.

Various lumped parameter models, including the three-element Windkessel model, have successfully been implemented at the outlets of the blood flow domain. Outlet models such as these are able to simulate the resistance of the upstream and downstream vessels and produce flow and pressure responses that are found in branching artery and vein structures. The pressures under which various forms of vascular access truly operate are unknown, however. Methods to measure the pressure should be explored to model fistulae and grafts more accurately. Complex lumped parameter models could then be developed to simulate an individual patients specific pressure responses in the artery and veins.

To model more accurrately the flow of blood in vascular access shunts, where shear-thinning is likely to occur, non-Newtonian fluid models such as the Casson, or Carreau–Yusada models, should be used for the blood. A more efficient fluid and FSI model could be developed by prescribing a parabolic velocity inlet condition, in place of the mass-flow boundary condition we have used. This would allow the inlet length to be shortened to reduce the DOF while still maintaining accuracy in the region of interest. This can be implemented if the inlet is made perfectly circular and takes advantage of the fact that an accurate velocity profile would develop over a shorter distance. A further improvement to the model may be gained by substituting the no-slip boundary condition used in this work with a more accurate blood flow shear condition, or one where wall roughness effects are taken into account.

We have modelled the vessel walls with a varying thickness at the anastomosis, using one layer of enhanced assumed strain solid elements to optimise the efficiency of the FSI model while solving the displacement solution with sufficient accuracy. To accurately determine the stresses and strains, especially any stress concentrations, higher density meshes with more element layers through the vessel wall should be used along with higher-order finite elements.

We have modelled the artery and veins as an incompressible isotropic hyperelastic material model each with their characteristic strengths. This material model could be enhanced to include anisotropy to improve the response of these vessel structures to the internal blood flow pressure.

A spring stiffness-based Robin boundary condition has been successfully implemented to mimic the effect of the surrounding tissue on the vessel walls. By combining this method with frictionless boundary conditions at the outlets of the model, it has been possible to reduce the problem size and computational expense without overconstraining it. The relative accuracy and efficiency between the following two vessel wall models should be assessed: a model with shell elements and sufficiently long inlets and outlets, and one with solid elements and shortened inlets and outlets such as those used in this work. The Robin boundary condition in these models could also be enhanced with additional modelling techniques such as damping: these may replicate the effect of the surrounding tissue more accurately.

The soft tissue model deforms excessively if it is not prestressed, resulting in an underapproximation of the velocity and WSS solutions, particularly in the artery. In this case a fluid model that disregards the movement of the vessel walls is likely to be a better predictor of the flow field than an FSI model. Regardless, it has been shown that both these models are able to predict flow features, such as recirculation, that may lead to vascular access failure. It would be important in future studies to extend the model by accounting for prestress in a manner that makes use of medically imaged data.

It is possible that a more efficient FSI model could be developed with an iterative solid and fluid solver. The solid model could then be partially solved each coupling step, as is the case with the fluid. This could potentially decrease the solid solver time within each coupling step, and further stabilise the FSI. It must be noted that an iterative solver may be ill-conditioned and perform poorly, if at all, due to the hollow and narrow-walled structure of arteries and veins. Efficiency may also be gained by solving the fluid and solid problems at the same time in each coupling step and transferring the boundary solutions at the same time. This usually has a destabilising effect on the FSI, however, as the fluid and solid models are out of sync in each coupling step. This could therefore have the opposite effect and increase the computational expense of the model, or even render it completely unsolvable. These changes should be tested in future work.

Bibliography

[1] MA Vazquez. Vascular access for dialysis: recent lessons and new insights. *Current Opinion in Nephrology and Hypertension*, 18(2):116–21, 2009.

[2] T Liyanage, T Ninomiya, V Jha, B Neal, HM Patrice, I Okpechi, M Zhao, and J Lv. Worldwide access to treatment for end-stage kidney disease: a systematic review. *The Lancet*, 385(9981):1975–1982, 2015.

[3] ESRD Patients in 2013: A Global Perspective. Technical report, Fresenuis Medical Care, Bad Homburg, 2014.

[4] SJ Schwab. Vascular access for hemodialysis. *Kidney International*, 55(5):2078–2090, 1999.

[5] Clinical practice guidelines for vascular access. *American Journal of Kidney Diseases*, 48, Supplement 1:S248 – S273, 2006.

[6] AJ Collins, RN Foley, C Herzog, BM Chavers, D Gilbertson, A Ishani, BL Kasiske, J Liu, LW Mau, M McBean, A Murray, WS Peter, H Guo, Q Li, S Li, S Li, Y Peng, Y Qiu, T Roberts, M Skeans, J Snyder, C Solid, C Wang, E Weinhandl, D Zaun, C Arko, SC Chen, F Dalleska, F Daniels, S Dunning, J Ebben, E Frazier, C Hanzlik, R Johnson, D Sheets, X Wang, B Forrest, E Constantini, S Everson, PW Eggers, and L Agodoa. Excerpts from the US renal data system 2009 annual data report. *American Journal of Kidney Diseases*, 55(1, Supplement 1):A6 – A7, 2010.

[7] H Wasse, N Kutner, R Zhang, and Y Huang. Association of initial hemodialysis vascular access with patient-reported health status and quality of life. *Clinical Journal of the American Society of Nephrology*, 2(4):708–714, 2007.

[8] M El-Nahas. The global challenge of chronic kidney disease. *Kidney International*, 68:2918–2929, 2005.

[9] R Barsoum. Chronic kidney disease in the developing world. *The New England Journal of Medicine*, 354:997–999, 2006.

[10] JB Wetmore and AJ Collins. Global challenges posed by the growth of end-stage renal disease. *Renal Replacement Therapy*, pages 1–7, 2016.

[11] AJ Collins, RN Foley, B Chavers, D Gilbertson, C Herzog, K Johansen, B Kasiske, N Kutner, J Liu, WS Peter, H Guo, S Gustafson, B Heubner, K Lamb, S Li, S Li, Y Peng, Y Qiu, T Roberts, M Skeans, J Snyder, C Solid, B Thompson, C Wang, E Weinhandl, D Zaun, C Arko, SC Chen, F Daniels, J Ebben, E Frazier, C Hanzlik, R Johnson, D Sheets, X Wang, B Forrest, E Constantini, S Everson, P Eggers, and L Agodoa. US renal data system 2011 annual data report. *American Journal of Kidney Diseases*, 59(1, Supplement 1):A7 –, 2012.

[12] AK Jain, P Blake, P Cordy, and AX Garg. Global trends in rates of peritoneal dialysis. *Journal of the American Society of Nephrology*, 23(3):533–544, 2012.

[13] M Allon and ML Robbin. Increasing arteriovenous fistulas in hemodialysis patients: problems and solutions. *Kidney International*, 62:1109–1124, 2002.

[14] T Kashiwagi, K Sato, S Kawakami, M Kiyomoto, M Enomoto, T Suzuki, H Genei, H Nakada, Y Iino, and Y Katayama. Effects of reduced dialysis fluid flow in hemodialysis. *Journal of Nippon Medical School*, 80(2):119–130, 2013.

[15] P Chakrabarti. Dialysis access: synthetic bridge graft. `http://www.calcuttayellowpages.com/cimage25/109177hemodia2.jpg`.

[16] P Chakrabarti. Dialysis access: primary arteriovenous fistula. `http://www.calcuttayellowpages.com/cimage25/109177hemodia1.jpg`.

[17] I Van Tricht, D De Wachter, J Tordoir, and P Verdonck. Hemodynamics and complications encountered with arteriovenous fistulas and grafts as vascular access for hemodialysis: a review. *Annals of Biomedical Engineering*, 33(9):1142–1157, 2005.

[18] F Basseau, N Grenier, H Trillaud, and C Douws. Volume flow measurement in hemodialysis. *Journal of Ultrasound in Medicine*, 18:177–183, 1999.

[19] LM Moist, L Trpeski, Y Na, and CE Lok. Increased hemodialysis catheter use in Canada and associated mortality risk: data from the Canadian Organ Replace-

ment Registry 2001–2004. *Clinical Journal of the American Society of Nephrology*, 3(6):1726–1732, 2008.

[20] DC McGee and MK Gould. Preventing complications of central venous catheterization. *New England Journal of Medicine*, 348(12):1123–1133, 2003.

[21] DW Windus. Permanent vascular access: a nephrologist's view. *American Journal of Kidney Diseases*, 21(5):457–471, 1993.

[22] S Schwab, A Besarab, G Beathard, D Brouwer, E Etheredge, M Hartigan, M Levine, R McCann, R Sherman, and S Trerotola. NKF-DOQI clinical practice guidelines for vascular access. *American Journal of Kidney Diseases*, 30(4):S150–S191, 1997.

[23] PV Suhocki, PJ Conlon, MH Knelson, R Harland, and SJ Schwab. Silastic cuffed catheters for hemodialysis vascular access: thrombolytic and mechanical correction of malfunction. *American Journal of Kidney Diseases*, 28(3):379–386, 1996.

[24] M Kumwenda, S Mitra, and C Reid. Clinical Practice Guidline: Vascular Access For Haemodialysis. Technical report, UK Renal Association, 2015.

[25] US Renal Data System. USRDS 2008 Annual Data Report: Atlas of Chronic Kidney Disease and End-Stage Renal Disease in the United States. Technical report, National Institutes of Health, National Institute of Diabetes and Digestive and Kidney Diseases, Bethesda, Maryland, 2008.

[26] H Wasse, RA Speckman, DL Frankenfield, MV Rocco, and WM McClellan. Predictors of delayed transition from central venous catheter use to permanent vascular access among ESRD patients. *American Journal of Kidney Diseases*, 49(2):276–283, 2007.

[27] SM Hazinedaroglu, HA Kayaoglu, D Ayli, N Duman, and MA Yerdel. Immediate postimplant hemodialysis through a new self-sealing heparin-bonded polycarbonate/urethane graft. *Transplantation Proceedings*, 36(9):2599 – 2602, 2004.

[28] Laminate Medical Technologies Ltd. Intimal hyperplasia. `http://www.laminatemedical.com/professionals/#1446382720115-a3dcaacb-124e`.

[29] R Munda, MR First, JW Alexander, CC Linnemann, JP Fidler, and D Kittur. Polytetrafluoroethylene graft survival in hemodialysis. *The Journal of the American Medical Association*, 249(2):219–222, 1983.

[30] M Allon. Current management of vascular access. *Clinical Journal of the American Society of Nephrology*, 2(4):786–800, 2007.

[31] P Ravani, LM Spergel, A Asif, P Roy-Chaudhury, and A Besarab. Clinical epidemiology of arteriovenous fistula in 2007. *Journal of Nephrology*, 20(B):141, 2007.

[32] PY Fan and SJ Schwab. Vascular access: concepts for the 1990s. *Journal of the American Society of Nephrology*, 3(1):1–11, 1992.

[33] RC Harland. Placement of permanent vascular access devices: Surgical considerations. *Advances in Renal Replacement Therapy*, 1(2):99–106, 1994.

[34] Z Kharboutly, M Fenech, JM Treutenaere, I Claude, and C Legallais. Investigations into the relationship between hemodynamics and vascular alterations in an established arteriovenous fistula. *Medical Engineering & Physics*, 29(9):999–1007, 2007.

[35] T Lee and NU Haq. New developments in our understanding of neointimal hyperplasia. *Advances in Chronic Kidney Disease*, 22(6):431–437, 2015.

[36] P Roy-Chaudhury, BS Kelly, MA Miller, A Reaves, J Armstrong, N Nanayakkara, and SC Heffelfinger. Venous neointimal hyperplasia in polytetrafluoroethylene dialysis grafts. *Kidney International*, 59(6):2325–2334, 2001.

[37] BS Kelly, SC Heffelfinger, JF Whiting, MA Miller, A Reaves, J Armstrong, A Narayana, and P Roy-Chaudhury. Aggressive venous neointimal hyperplasia in a pig model of arteriovenous graft stenosis. *Kidney International*, 62(6):2272–2280, 2002.

[38] P Roy-Chaudhury, VP Sukhatme, and AK Cheung. Hemodialysis vascular access dysfunction: a cellular and molecular viewpoint. *Journal of the American Society of Nephrology*, 17(4):1112–1127, 2006.

[39] P Roy-Chaudhury, LM Spergel, A Besarab, A Asif, and P Ravani. Biology of arteriovenous fistula failure. *Journal of Nephrology*, 20(B):150, 2007.

[40] P Roy-Chaudhury, L Arend, J Zhang, M Krishnamoorthy, Y Wang, R Banerjee, A Samaha, and R Munda. Neointimal hyperplasia in early arteriovenous fistula failure. *American Journal of Kidney Diseases*, 50(5):782–790, 2007.

[41] T Lee and P Roy-Chaudhury. Advances and new frontiers in the pathophysiology of venous neointimal hyperplasia and dialysis access stenosis. *Advances in Chronic Kidney Disease*, 16(5):329–338, 2009.

[42] SB Palder, RL Kirkman, AD Whittemore, RM Hakim, JM Lazarus, and NL Tilney. Vascular access for hemodialysis. patency rates and results of revision. *Annals of Surgery*, 202(2):235, 1985.

[43] EE Ethcredgc, SD Haid, and MN Maescr. Salvage operations for malfunctioning pdytetrafluoroethylene hemodialysis access grafts. *Surgery*, 94(5):464–70, 1983.

[44] SJ Schwab, LD Quarles, JP Middleton, RH Cohan, M Saeed, and VW Dennis. Hemodialysis-associated subclavian vein stenosis. *Kidney International*, 33(6):1156–1159, 1988.

[45] A Besarab, KL Sullivan, RP Ross, and MJ Moritz. Utility of intra-access pressure monitoring in detecting and correcting venous outlet stenoses prior to thrombosis. *Kidney International*, 47(5):1364–1373, 1995.

[46] DW Windus, J Audrain, R Vanderson, MD Jendrisak, D Picus, and JA Delmez. Optimization of high-efficiency hemodialysis by detection and correction of fistula dysfunction. *Kidney International*, 38(2):337–341, 1990.

[47] H Burger, JJ Zijlstra, SA Kluchert, AP Scholten, and G Kootstra. Percutaneous transluminal angioplasty improves longevity in fistulae and shunts for haemodialysis. *Nephrology Dialysis Transplantation*, 5(8):608–611, 1990.

[48] AA Safa, K Valji, AC Roberts, TW Ziegler, RJ Hye, and SB Oglevie. Detection and treatment of dysfunctional hemodialysis access grafts: effect of a surveillance program on graft patency and the incidence of thrombosis. *Radiology*, 199(3):653–657, 1996.

[49] J Sands and C Miranda. Prolongation of hemodialysis access survival with elective revision. *Clinical Nephrology*, 44(5):329–333, 1995.

[50] L Turmel-Rodrigues, J Pengloan, D Blanchier, M Abaza, B Birmele, O Haillot, and D Blanchard. Insufficient dialysis shunts: improved long-term patency rates with close hemodynamic monitoring, repeated percutaneous balloon angioplasty, and stent placement. *Radiology*, 187(1):273–278, 1993.

[51] American Access Care. Dialysis access management: angioplasty of stenosis with stent placement. `http://www.aacinterventionalny.com/dialysis-access-management.php`.

[52] B Ene-Iordache, L Mosconi, G Remuzzi, and A Remuzzi. Computational fluid dynamics of a vascular access case for hemodialysis. *Journal of Biomechanical Engineering*, 123(3):284, 2001.

[53] S Lee, DS Smith, F Loth, PF Fischer, and HS Bassiouny. Importance of flow division on transition to turbulence within an arteriovenous graft. *Journal of Biomechanics*, 40(5):981–992, 2007.

[54] AK Niemann, S Thrysoe, JV Nygaard, JM Hasenkam, and SE Petersen. Computational fluid dynamics simulation of av fistulas: from MRI and ultrasound scans to numeric evaluation of hemodynamics. *The Journal of Vascular Access*, 13(1):36–44, 2011.

[55] FN Van de Vosse, J De Hart, CHGA Van Oijen, D Bessems, TWM Gunther, A Segal, BJBM Wolters, JMA Stijnen, and FPT Baaijens. Finite-element-based computational methods for cardiovascular fluid-structure interaction. *Journal of Engineering Mathematics*, 47(3-4):335–368, 2003.

[56] J Chen, S Wang, G Ding, X Yang, and H Li. The effect of aneurismal-wall mechanical properties on patient-specific hemodynamic simulations: two clinical case reports. *Acta Mechanica Sinica*, 25(5):677–688, 2009.

[57] YH Kim, JE Kim, Y Ito, AM Shih, B Brott, and A Anayiotos. Hemodynamic analysis of a compliant femoral artery bifurcation model using a fluid structure interaction framework. *Annals of Biomedical Engineering*, 36(11):1753–1763, 2008.

[58] Z Li and C Kleinstreuer. Fluid-structure interaction effects on sac-blood pressure and wall stress in a stented aneurysm. *Journal of Biomechanical Engineering*, 127(4):662–671, 2005.

[59] D Tang, C Yang, S Kobayashi, J Zheng, PK Woodard, Z Teng, K Billiar, R Bach, and DN Ku. 3D MRI-based anisotropic FSI models with cyclic bending for human coronary atherosclerotic plaque mechanical analysis. *Journal of Biomechanical Engineering*, 131(6):061010, 2009.

[60] TE Tezduyar, S Sathe, M Schwaab, and BS Conklin. Arterial fluid mechanics modeling with the stabilized space–time fluid–structure interaction technique. *International Journal for Numerical Methods in Fluids*, 57(5):601–629, 2008.

[61] R Torii, NB Wood, N Hadjiloizou, AW Dowsey, AR Wright, AD Hughes, J Davies, DP Francis, J Mayet, GZ Yang, et al. Fluid–structure interaction analysis of a patient-specific right coronary artery with physiological velocity and pressure waveforms. *Communications in Numerical Methods in Engineering*, 25(5):565–580, 2009.

[62] DS Molony, A Callanan, EG Kavanagh, MT Walsh, and TM McGloughlin. Fluid-structure interaction of a patient-specific abdominal aortic aneurysm treated with an endovascular stent-graft. *BioMedical Engineering OnLine*, 8:24, 2009.

[63] D Tang, C Yang, S Mondal, F Liu, G Canton, TS Hatsukami, and C Yuan. A negative correlation between human carotid atherosclerotic plaque progression and plaque wall stress: in vivo MRI-based 2D/3D FSI models. *Journal of Biomechanics*, 41(4):727–736, 2008.

[64] CA Taylor and CA Figueroa. Patient-specific modeling of cardiovascular mechanics. *Annual Review of Biomedical Engineering*, 11:109, 2009.

[65] G Xiong, CA Figueroa, N Xiao, and CA Taylor. Simulation of blood flow in deformable vessels using subject-specific geometry and spatially varying wall properties. *International Journal for Numerical Methods in Biomedical Engineering*, 27(7):1000–1016, 2011.

[66] I Decorato, Z Kharboutly, T Vassallo, J Penrose, C Legallais, and AV Salsac. Numerical simulation of the fluid structure interactions in a compliant patient-specific arteriovenous fistula. *International Journal for Numerical Methods in Biomedical Engineering*, 30(2):143–159, 2014.

[67] M Ngoepe, B Reddy, D Kahn, C Meyer, P Zilla, and T Franz. A numerical tool for the coupled mechanical assessment of anastomoses of PTFE arterio-venous access grafts. *Cardiovascular Engineering and Technology*, 2(3):160–172, 2011.

[68] J Degroote, P Bruggeman, R Haelterman, and J Vierendeels. Stability of a coupling technique for partitioned solvers in FSI applications. *Computers & Structures*, 86(23-24):2224–2234, 2008.

[69] H Gharahi, BA Zambrano, DC Zhu, JK DeMarco, and S Baek. Computational fluid dynamic simulation of human carotid artery bifurcation based on anatomy and volumetric blood flow rate measured with magnetic resonance imaging. *International Journal of Advances in Engineering Sciences and Applied Mathematics*, 8(1):46–60, 2016.

[70] M Markl, FP Chan, MT Alley, KL Wedding, MT Draney, CJ Elkins, DW Parker, R Wicker, CA Taylor, RJ Herfkens, et al. Time-resolved three-dimensional phase-contrast MRI. *Journal of Magnetic Resonance Imaging*, 17(4):499–506, 2003.

[71] HB Grotenhuis, JJ Westenberg, P Steendijk, RJ van der Geest, J Ottenkamp, JJ Bax, JW Jukema, and A de Roos. Validation and reproducibility of aortic pulse wave velocity as assessed with velocity-encoded MRI. *Journal of Magnetic Resonance Imaging*, 30(3):521–526, 2009.

[72] P Dyverfeldt, JPE Kvitting, A Sigfridsson, J Engvall, AF Bolger, and T Ebbers. Assessment of fluctuating velocities in disturbed cardiovascular blood flow: In vivo feasibility of generalized phase-contrast mri. *Journal of Magnetic Resonance Imaging*, 28(3):655–663, 2008.

[73] PD Gatehouse, J Keegan, LA Crowe, S Masood, RH Mohiaddin, KF Kreitner, and DN Firmin. Applications of phase-contrast flow and velocity imaging in cardiovascular MRI. *European Radiology*, 15(10):2172–2184, 2005.

[74] A Harloff, F Albrecht, J Spreer, A Stalder, J Bock, A Frydrychowicz, J Schöllhorn, A Hetzel, M Schumacher, J Hennig, et al. 3D blood flow characteristics in the carotid artery bifurcation assessed by flow-sensitive 4D MRI at 3T. *Magnetic Resonance in Medicine*, 61(1):65–74, 2009.

[75] A Frydrychowicz, AF Stalder, MF Russe, J Bock, S Bauer, A Harloff, A Berger, M Langer, J Hennig, and M Markl. Three-dimensional analysis of segmental wall shear stress in the aorta by flow-sensitive four-dimensional-MRI. *Journal of Magnetic Resonance Imaging*, 30(1):77–84, 2009.

[76] C Canstein, P Cachot, A Faust, A Stalder, J Bock, A Frydrychowicz, J Küffer, J Hennig, and M Markl. 3D MR flow analysis in realistic rapid-prototyping model systems of the thoracic aorta: Comparison with in vivo data and computational fluid dynamics in identical vessel geometries. *Magnetic Resonance in Medicine*, 59(3):535–546, 2008.

[77] W Mangrum, K Christianson, S Duncan, P Hoang, AW Song, and E Merkle. *Duke Review of MRI Principles: Case Review Series*. Elsevier Health Sciences, 2012.

[78] TC Farrar and ED Becker. *Pulse and Fourier Transform NMR: Introduction to Theory and Methods*. Elsevier, 2012.

[79] P Beerbaum, H Körperich, P Barth, H Esdorn, J Gieseke, and H Meyer. Non-invasive quantification of left-to-right shunt in pediatric patients phase-contrast cine magnetic resonance imaging compared with invasive oximetry. *Circulation*, 103(20):2476–2482, 2001.

[80] VS Lee. *Cardiovascular MRI: Physical Principles to Practical Protocols*. Lippincott Williams & Wilkins, 2006.

[81] M Miyazaki and VS Lee. Nonenhanced MR angiography. *Radiology*, 248(1):20–43, 2008.

[82] S Jermy. 4D Flow and Displacement Sensitive MR Imaging of Upper-Arm Arteriovenous Connections for Haemodialysis. Master's thesis, University of Cape Town, 2016.

[83] MA Bernstein, KF King, and XJ Zhou. *Handbook of MRI Pulse Sequences*. Elsevier, 2004.

[84] RW Brown, YCN Cheng, EM Haacke, MR Thompson, and R Venkatesan. *Magnetic Resonance Imaging: Physical Principles and Sequence Design*. John Wiley & Sons, 2014.

[85] GA Holzapfel. *Nonlinear Solid Mechanics: a Continuum Approach for Engineering*. Wiley, Chichester, 2000.

[86] OH Yeoh. Some forms of the strain energy function for rubber. *Rubber Chemistry and Technology*, 66(5):754–771, 1993.

[87] RD Cook, DS Malkus, ME Plesha, and RJ Witt. *Concepts and Applications of Finite Element Analysis.* John Wiley & Sons, 2007.

[88] J Bonet and RD Wood. *Nonlinear Continuum Mechanics for Finite Element Analysis.* Cambridge University Press, Cambridge, 2nd edition, 2008.

[89] *ANSYS® Academic Research, Release 16.0, Help System, ANSYS Mechanical User's Guide.* ANSYS, Inc., 2015.

[90] *ANSYS® Academic Research, Release 16.0, Help System, Mechanical APDL Theory Reference.* ANSYS, Inc., 2015.

[91] JC Nagtegaal and DD Fox. Using assumed enhanced strain elements for large compressive deformation. *International Journal of Solids and Structures*, 33(20):3151–3159, 1996.

[92] JC Simo and F Armero. Geometrically non-linear enhanced strain mixed methods and the method of incompatible modes. *International Journal for Numerical Methods in Engineering*, 33(7):1413–1449, 1992.

[93] JC Simo, F Armero, and RL Taylor. Improved versions of assumed enhanced strain tri-linear elements for 3D finite deformation problems. *Computer Methods in Applied Mechanics and Engineering*, 110(3):359–386, 1993.

[94] U Andelfinger and E Ramm. EAS-elements for two-dimensional, three-dimensional, plate and shell structures and their equivalence to HR-elements. *International Journal for Numerical Methods in Engineering*, 36(8):1311–1337, 1993.

[95] NM Newmark. A method of computation for structural dynamics. *Journal of Engineering Mechanics*, ASCE(85 (EM3)):67–94, 1959.

[96] HK Versteeg and W Malalasekera. *An Introduction to Computational Fluid Dynamics: The Finite Volume Method.* Pearson Education Ltd, Harlow, England ; New York, 2007.

[97] *ANSYS® Academic Research, Release 16.0, Help System, Fluent User's Guide.* ANSYS, Inc., 2015.

[98] *ANSYS® Acedemic Research, Release 16.0, Help System, Fluent Theory Guide.* ANSYS, Inc., 2015.

[99] RI Issa. Solution of the implicitly discretised fluid flow equations by operator-splitting. *Journal of Computational Physics*, 62(1):40–65, 1986.

[100] HJ Bungartz and M Schäfer. *Fluid-Structure Interaction: Modelling, Simulation, Optimisation*, volume 1. Springer Science & Business Media, 2006.

[101] *ANSYS® Academic Research, Release 16.0, Help System, System Coupling User's Guide*. ANSYS, Inc., 2015.

[102] PF Galpin, RB Broberg, and BR Hutchinson. Three-dimensional navier stokes predictions of steady-state rotor/stator interaction with pitch change. In *Proceedings of 3rd Annual Conference of the CFD Society of Canada, Banff, AB, Canada*, volume 3rd Annual Conference of the CFD, Society of Canada, Banff, Alberta, Canada, 1995. Advanced Scientific Computing Ltd.

[103] KE Jansen, F Shakib, and TJR Hughes. Fast projection algorithm for unstructured meshes. *Computational Nonlinear Mechanics in Aerospace Engineering*, 146:175, 1992.

[104] C Förster, WA Wall, and E Ramm. Artificial added mass instabilities in sequential staggered coupling of nonlinear structures and incompressible viscous flows. *Computer Methods in Applied Mechanics and Engineering*, 196(7):1278–1293, 2007.

[105] M Markl, A Frydrychowicz, S Kozerke, M Hope, and O Wieben. 4D flow MRI. *Journal of Magnetic Resonance Imaging*, 36(5):1015–1036, 2012.

[106] RM Goldstein, HA Zebker, and CL Werner. Satellite radar interferometry: Two-dimensional phase unwrapping. *Radio Science*, 23(4):713–720, 1988.

[107] JM Huntley. Three-dimensional noise-immune phase unwrapping algorithm. *Applied Optics*, 40(23):3901–3908, 2001.

[108] O Marklund, J Huntley, and R Cusack. Robust unwrapping algorithm for 3-D phase volumes of arbitrary shape containing knotted phase singularity loops. *Journal of Scientific Research and Reports*, pages 1402–1528, 2005.

[109] H Essabbah, C Lacombe, G Fabre, J Saint-Blancard, D Daveloose, D Molle, and F Leterrier. Transient rheological study of blood stored in a liquid state. *Revue Francaise de Transfusion et Immuno-Hematologie*, 24(4):357–373, 1981.

[110] J Boyd, JM Buick, and S Green. Analysis of the Casson and Carreau-Yasuda non-Newtonian blood models in steady and oscillatory flows using the lattice Boltzmann method. *Physics of Fluids (1994-present)*, 19(9):093103, 2007.

[111] SS Shibeshi and WE Collins. The rheology of blood flow in a branched arterial system. *Applied Rheology*, 15(6):398, 2005.

[112] JF Hale, DA McDonald, and JR Womersley. Velocity profiles of oscillating arterial flow, with some calculations of viscous drag and the Reynolds number. *The Journal of Physiology*, 128(3):629, 1955.

[113] X He and DN Ku. Unsteady entrance flow development in a straight tube. *Journal of Biomechanical Engineering*, 116(3):355–360, 1994.

[114] YC Fung. *Biodynamics: Circulation.* Springer Science & Business Media, 2013.

[115] HJ Kim, IE Vignon-Clementel, CA Figueroa, JF LaDisa, KE Jansen, JA Feinstein, and CA Taylor. On coupling a lumped parameter heart model and a three-dimensional finite element aorta model. *Annals of Biomedical Engineering*, 37(11):2153–2169, 2009.

[116] L Itu, P Sharma, K Ralovich, V Mihalef, R Ionasec, A Everett, R Ringel, A Kamen, and D Comaniciu. Non-invasive hemodynamic assessment of aortic coarctation: validation with in vivo measurements. *Annals of Biomedical Engineering*, 41(4):669–681, 2013.

[117] HJ Kim, IE Vignon-Clementel, JS Coogan, CA Figueroa, KE Jansen, and CA Taylor. Patient-specific modeling of blood flow and pressure in human coronary arteries. *Annals of Biomedical Engineering*, 38(10):3195–3209, 2010.

[118] JM Corpataux, E Haesler, P Silacci, HB Ris, and D Hayoz. Low-pressure environment and remodelling of the forearm vein in Brescia–Cimino haemodialysis access. *Nephrology Dialysis Transplantation*, 17(6):1057–1062, 2002.

[119] MA Gutierrez, PE Pilon, SG Lage, L Kopel, RT Carvalho, and SS Furuie. Automatic measurement of carotid diameter and wall thickness in ultrasound images. *Computers in Cardiology*, pages 359–362, 2002.

[120] TC Gasser, RW Ogden, and GA Holzapfel. Hyperelastic modelling of arterial layers with distributed collagen fibre orientations. *Journal of the Royal Society Interface*, 3(6):15–35, 2006.

[121] KC McGilvray, R Sarkar, K Nguyen, and CM Puttlitz. A biomechanical analysis of venous tissue in its normal and post-phlebitic conditions. *Journal of Biomechanics*, 43(15):2941–2947, 2010.

[122] PJ Prendergast, C Lally, S Daly, AJ Reid, TC Lee, D Quinn, and F Dolan. Analysis of prolapse in cardiovascular stents: a constitutive equation for vascular tissue and finite-element modelling. *Journal of Biomechanical Engineering*, 125(5):692–699, 2003.

[123] E Maher, A Creane, S Sultan, N Hynes, C Lally, and DJ Kelly. Inelasticity of human carotid atherosclerotic plaque. *Annals of Biomedical Engineering*, 39(9):2445–2455, 2011.